POLITECNICO DI MILANO

School of Industrial and Information Engineering

Master of Science Program in Chemical Engineering

KINETIC AND FLUID DYNAMIC STUDY OF N-DOPING IN SIC CHEMICAL VAPOUR DEPOSITION

Supervisor: Prof. Carlo Alessandro Cavallotti

Master degree thesis of:

Nicolò DONINELLI

ID 883945

Academic Year 2019/2020

Table of Contents

Chapter 1: Introduction 1

1.1 Chemical Vapour Deposition 2

1.1.1 Conventional CVD Mechanism and Film Morphology 3

1.1.2 Classification of CVD Processes 5

1.1.3 Thermal CVD Growth Rate 7

1.1.4 Thermal CVD Reactors 8

1.1.5 Thermal CVD Process Layout 11

1.2 Silicon Carbide 13

1.2.1 Silicon Carbide Crystalline Structure 14

1.2.2 Silicon Carbide Properties, Applications and Role in the Electronics Industry 15

1.2.3 History of SiC Production Routes 17

1.3 Overview on n-type Doping of Silicon Carbide 22

1.3.1 State of the Art of SiC Film Growth and Doping through CVD 24

1.4 Thesis Purpose and Methodology 25

Chapter 2: Modelling of a CVD System and Computational Aspects 26

2.1 Governing Equations for a CVD Reactor 27

2.1.1 One Dimensional Heterogeneous Reactor Modelling 30

2.1.2 Physical Parameters 40

2.1.3 Kinetic Rates Evaluation 41

2.2 Kinetic Scheme 46

2.2.1 Gas Phase Reactivity 46

2.2.2 Surface Reactivity 48

2.2.3 Thermodynamic Analysis 50

2.3 Reactor Layout 52

2.4 Software Structure 54

2.4.1 Software Modifications 55

2.5 Experimental Data Review of Film Thickness and Doping Profiles 58

Chapter 3: Numerical Simulations of SiC Deposition and Nitrogen Incorporation 62

3.1 Introductory Aspects and Key Performance Indicators 63

3.1.1 Wafer Horizontal Subdivision 65

3.1.2 Operative Conditions: Monodimensional Model 67

3.1.3 Operative Conditions: Three-Dimensional Model 70

3.2 Sensitivity Analysis of the Kinetic Scheme 71

3.3 Baseline and Optimized Simulations of Silicon Carbide Deposition 75

3.3.1 Comparison between Baseline Simulation and Experimental Data 75

3.3.2 Comparison between Optimized Simulations and Experimental Data 78

3.4 Study of the Enhanced Nitrogen Incorporation at Wafer Edges 81

3.4.1 Three-Dimensional Simulations 86

Chapter 4: Conclusions and Future Prospects 90

List of tables

Chapter 1: Introduction

Table 1.1: *main CVD processes with their operating conditions.* 6

Table 1.2: *comparison between various vacuum pumps.* 12

Table 1.3: *silicon carbide main physical properties at standard conditions.* 13

Table 1.4: *intrinsic properties of Si and wide-bandgap semiconductors.* 15

Table 1.5: *comparison between main SiC production routes.* 21

Chapter 3: Numerical Simulations of SiC Deposition and Nitrogen Incorporation

Table 3.1: *geometrical features of each horizontal set of experimental data.* 66

Table 3.2: *feed molar composition.* 67

List of figures

Chapter 1: Introduction

Figure 1.1: *Chemical Vapour Deposition mechanism*. 4

Figure 1.2: *Thermal CVD reactor.* 5

Figure 1.3: *PECVD and PCVD reactors.* 6

Figure 1.4: *Si film growth rate vs reciprocal temperature over increasing mass transfer constant.* 7

Figure 1.5: *film thickness comparison between still, rotating and still-inclined susceptor configurations.* 8

Figure 1.6: *horizontal multi-wafer reactor.* 9

Figure 1.7: *vertical multi-wafer reactor*. 9

Figure 1.8: *barrel and vertical disk reactors.* 10

Figure 1.9: *chimney reactor.* 10

Figure 1.10: *TCVD process scheme.* 11

Figure 1.11: *silicon carbide phase diagram.* 13

Figure 1.12*: SiC base tetrahedron.* 14

Figure 1.13: *main SiC polytypes.* 14

Figure 1.14: *operating range of Si, SiC, GaN and diamond in the semiconductor industry.* 16

Figure 1.15*:* SiO_2 *– C calculated phase diagram.* 17

Figure 1.16: *Acheson furnace*. 18

Figure 1.17: *cross section of an Acheson furnace and temperature profile over time for each zone.* 18

Figure 1.18: *Lely furnace.* 19

Figure 1.19: *original LPE apparatus with its graphite lid and LPE furnace.* 20

Figure 1.20: *possible N incorporation sites on both Si and C polar faces of a 4H-SiC crystal.* 22

Chapter 2: Modelling of a CVD System and Computational Aspects

Figure 2.1: *heterogeneous model of a horizontal CVD reactor.* 30

Figure 2.2: *schematic representation of the* $C_2H_4/SiHCl_3/N_2$ *kinetic scheme.* 49

Figure 2.3: *distribution of main silicon chlorinated species diluted in a* H_2 *carrier gas as a function of temperature.* 50

Figure 2.4: *gas phase composition along the axis of a 150 mm wafer of a horizontal CVD reactor.* 51

Figure 2.5: *digital twin of PE-106 reactor.* 52

Figure 2.6: *simulated gas temperature profile for each zone of the reactor.* 53

Figure 2.7: *transverse section of the PE-106 reactor.* 53

Figure 2.8: *comparison between the pre-existing and the modified wafer temperature profile.* 56

Figure 2.9: *film thickness colormap for the rotating susceptor configuration.* 58

Figure 2.10: *N incorporation colormap for the rotating susceptor configuration.* 59

Figure 2.11: *film thickness colormap for the still susceptor configuration.* 60

Figure 2.12: *N incorporation colormap for the still susceptor configuration.* 61

Chapter 3: Numerical Simulations of SiC Deposition and Nitrogen Incorporation

Figure 3.1: *schematic representation of the wafer subdivision in horizontal sectors.* 65

Figure 3.2: *wafer flat temperature profile.* 68

Figure 3.3: *wafer "gaussian" temperature profile, G1.* 68

Figure 3.4: *wafer "gaussian" temperature profile, G2.* 68

Figure 3.5: *wall temperature profile over the axial coordinate of the reactor centerline.* 69

Figure 3.6: *peak growth rate percent variance from a reference value of 0.38 µm/min.* 71

Figure 3.7: *film disuniformity percent variance from a reference value of 1.3E-02.* 72

Figure 3.8: *doping disuniformity variance from a reference value of 9.8E-03.* 73

Figure 3.9: *growth rate profile over the centerline axial length, comparison between baseline simulation and experimental data.* 75

Figure 3.10: *averaged growth rate profile over the centerline axial length, comparison between baseline simulation and experimental data.* 76

Figure 3.11: *nitrogen incorporation profile over the centerline axial length, comparison between baseline simulation and experimental data.* 77

Figure 3.12: *averaged growth rate profile over the centerline axial length, comparison between optimized simulation and experimental data.* 78

Figure 3.13: *averaged nitrogen incorporation profile over the centerline axial length, comparison between optimized simulation and experimental data.* 78

Figure 3.14: *averaged nitrogen incorporation profile over the centerline axial length, comparison between simulations conducted with "gaussian" temperature profiles.* 79

Figure 3.15: *fitted N incorporation profile along the axial length of the centerline.* 81

Figure 3.16: *nitrogen incorporation profile along the axial length of abscissa R2.* 82

Figure 3.17: *nitrogen incorporation profile along the axial length of abscissa R3.* 83

Figure 3.18: *nitrogen incorporation profile along the axial length of abscissa R5.* 83

Figure 3.19: *nitrogen incorporation profile along the axial length of abscissa R6.* 84

Figure 3.20: *inlet dopant molar fraction predicted by the proportional relation for each abscissa versus distance from the centerline.* 84

Figure 3.21: *colormap of N deposition rate in the still susceptor configuration.* 88

Preface

Silicon Carbide is one of the most promising wide band-gap semiconductors employed for the manufacturing of devices requiring high power density and high voltage capability. This is due to its excellent electronic properties, like large breakdown electric field and thin drift layers, which makes SiC equipment able to withstand higher temperatures and switching frequencies compared to the most common and widespread silicon devices. Currently, the optimal way to produce such equipment within market standards is represented by substrate deposition of a thin silicon carbide epitaxial film made of a series of monocrystalline layers grown through Chemical Vapour Deposition; to adjust the electronic properties of the grown material, doping with elements like aluminium, phosphorous or nitrogen is performed in-situ during epitaxial growth. The ending product of the deposition process is a circular wafer with a diameter ranging from 150 to 200 mm.

Industrially, silicon carbide epitaxial growth has still to overcome several important challenges, the most relevant being the achievement of satisfying film and doping uniformity of the semiconductive wafer. Such aspect is investigated from a fluid dynamic and a kinetic point of view in this thesis work, whose structure consists of four chapters:

- Chapter 1 covers the most important physical and technological aspects of chemical vapour deposition as well as silicon carbide main properties and manufacturing processes.
- Chapter 2 describes the governing equations and software employed to model the industrial epitaxy reactor studied in this work; it also reviews the experimental data obtained from the reactor while denoting issues and anomalies related to the nitrogen incorporation trend.
- Chapter 3 resumes the outcomes of several numerical simulations of nitrogen doped silicon carbide deposition conducted in this work and compares them with the experimental data.
- Chapter 4 draws conclusions from the simulations results and eventually outlines future expectations and improvements related to the numerical modelling of silicon carbide deposition performed with the tools presented in this thesis.

Abstract

In this thesis work, chemical kinetics and fluid dynamic behaviour of silicon carbide film growth and nitrogen doping carried inside an industrial Chemical Vapour Deposition reactor, suitable for the production of 150 mm 4H-SiC (0001) circular wafers, have been investigated through numerical simulations conducted with two physical models, one monodimensional and one three-dimensional, implemented in two different softwares; several fixes were applied to the software containing the 1D discretization in an attempt to improve the quality of the simulations.

A sensitivity analysis performed at the beginning of this work allowed to identify the key species involved in silicon carbide film growth and nitrogen doping.

Subsequently, several optimized monodimensional simulations were launched in order to replicate the experimental trends of growth rate and nitrogen incorporation gathered from two test runs.

Lastly, the phenomenon of uneven nitrogen incorporation observed at the lateral zones of the growing silicon carbide wafer was investigated first with a set of simplified monodimensional simulations featuring a fictitious dopant species and then with more detailed three-dimensional simulations; this phenomenon was supposed to be triggered by gas phase reactions converting molecular nitrogen into a dopant intermediate. The outcome of these computations suggests that the reactor could benefit either from a reduction of the wafer's diameter or by the use of a more efficient dopant precursor.

CHAPTER 1

Introduction

This chapter resumes the most important features about Chemical Vapour Deposition.

Section 1.1 introduces the acknowledged mechanism of the process, giving a brief classification of CVD techniques and equipment with a particular focus on thermal CVD.

Subsequentially, Section 1.2 is dedicated to silicon carbide and its crystallographic properties along with its applications in the microelectronics industry and a synthesis of SiC main production routes patented from the end of the 19th century to the modern era.

Section 1.3 gives an overview on n-type doping, summarizing the results of numerous academic publications through the years in order to clarify the influence of CVD main parameters and operating conditions over nitrogen incorporation and film growth.

In the end, Section 1.4 contains the objectives of this thesis work.

1.1 Chemical Vapour Deposition

Chemical Vapour Deposition (CVD) is a process involving the formation of a thin solid film on a substrate through chemical reactions of selected metallic/organo-metallic precursor species. These species are injected in a carrier gas (typically H_2, He, N_2 or Ar) fed to a reactor, consisting of a vacuum growth chamber and a heated susceptor: inside the chamber, precursors dissociate in the gaseous phase forming reactive intermediates that diffuse towards a growth plate located on the susceptor, where deposition occurs.

Since properties of the deposited film largely depend on the employed precursors, one of the main requirements for these species is a high chemical purity; although in some cases impurities incorporation in the film has a beneficial role on the properties of the ending product, most of the times the presence of traces of metals or other organic molecules significantly degrades film quality. Thus, precursors undergo several purification treatments in an attempt to minimize their impurities content. Another desideratum is an adequate volatility: this is not an issue for species naturally occurring in a gaseous state (C_2H_2, SiH_4, N_2), but it is for liquid and solid precursors as their low vapour pressures could compromise vaporization and transport into the carrier gas; moreover, the ideal precursor must exhibit a large temperature interval between its evaporation and decomposition coupled with good thermal stability. This latter feature is particularly appreciated not only from a productive point of view, as it allows to stock the precursors for long period of times without wastages, but also for safety reasons as it minimizes the risk of runaway and release of harmful compounds in the surrounding environment.

Ultimately, various type of films can be grown through chemical vapour deposition processes with different crystallographic and electronic properties suitable for the production of corrosion-resistant coatings, composite materials, catalysts and semiconductors; regarding this latter field, from the second half of the 20th century silicon has been extensively employed for the production of power electronic devices in the microelectronics industry. Nowadays, lot of interest is growing towards other species like Ge, Ga, GaN, SiC and diamond as they have shown excellent thermoelectronic properties and, unlike silicon, they are able to operate at high temperatures and frequencies.

1.1.1 Conventional CVD Mechanism and Film Morphology

The CVD process, from its fundamental standpoint, is made of several physicochemical steps involving interaction between gas species and substrate:

1. convective mass transfer of the precursors, which are inserted in the growth chamber through the carrier gas;
2. precursors pyrolysis leading to the formation of reactive intermediates;
3. material and thermophoretic diffusive mass transfer of the reactants from the gaseous bulk to the substrate;
4. reactants adsorption onto the substrate;
5. surface diffusion to growth sites, surface recombination reactions and nucleation processes. Adsorbed atoms are incorporated inside the growing film;
6. by-products desorption;
7. diffusive mass transfer of the by-products from the substrate to the gaseous bulk;
8. convective mass transfer from the growth chamber to the outlet.

Surface diffusion and nucleation phenomena determine the overall morphology and properties of the film. This process is described by the Terrace Step Kink mechanism, developed by Burton et al.[1], which states that the deposition surface can be assumed as an evolving terrace formed by nucleation of adsorbed species. Terrace growth occurs by insertion of adsorbed species into kinks at terrace edges (step growth) or by clusters formation over the terrace (cluster growth); competition between these two mechanisms depends on the characteristic times of surface diffusion and kink insertion of adsorbed atoms: if the former phenomenon is faster than the latter, then adatoms will aggregate through cluster growth; moreover, if the aggregates size reaches a critical value they act as new nucleation sites leading to the formation of polycrystalline or amorphous layers.

In the opposite case, i.e. if kink insertion is faster than surface diffusion, adsorbed species will tend to form overlapping identical monolayers (epitaxial layers) resulting in a monocrystalline film with very few defects; epitaxial growth is a thermally activated process which can be homogeneous, if substrate and growing layers are made of the same material, or heterogeneous, if substrate and growing layers materials are different but with similar crystalline lattices.

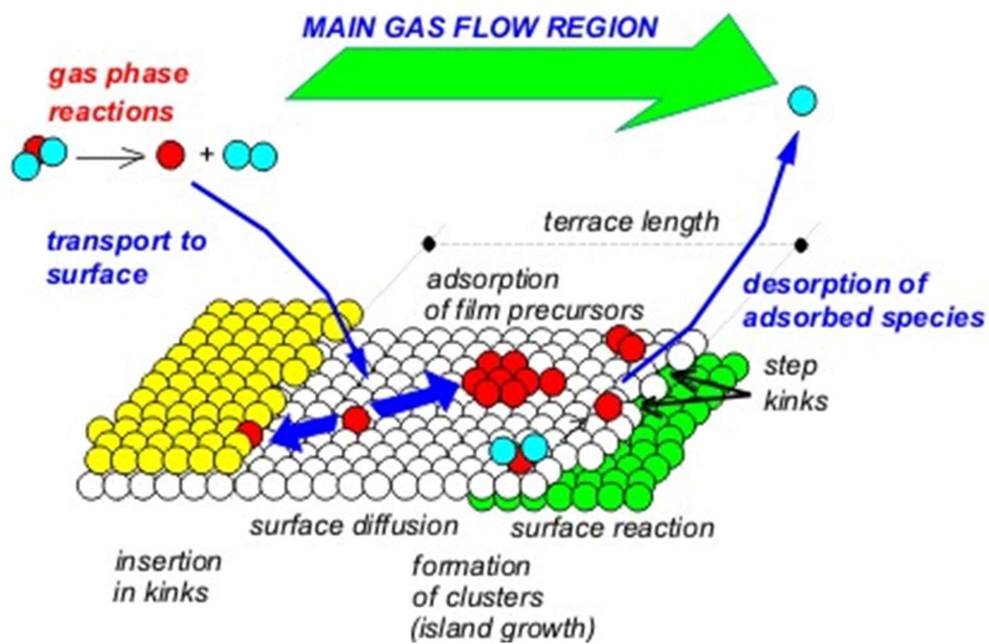

Figure 1.1: *Chemical Vapour Deposition mechanism*[2].

1.1.2 Classification of CVD Processes

Most of the reactions involved in chemical vapour deposition processes are endothermic and with high activation energies, hence they require an energy input: a classification of CVD methods can be made in terms of how this energy source is provided.

Thermal CVD[3] processes rely on a temperature gradient established between a heating element, located outside and close to the reactor walls or under its susceptor, and the growth chamber; as a result of this, the temperature of the system increases. The employed heating element is often a radio-frequency coil or an infra-red lamp (radiative heat transfer) or an electrical resistance adherent to the susceptor (conductive heat transfer); cooling water flows into pipes in contact with the external walls to control the temperature of the chamber. Although TCVD is the simplest approach to control film growth rate, it is not suited for temperature-sensitive substrates as they could degrade.

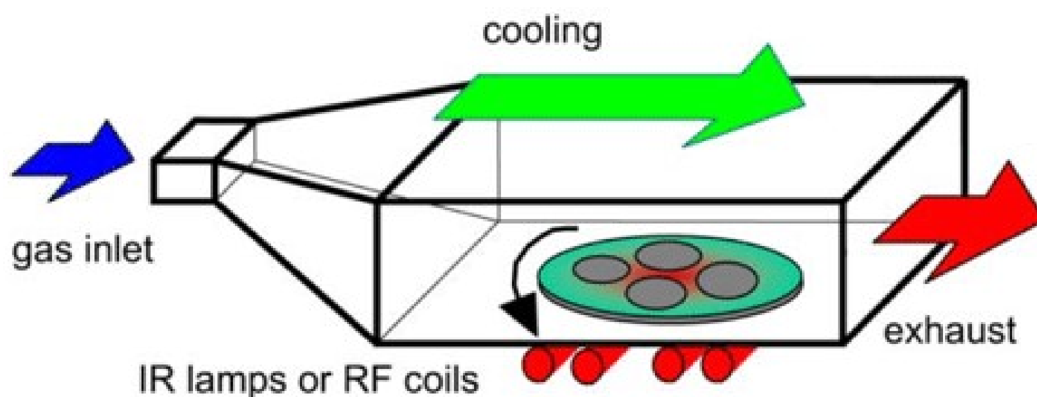

Figure 1.2: *Thermal CVD reactor[4], cooling on the chamber ceiling allows an optimal temperature control.*

Plasma Enhanced CVD[5] adopts an electric field to ionize the gaseous phase obtaining a plasma where excited electrons, detached from their original atomic nuclei, create highly reactive species that will lead to film growth. The electric field is generated applying two electrodes, one connected with the susceptor and one with the chamber ceiling, powered by alternate or direct current generators; PECVD allows to operate with lower temperatures (300÷450 K), but it is a complex process involving several parameters that needs to be controlled since plasma can damage the deposition surface, compromising film properties.

In Photolytic CVD[6] processes precursors decomposition is triggered by photons of a specific light source, i.e. a laser light concentrated towards a susceptor through a quartz lens irradiating both the gas and the growing film. The energy input can be manipulated by changing the light source frequency or wavelength, selectively enhancing certain reactions inside the chamber.

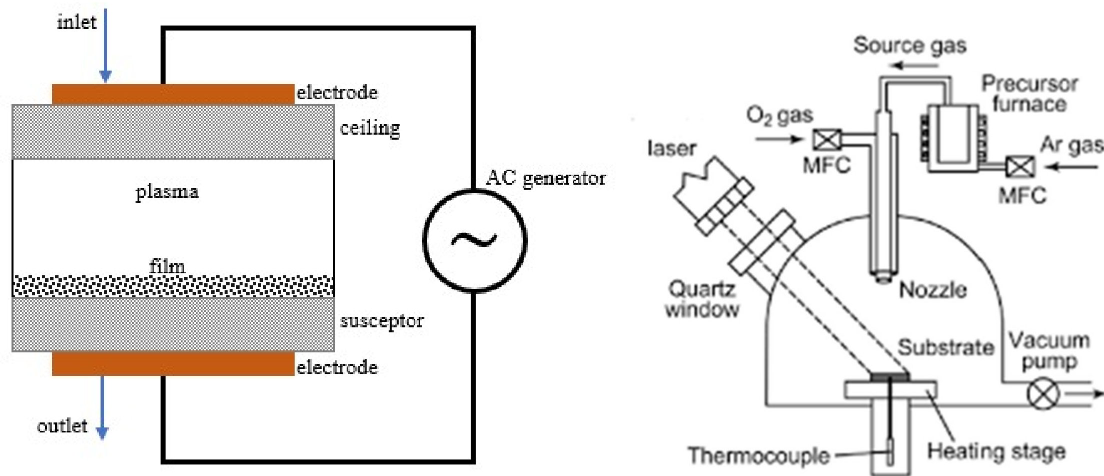

Figure 1.3: *PECVD (left) and PCVD[7] (right) reactors.*

An extremely sophisticated CVD process is Atomic Layer Epitaxy[5], where precursors are sequentially introduced into a reactive chamber with a series of pulses: in each of these pulses precursor molecules are adsorbed on the substrate and further react with the surface until all the reactive sites are saturated; then, the system is purged to remove remaining precursor traces in the gas phase and another species is injected to continue the deposition until the desired film composition and thickness are reached. This technique allows to regulate the amount of each deposited compound minimizing defects formation.

Process	Operating conditions	Driving force
TCVD	1773÷2273 K, ≤1 bar	Temperature gradient
PECVD	300÷450 K, ≤1 bar	Potential gradient
PCVD	673÷773 K, ≤1 bar	Light source (photons)

Table 1.1: *main CVD processes with their operating conditions.*

1.1.3 Thermal CVD Growth Rate

The main parameter controlling film growth in conventional TCVD processes is, obviously, temperature. Dependence of film growth rate on substrate temperature is displayed in Figure 1.4, which reports the growth rate of a Si film, obtained from $SiCl_4$ reduction with hydrogen and deposition, as a function of reciprocal temperature.

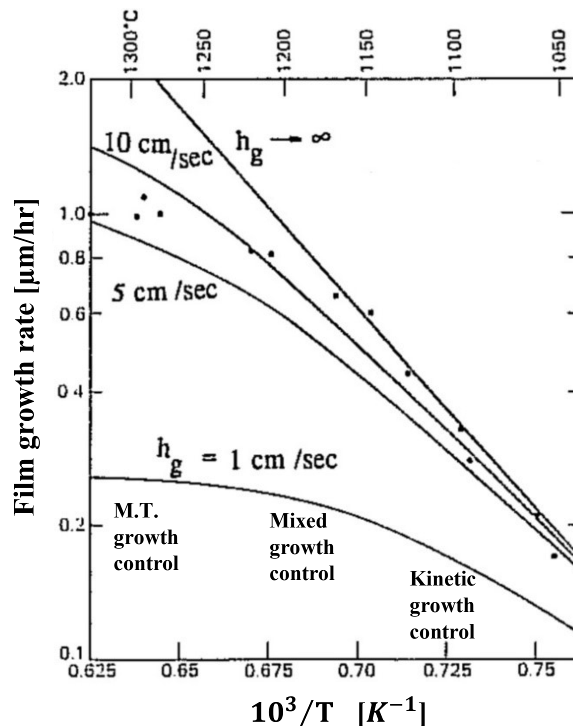

Figure 1.4: *Si film growth rate vs reciprocal temperature*[8] *over increasing mass transfer constant* (h_g).

At low temperatures, both gaseous and surface reactivity are slow with respect to mass transfer so the growth rate has an exponential trend directly proportional to the Arrhenius equation (kinetic growth control); this region can be extended to even higher temperatures by increasing the mass transfer constant through manipulation of the operative conditions. On the other hand, kinetics is enhanced at high temperatures and mass transfer becomes the controlling process (mass transfer growth control); in this region the growth rate is almost constant and its dependence on temperature is negligible.

Ultimately, if the temperature is raised even more growth rate shows a declining trend, not reported in Figure 1.4, due to gas phase parasitic reactions and increased precursors desorption[9] from the film.

1.1.4 Thermal CVD Reactors

Despite the numerous design configurations available for TCVD reactors, it is possible to distinguish two main categories based on the growth chamber geometrical orientation: horizontal and vertical.

An example of the former configuration is the disk reactor, shown in Figure 1.2, where the gaseous feed contacts a wafer placed on a susceptor which can be either a still or a rotating disk: susceptor motion affects film thickness; indeed, if the susceptor is still then film thickness will have a bear trend as the highest deposition zone, i.e. the part of the reactor where precursors diffusive fluxes are maximum and grant the highest driving force for surface reactions, is the wafer inlet edge. In this zone the boundary layer thickness, δ_x, is minimum and it can be shown[9] that the diffusive flux of a generic species is inversely proportional to δ_x. Otherwise, if the disk is rotating film thickness will be more uniform since each outer portion of the wafer becomes the highest deposition zone.

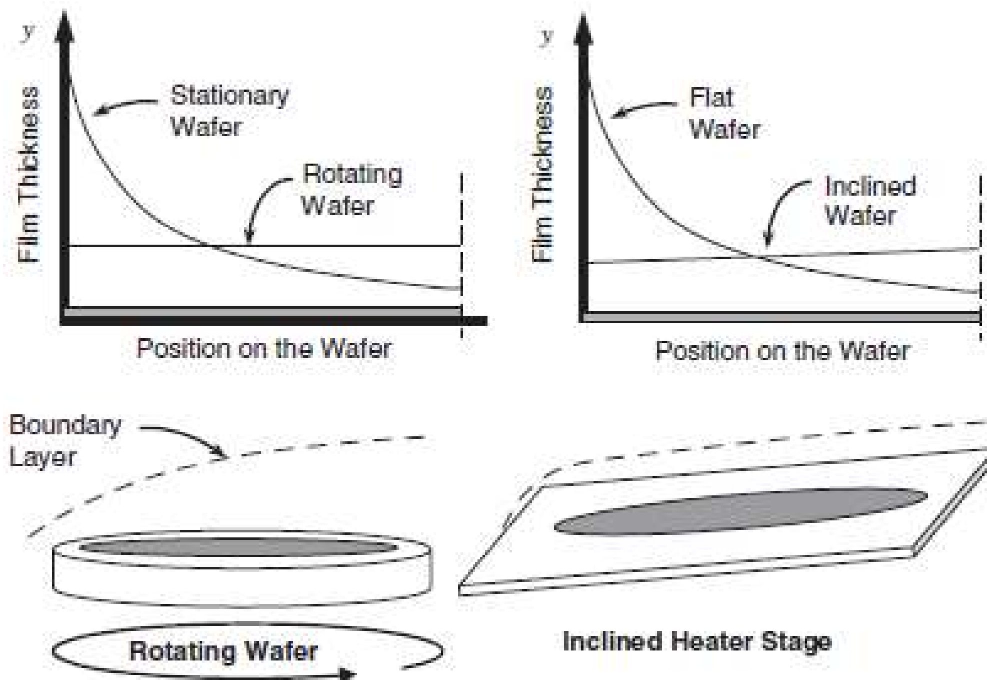

Figure 1.5: *film thickness comparison between still, rotating and still-inclined susceptor configurations*[9].

Still susceptors can be tilted (Figure 1.5) to reduce the growth chamber cross section and consequently enhance the gaseous bulk flow velocity in the deposition zone: this increment flattens the boundary layer profile promoting film uniformity.

A high production horizontal configuration is represented by the multi-wafer reactor, where a line of growth plates (wafers) is fixed to a support (boat) inside the growth chamber and gas is gradually injected from distribution tubes located along the reactor axis or at the inlet. The thermal gradient is manipulated with a three zone heating element: if the growth rate decreases in one of these zones, then it is possible to locally raise the temperature and further enhance the kinetics of the process.

Among vertical reactors, the most widespread configurations are the barrel reactor, the (vertical) disk reactor and the chimney reactor: in barrel and disk reactors the gaseous inlet enters from the top of the chamber and film growth occurs onto plates attached to the susceptor, which is either a rotating prism or disk; instead, chimney reactors feature a still susceptor fixed to the chamber wall. Despite the difficult temperature control due to vertical convection phenomena, these configurations allow to produce thicker films in less time than horizontal reactors.

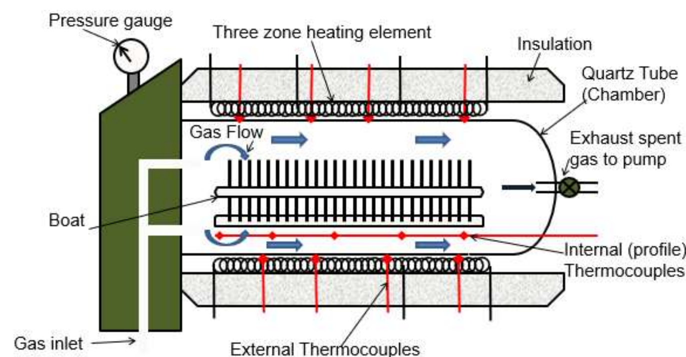

Figure 1.6: *horizontal multi-wafer reactor*[11].

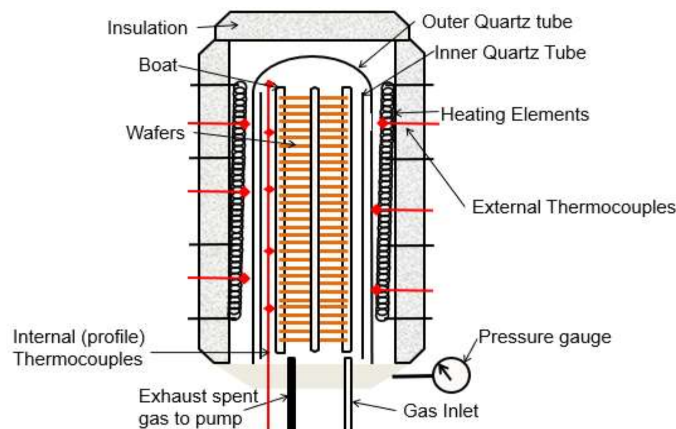

Figure 1.7: *vertical multi-wafer reactor*[11].

Regarding the reactor wall temperature, two designs are available:

- *hot wall* reactors ensure a more uniform temperature distribution and enhanced growth rate as not only the susceptor, but also all other surfaces are heated. The main drawback of this configuration is that coating may occur also onto the reactor walls leading to fouling and precursor losses;

- *cold wall reactors*, where only the susceptor is heated. Despite the lower growth rates, this design usually achieves better film quality.

Due to their properties, hot wall reactors are often employed with polycrystalline films, while the cold wall option fits processes operating with epitaxial films growth.

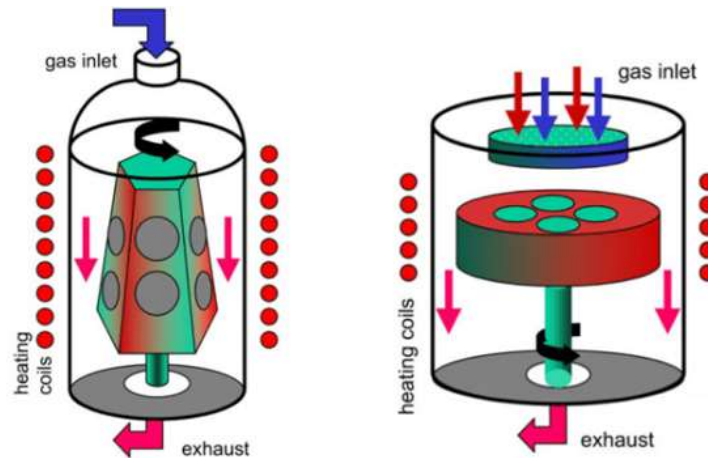

Figure 1.8: *barrel (left) and vertical disk (right) reactors*[4].

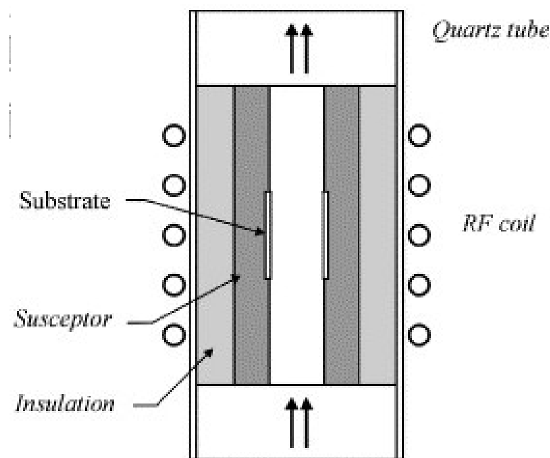

Figure 1.9: *chimney reactor*[12].

To limit gas phase reactivity and simultaneously improve surface deposition, TCVD reactors operate in atmospheric or sub-atmospheric ($P \approx 10\ \mathrm{mtorr}$) conditions: in the former case gas phase reactions are still relevant and the presence of a significant boundary layer[9] leads to a mixed control of the growth rate determined by both kinetics and mass transport, which can lead to homogeneous reactions of the precursors inside the gas phase, i.e. premature formation of unwanted solid particles colliding onto the substrate, and ultimately alter film uniformity; on the other hand, at low pressures the growth rate is mainly controlled by surface chemistry due to the enhanced gas diffusivity and the reduced partial pressures of the reactants. Furthermore, if precursors are volatile enough there is no need of a carrier gas, but higher precursors concentration in the gas phase is required to compensate for the lower pressure.

1.1.5 Thermal CVD Process Layout

Common features of all TCVD reactors are a precursor delivery section followed by a growth chamber and an exhaust section. A simplified representation of a standard TCVD process scheme operating with liquid precursors is depicted in Figure 1.10.

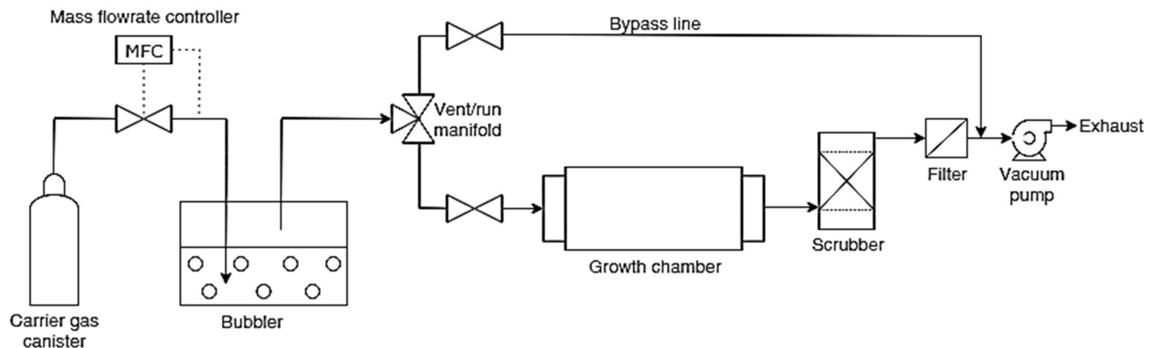

Figure 1.10: *TCVD process scheme.*

The delivery section includes a canister containing the pressurized carrier gas and a bubbler where liquid phase precursors are stocked; the bubbler consists of a sealed quartz/stainless steel container with a series of immersed tubes, to let the carrier gas gurgle inside the liquid mixture, and dip-tubes, to extract the carrier-precursors vapour.

Precursors transport rate is regulated manipulating the bubbler feed with a feedback controller, while a mechanical pressure regulator attached to the canister equalizes the gas pressure to the one of the delivery system. The flow of reactants from the bubbler to the growth chamber is then stabilized through a vent-run manifold where the entire stream is purged in a bypass line (vent mode) until it is ready to enter the growth chamber (run mode) with the wanted composition. Reactor effluent enters the exhaust section, where it is scrubbed and filtered through molecular sieves and cryogenic traps to remove harmful vapours, droplets and solid particles from the gas before discharging it in the atmosphere.

The required suction to ensure both gas circulation through each component of the system and low pressure inside the growth chamber is provided by a high vacuum pump selected in terms of operating pressure, pumping speed, i.e. volume of gas removed per unit of time, costs and working environment; it is possible to distinguish two main categories of vacuum pumps: gas transfer pumps, which establish suction by physically expelling gas from the system, and gas capture pumps, where suction is provided by gas molecules adsorption or condensation over dedicated surfaces. Gas capture pumps usually achieve lower pressures than gas transfer pumps, but their pumping speed decay in time as the adsorption surface becomes saturated so they require periodical maintenance.

Pump Type	**Operating Range [Torr]**	**Pumping Speed [l/s]**
Turbo-drag hybrid	10^{-11}	$50 \div 3200$
Turbomolecular	$10^{-7} \div 10^{-10}$	$30 \div 3500$
Molecular drag	10^{-6}	< 10
Oil diffusion	10^{-4}	$30 \div 50000$
Screw	10^{-3}	$15 \div 140$
Rotary vane	$10^{-2} \div 10^{-3}$	$0.5 \div 325$
Scroll	10^{-2}	$6 \div 13$
Diaphragm	$1 \div 10$	< 5

Table 1.2: *comparison between various vacuum pumps, data gathered from Jones and Hitchman*[9].

1.2 Silicon Carbide

Silicon carbide[13] discovery is accredited to the swedish chemist Jöns Jacob Berzelius (1810), who observed carbon and silicon aggregation to give a hard crystalline structure; while SiC was also accidentally synthesized in an attempt to recrystallize carbon into diamond using a potential gradient, by Despretz in 1849 and then by Marsden in 1881, Edward Goodrich Acheson was the first to identify the compound chemical composition and its molecular formula in 1891. SiC is scarcely found in nature from meteoritic fragments as moissanite, a hard greenish mineral discovered by the chemist Henri Moissan in 1893.

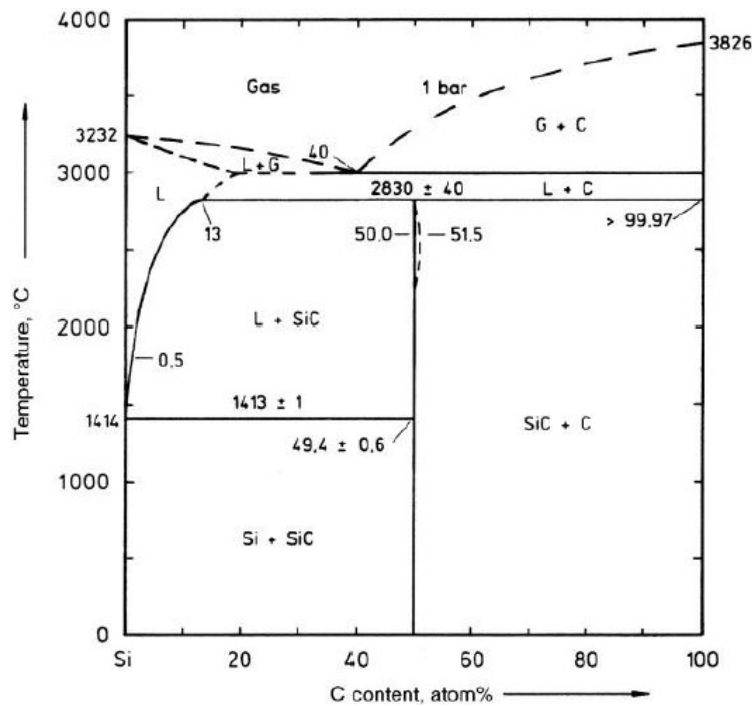

Figure 1.11: *silicon carbide phase diagram*[13].

Molecular Weight [kg/kmol]	Density [kg/m³]	Melting Point [K]	Crystal Structure
40.097	3200	3103±40	Cubic, hexagonal, rhombohedral.

Table 1.3: *silicon carbide main physical properties*[13] *at standard conditions* (298 K, 10^5 Pa).

1.2.1 Silicon Carbide Crystalline Structure

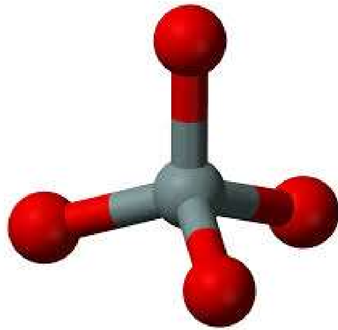

Figure 1.12: *SiC base tetrahedron. The central grey atom represents C (or Si) while red atoms at the vertices are Si (or C if the central atom is Si); the length of the Si-C bond is equal to 1.89 Å, while the distance between two Si or two C atoms inside the covalent network is 3.08 Å.*

SiC structure consist of a covalent network made of interconnected tetrahedra with a central carbon/silicon atom surrounded by four silicon/carbon atoms located at the vertices. These tetrahedra are linked through their corners to form several allotropic structures, known as *polytypes*: all polytypes share an identical two dimensional double layer made of a Si atomic plane and a C atomic plane, what changes is the stacking sequence of these bilayers in the third dimension; more than 250 polytypes have been discovered through the years, but the most common are the β-SiC (3C-SiC), a cubic lattice stable at temperatures below 2273 K, and the α-SiC (6H-SiC), a hexagonal lattice stable above 2273 K. While all polytypes have common mechanical characteristics, they are not equal in terms of thermal and electrical properties because of their different electronic mobility, i.e. 4H-SiC and 6H-SiC have larger thermal conductivity than 3C-SiC.

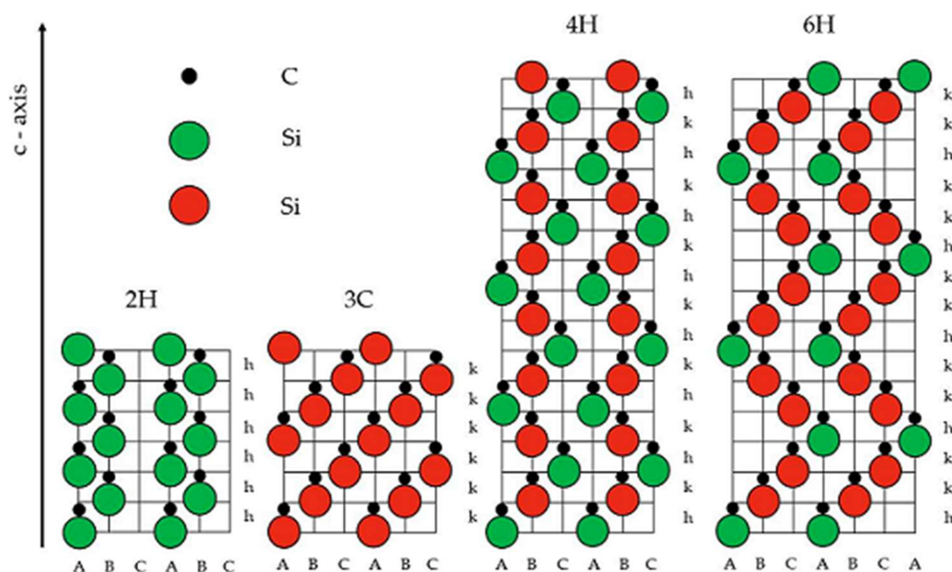

Figure 1.13: *main SiC polytypes according to Ramsdell notation*[14]*, which indicates both the number of layers defining the packing sequence and the structure of the unit cell (C for cubic and H for hexagonal).*

1.2.2 Silicon Carbide Properties, Applications and Role in the Electronics Industry

Although SiC has been an industrial product for over a century, it still retains an important role not only in the production of abrasives and refractory materials, due to the high hardness and chemical inertia provided by the Si-C covalent network coupled with a low thermal expansion coefficient and high thermal conductivity, but also in the manufacturing of wide-bandgap semiconductors thanks to excellent electrical properties which make SiC suitable for the realization of electronic equipment able to work in harsh environments at high voltages and current densities. these latter properties can be further tuned by p-type doping with trivalent elements (Al, B) or n-type doping with pentavalent species (P, N) to obtain small power devices like diodes, transistors and thermal sensors.

For the time being, the strongest contenders within wide-bandgap semiconductors are SiC and gallium nitride (GaN). The key features of these compounds, compared to pure silicon, are reported in Table 1.4: the high bandgap and breakdown electric field of both SiC and GaN enable the construction of medium to high voltage power devices operating in a larger temperature window than Si components; moreover, GaN is superior to SiC in terms of electronic mobility and drift velocity, thus it is the ideal candidate for high frequency applications like switching power supplies and AC adapters. Anyhow, GaN low thermal conductivity, almost four times smaller than SiC, leads to poor heat transfer and possible overheating risks: these issues compromise GaN performances at high voltages and so SiC remains the material of choice when working in extreme conditions.

Properties at 300 K	**Si**	**3C-SiC**	**4H-SiC**	**6H-SiC**	**GaN**
Bandgap [eV]	1.12	2.3	3.03	3.26	3.45
Breakdown Electric Field [10^6 V/m]	30	200	220	250	200
Electronic Mobility [$m^2/V/s$]	0.15	0.08	0.1	0.05	0.125
Drift Velocity [10^5 m/s]	1	2.5	2	2	2.2
Thermal Conductivity [W/m/K]	150	320	490	490	130
Maximum Working Temperature [K]	423	773	1033	1033	1073

Table 1.4: *intrinsic properties of Si and wide-bandgap semiconductors*[15].

While it is clear that GaN and SiC are the go-to species for the midrange voltage market with remarkable efficiency and power density advantages compared to pure silicon, the latter has cemented its role as leading commodity in the production of the most common and widespread low power devices (mobile phones, personal computers). This fact can be explained by the prohibitive price associated to wide-bandgap semiconductors together with their ideal operating range in terms of voltage; however, the demand for smaller and more performant electronic components keeps growing and in a certain future GaN and SiC could move from their niche markets and start to compete with Si on a global scale.

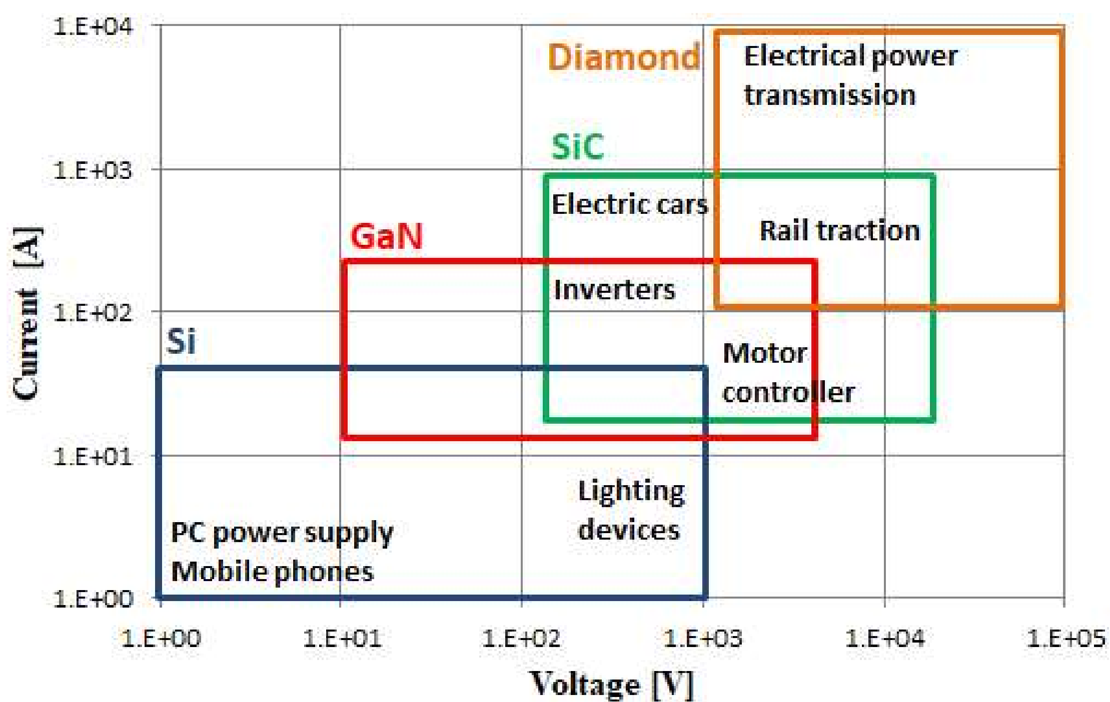

Figure 1.14: *operating range of Si, SiC, GaN and diamond in the semiconductor industry.*

Eventually, silicon carbide hardness and thermal shock resistance are exploited in the automotive sector for the manufacturing of carbon-ceramic brake disks, also known as C/SiC brake disks[16]: most prominent qualities of this product are high wear and corrosion resistance, high friction coefficient, light weight and good thermal management; once again, the limiting factor of this technology is represented by its costs, thus for now its use is limited to race and luxury cars while over the years it will probably replace common cast iron brake disks.

1.2.3 History of SiC Production Routes

Prior to the advent of silicon carbide semiconductors, the first industrial synthesis for the manufacturing of SiC abrasive pastes using an electric furnace was patented in 1896 by Acheson[17], who accidentally obtained silicon carbide crystals while trying to produce diamond from clay and powdered coke heated by means of an electrode; due to the abundancy of the raw materials and the high capacity, this batch process is still competitive nowadays: modern Acheson furnaces employ a graphite electrode surrounded by a 60:40 wt. % clay:coke mixture heated at temperatures close to 2273 K for 36 hours and further cooled[18]. The acknowledged SiC synthesis mechanism involves heterogeneous phase interactions between gaseous SiO and solid C[19], while the global reaction describing the process is:

$$\mathrm{SiO_2}^{(s,l)} + 3\ \mathrm{C}^{(s)} \rightleftarrows \mathrm{SiC}^{(s)} + 2\ \mathrm{CO}^{(g)} \qquad \mathit{SiC\ formation\ from\ silica\ and\ coke}\ \text{(R1.1)}$$

Working with coke excess, $\frac{C}{SiO_2} > 3$ or $\frac{SiO_2}{SiO_2+C} < 0.25$, ensures SiC formation and reduces the content of by-products and unreacted species.

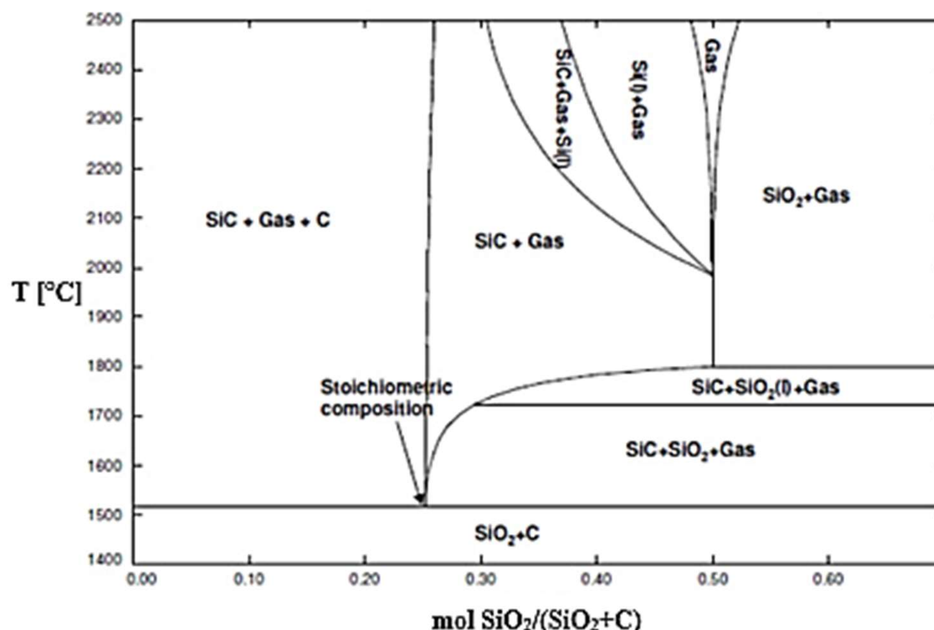

Figure 1.15: *SiO_2 – C calculated phase diagram[19]. Silicon carbide is formed at temperatures higher than 2073 K only if the reactants stoichiometric ratio is lower than 0.5.*

Inside the furnace, the reacting mixture gradually forms an amorphous SiC coarse shell around the hot core electrode followed by a SiC crystalline layer and a firesand zone, while unreacted SiO vapours migrate from the centre towards the reactor wall together with CO and CO_2. In this phase it is mandatory to control the core temperature[17] as if it is too high then SiC decomposes into volatile Si and solid graphite which accumulates around the electrode dangerously enhancing its dimensions and its conductivity; once the furnace run is completed, the SiC ingot is fragmented, finely granulated and treated to meet the required specifications.

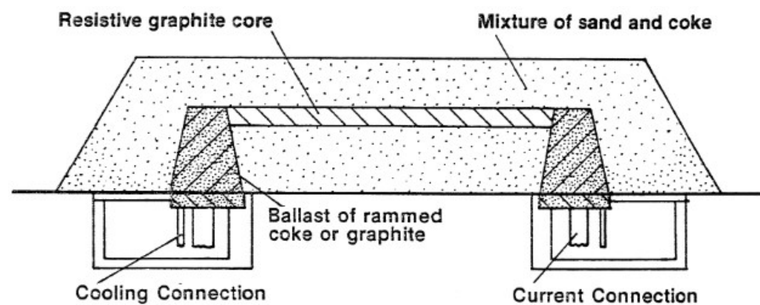

Figure 1.16: *Acheson furnace[18]. The obtained SiC ingot is mostly made of α-SiC with an outer β-SiC annulus due to the decreasing temperature trend.*

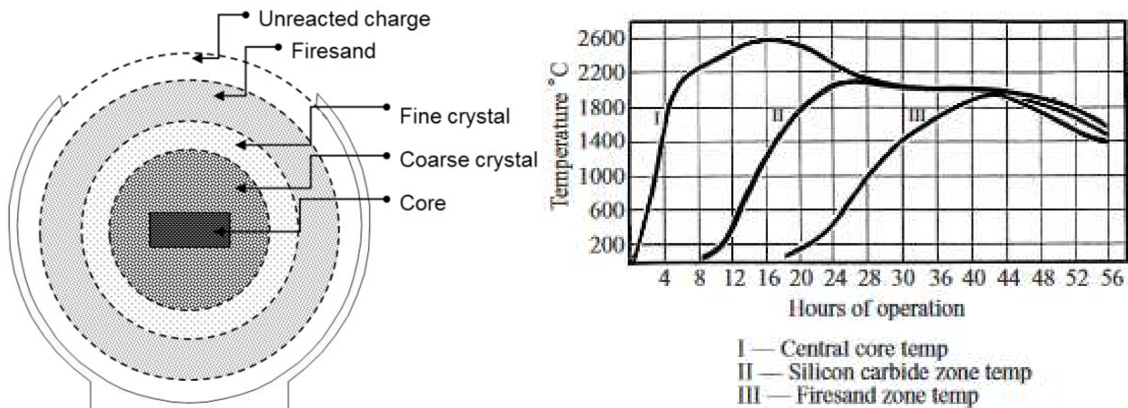

Figure 1.17: *cross section of an Acheson furnace[20] and temperature profile[18] over time for each zone. Temperature radially decreases moving from the core electrode to the outer layers.*

Despite the large production volumes, the main drawback of the Acheson synthesis are the presence of pollutant gaseous by-products in large quantities (up to 1.4 tons of CO per ton of SiC produced, which gets oxidized inside the furnace to give CO_2) and the high amount of energy input required to provide the necessary heat to the system.

Among all the emerging methods experimented to produce silicon carbide for the semiconductor industry in the '50s, one of the most effective was the sublimation growth process invented by Jan Anthony Lely[21] in 1958. Differently from the Acheson process, the raw material for this method is SiC itself; indeed, rather than a direct synthesis, the Lely process can be seen as a purification of commercial silicon carbide from its metallic impurities through sublimation, followed by a nucleation phase where SiC morphology shifts from polycrystalline to monocrystalline: powdered polycrystalline SiC is loaded inside a graphite crucible internally coated with a SiC inner liner, where it is heated in a rarefied inert gas atmosphere at temperatures close to 2773 K[21] in order to enhance SiC sublimation and decomposition forming gaseous Si_2C, SiC_2 and Si. Then, these species deposit onto an ad hoc surface, either the crucible lid or a graphite rod, kept at a lower temperature and covered with seed crystals to enhance monocrystalline SiC nucleation.

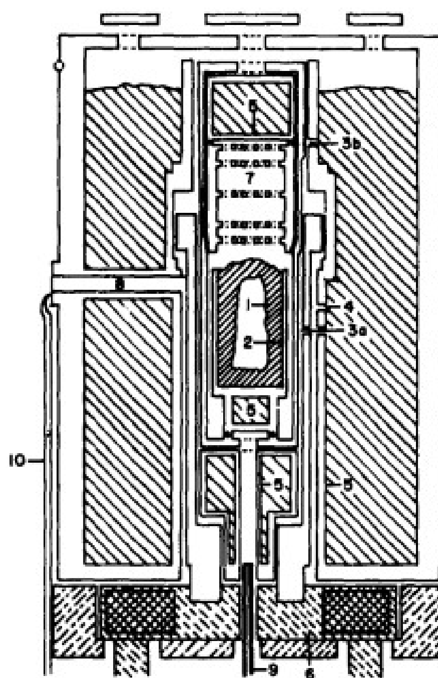

(1) SiC for sublimation; (2) graphite crucible; (3) graphite crucible made of two parts for protection of Sic; (4) heating element, a graphite tube split three-fourths of its length; (5) insulating body made with graphite lampblack; (6) water-cooled copper electrodes; (7) graphite network; (8) tube for pyrometer; (9) tube for introducing protective gas; (10) protective gas inlet. The furnace is surrounded by a water-cooled vacuum-type envelope.

Figure 1.18: *Lely furnace*[22].

Currently, Research & Development efforts are focused on a modified version of sublimation growth, known as Physical Vapour Transport, capable to solve the low reproducibility of Lely's process from one furnace batch to another due to the high temperature gradients involved.

Further progress in fabrication of silicon carbide semiconductors were made in 1969 with Liquid Phase Epitaxy, a thermal driven solution growth technique developed by Brander and Sutton[23]. The first LPE system consisted of a heated graphite crucible divided in a hot top zone, containing solid silicon lumps, and in a colder bottom zone, where α-SiC substrate crystals grown using Lely's method were supported by graphite clamps; the required temperature gradient between the two zones was achieved by varying the dimension of the heating elements placed next to the crucible, working with a top temperature of 2173 K and a bottom temperature of 2073 K[23]. Once the system has reached the operating temperature, silicon lumps start to melt forming a liquid phase which moves towards the bottom zone: liquid Si then reacts with the crucible inner graphite walls forming SiC crystals that dissolve during the run releasing carbon until the melt becomes saturated and equilibrium is reached. Then, mixture temperature is reduced so carbon solubility drops reaching a lower saturation concentration and simultaneously growing β-SiC epitaxial crystalline layers onto the substrate (the apparatus work in a temperature range higher than silicon melting point so only silicon carbide can exist in solid phase[24]). At the end of the run the system is cooled and SiC crystals are recovered by cutting the top zone while the remaining solid Si is dissolved in a HF-HNO_3 solution[23].

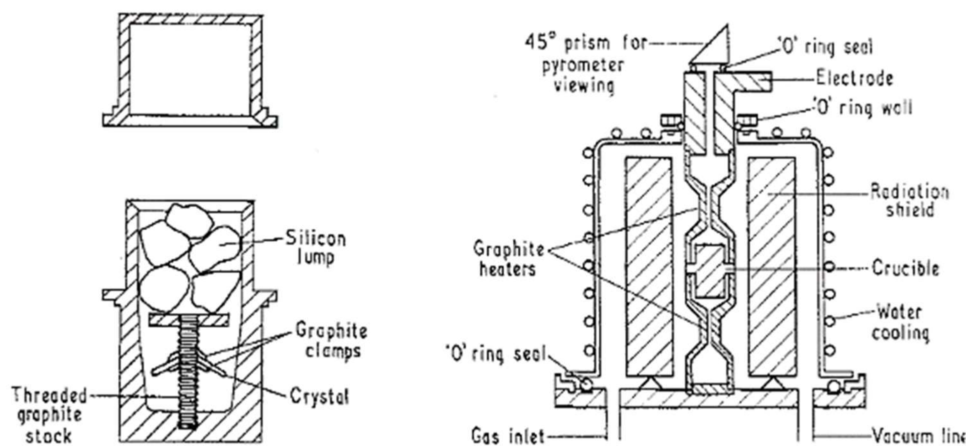

Figure 1.19: *original LPE apparatus (left) with its graphite lid (left-top) and LPE furnace (right)*[23].

The process is still in use as it allows to form silicon carbide crystals at lower temperatures than its predecessors in a more controlled manner: over the years alternative melts made of mixtures of Si and Group 13 (Ga) or Group 14 (Ge, Sn) metals were tested together with various dopant agents like Al, B and N.

A generic comparison between chemical vapour deposition and other SiC production routes can be made in terms of operating conditions and product quality: the Acheson process has no control over impurities incorporation, it has high energy consumptions while producing high amounts of pollutant species; moreover, crystals obtained from ingot fragmentation largely exceed the required dimensions for applications in the semiconductor industry (actually, this process was not even conceived to meet these requirements as silicon carbide electronic properties were yet to be discovered at the time) so they are used almost exclusively for abrasives production or metallurgical purposes. At the same time, PVT gives smaller and purer SiC crystals, but, as already said, it is difficult to replicate the same quality for each batch due to the poor thermal control over the system; an improvement is represented by the LPE method, characterized by higher growth rates and better product quality than PVT with the advantage of working at lower temperatures. Anyhow, both methods have been gradually replaced by chemical vapour deposition over the years[25] due to its extreme versatility and product quality, although it is an expensive technique so LPE and PVT are still employed for some niche applications.

Process	**Operating Conditions**	**Product**
Acheson	2273 K, 1 bar Run time: days	Green α-SiC (abrasives) Black α-SiC (abrasives) Metallurgical α-SiC
Lely (PVT)	2773 K, 1 bar, inert atm. Run time: hours	α-SiC (semiconductors)
LPE	2073÷2273 K, 1 bar Run time: hours	β-SiC epitaxial crystals (semiconductors)
CVD	300÷2273 K, ≤1 bar Run time: minutes	α-SiC epitaxial crystals (semiconductors) β-SiC epitaxial crystals (semiconductors)

Table 1.5: *comparison between main SiC production routes. Black and metallurgical α-SiC are obtained by recycling the unreacted charge of previous furnace runs and have more impurities than green α-SiC synthesized from the starting raw materials.*

1.3 Overview on n-type Doping of Silicon Carbide

The first dopant incorporation control technique based on tuning of the C/Si ratio was developed in 1994 by the pioneer work of Larkin et al.[26,27]. Experimental tests in a CVD reactor, operating with different C/Si ratios ranging from 2 to 10, led to the formulation of the site-competition epitaxy criteria: due to their similar dimensions, i.e. similar atomic radii, C and N atoms compete for C sites inside SiC lattice while Si and Al do the same for Si sites; it was found that N and Al incorporation could be enhanced respectively decreasing carbon and silicon composition inside the feeding mixture.

Nitrogen incorporation patterns for the 4H-SiC polytype were studied by Yamamoto et al.[28] and Kojima et al.[29]. Assuming nitrogen incorporation to occur on both Si and C polar faces of the 4H-SiC crystal, the models proposed by these authors theorized four different possible configurations: on Si faces, N incorporates either on the terrace surface, forming a single bond with a Si atom ("1-Si" configuration), or at the terrace edges, forming two bonds with two Si atoms (2-Si); on C faces, N incorporates on the terrace surface, bonding with one or more Si atoms (2-C), or at the terrace edges, forming only one bond with a Si atom (1-C).

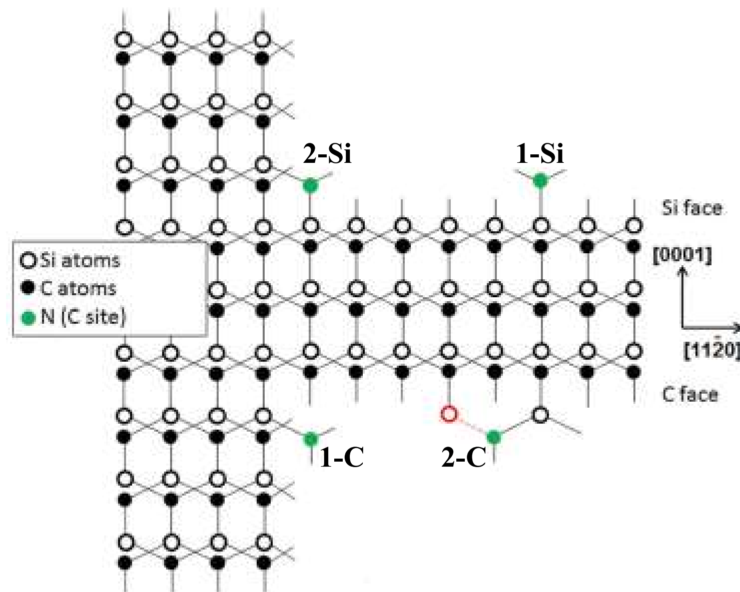

Figure 1.20: *possible N incorporation sites on both Si and C polar faces of a 4H-SiC crystal*[28,29] *(the red dot is a silicon atom).*

On a thermodynamic basis, configurations 1-Si and 1-C are less likely to occur as only one bond is formed and less energy is released so that the favoured cases seem to be 2-Si and 2-C. However, experimental evidences[28,29] have shown that N incorporation is higher on C faces rather than Si faces and a physical explanation of these results is still yet to be determined.

Kojima et al.[29] and Zang et al.[30,31] investigated the effect of C/Si ratio over N doping through test runs in CVD reactors. In these experiments, dopant atomic density inside the SiC lattice showed a decreasing trend when moving from silicon-rich conditions $(\mathrm{C/Si} \ll 1)$ to carbon-rich conditions $(\mathrm{C/Si} \gg 1)$, coherently with the site-competition criteria introduced by Larkin, though for intermediate conditions $(\mathrm{C/Si} \approx 1)$ there is no general agreement. Indeed, it is possible to assume that N incorporation in this region largely depends by reactor geometry[30,31].

Results obtained by these research groups also shown an inverse proportion between temperature and C/Si ratio: it is believed[32] that high temperatures may boost H_2 etching $\left(\mathrm{H_2^{(g)}} + \mathrm{C_x^*} \rightarrow \mathrm{C_xH_y}^{(g)}\right)$ so that C/Si ratio inside the reactor decreases as carbon is lost inside the carrier gas; the exact opposite phenomenon appears for low temperatures.

In recent years, Ferro and Chaussende[32] studied doping trend with respect to pressure by fitting data gathered from literature with Henry's law. It was found that N incorporation rate is directly proportional to pressure: the authors assume that this could be related to the fact that higher pressures imply higher hydrogen concentrations inside the reactor, i.e. higher etching, which ultimately reduce the C/Si ratio; at the same time, low pressures may cause Si sublimation from the silicon carbide matrix to the carrier gas and also less etching due to the reduced H_2 concentration resulting in higher C/Si ratios and so lower nitrogen incorporation.

Trying to provide a theory of everything able to justify n-type doping dependence from temperature, pressure and C/Si ratio, Ferro and Chaussende also obtained satisfying results with a new model based on the dynamic evaporation equilibrium between carbon atoms leaving the uppermost layers of the SiC matrix through etching and N atoms occupying the resulting vacancies while taking into account N desorption, particularly effective at high temperatures.

1.3.1 State of the Art of SiC Growth and Doping through CVD

A first theoretical study[33] of Si-C-H systems was done by Allendorf and Melius, which calculated the heat of formation for numerous organosilicon species, $H_xSi_yC_z$, through ab-initio methods combined with empiric correlations. These data were implemented into a kinetic scheme[34] tested on the model of a CVD rotating disk reactor[35] using SiH_4 and C_3H_8 respectively as Si and C precursors. At mild temperatures ($T = 1773 \div 1873\ K$), it was found that the growth rate of the system was controlled by C_2H_2 surface deposition (propane decomposes through pyrolysis to give CH_4 and C_2H_4, the latter further decomposes into C_2H_2 and hydrogen), slower than Si deposition.

Danielsson et al. performed 3D simulations[36] of a CVD reactor operating with the same precursors and range of temperature employed by Allendorf. The introduction of sticking coefficients allowed a better calculation of the adsorption rates, which ultimately resulted in a more detailed surface reactivity able to account for SiC parasitic growth on the reactor walls. Anyhow, the authors had to assume all surface reactions as irreversible due to the lack of proper thermodynamic data.

One of the first kinetic schemes including chlorosilanes was developed and tested on a horizontal CVD reactor by Veneroni and Masi[37]. Instead of the classic silane-propane-hydrogen composition reported in the previous works, HCl was added to the feeding mixture: this addition resulted in an enhanced gas phase reactivity due to the formation of chlorosilane intermediate species with an overall growth rate increase. The addition of hydrochloric acid also seemed to counter gas phase nucleation, i.e. unwanted formation of condensed clusters of particles in the gas phase leading to precursors losses, as the authors observed no silicon droplets in the gaseous outlet of the reactor.

A simplified kinetic model for n-type doping involving both gas and surface reactivity was tested by Fiorucci et al.[38]: assuming negligible interactions between growth and doping mechanisms, it was found that the doping-controlling reaction is N_2 dissociative adsorption and that surface reactions between nitrogen and Si free sites play a key role in the process. Moreover, the authors have shown that nitrogen incorporation inside the silicon carbide lattice is inversely proportional to SiC film growth rate.

Cavallotti et al.[39] further investigated n-type doping with the development of a kinetic scheme involving SiC deposition and N_2 decomposition in presence of chlorinated species. Simulation performed with a 1D heterogeneous model confirmed the effect of chlorosilane intermediates on the growth rate observed by Veneroni and Masi[37] and found that nitrogen incorporation rate is proportional to the square root of N_2 partial pressure.

1.4 Thesis Purpose and Methodology

The aim of the present study is to provide a comprehensive analysis of the kinetics and fluid dynamics related to silicon carbide film growth and n-type doping with nitrogen carried inside the PE-106 chemical vapour deposition reactor of LPE S.p.A.; such analysis relies on a kinetic scheme and a monodimensional model developed by various authors[37,38,39], both implemented in a Fortran software programmed by the same authors.

Initially, the work was focused on improving certain features of the employed program in an attempt to enhance its physical consistency and adherence with the real reactor, taking as reference a baseline numerical simulation which tries to reproduce the experimental trends of SiC growth rate and N incorporation gathered from two test runs. This phase also proved useful to perform other simulations in order to identify the main parameters involved in the kinetics of the process and test their impact onto the system.

Then, the second step shifted the attention to the experimental nitrogen doping trend and its anomalies: especially, uneven nitrogen incorporation along and horizontally with respect to the flow direction was investigated, first with a simplified monodimensional simulation and later with a detailed 3D model based on a pre-existing Fluent® model able to accurately describe the fluid dynamics and geometry of the system.

CHAPTER 2

Modelling of a CVD System and Computational Aspects

Chapter 2 aims to give an in-depth comprehension of the software and mathematical model utilized to perform the numerical simulations presented in this thesis; experimental data gathered prior to this work are introduced in the final part of this chapter in order to clarify what were the major issues and anomalies and how they could be possibly solved.

Section 2.1 introduces a steady-state formulation of the equations involved in a CVD system, followed by the full mathematical derivation of the model employed in this work.

Then, Section 2.2 contains the kinetic scheme related to silicon carbide film growth with nitrogen incorporation, as it is featured in the software used to carry the calculations.

Section 2.3 deals with the layout of the PE-106 epitaxy reactor patented by LPE S.p.A., the object of this study, describing the geometry and the role of each of its components.

The structure of the program chosen to run the 1D simulations, along with the most relevant modifications done in this work, is introduced in Section 2.4.

The outcome of two test-runs conducted with PE-106 is analysed in Section 2.5.

2.1 Governing Equations for a CVD Reactor

Modelling of a CVD reactor involves the solution of mass, momentum, species and energy conservation equations. As the growth rate is relatively small compared to the average residence time of an epitaxial CVD process, it is possible to write these equations in a steady-state formulation in order to describe the gas phase behaviour and its interaction with the deposition surface: the steady-state model proposed in this work, together with its mono-dimensional derivation, is the one developed by Carrà and Masi[40].

$$\nabla \cdot (\rho \boldsymbol{u}) = 0 \qquad \textit{Mass conservation (continuity equation)} \quad (2.1)$$

$$\boldsymbol{u} \cdot \nabla(\rho\omega_i) = W_i \sum_{j=1}^{NRG} \nu_{ij}^G R_j^G + \nabla \cdot \left[\rho\Gamma_i\left(\nabla\omega_i - \alpha_{T,i}\omega_i \nabla \ln T\right)\right] \qquad \textit{Species cons.} \quad (2.2)$$

$$\rho\widetilde{c_p}\boldsymbol{u} \cdot \nabla T = \nabla \cdot \lambda_T \nabla T - \sum_{j=1}^{NRG} R_j^G \Delta H_{R_j}(T) \qquad \textit{Energy conservation} \quad (2.3)$$

$$\rho\boldsymbol{u} \cdot \nabla\boldsymbol{u} = -\nabla P + \nabla \cdot \left[\mu(\nabla\boldsymbol{u} + \nabla\boldsymbol{u}^{\boldsymbol{T}}) - \frac{2}{3}\mu(\nabla \cdot \boldsymbol{u})\boldsymbol{I}\right] + \rho\boldsymbol{g} \qquad \textit{Momentum cons.} \quad (2.4)$$

$$\rho = \frac{P}{R_{gas}T}\frac{1}{\sum_{i=1}^{NCG}\frac{\omega_i}{W_i}} \qquad \textit{Equation of State} \quad (2.5)$$

ρ, $\boldsymbol{u}$, $\widetilde{c_p}$, λ_T, μ respectively represent mixture density, velocity vector, mass specific heat, thermal conductivity, and dynamic viscosity while T and P are the temperature and pressure of the gas phase; ω_i, W_i, Γ_i, $\alpha_{T,i}$ are the mass fraction, molecular weight, material diffusion coefficient, and thermophoretic diffusion coefficient referred to the i-th species.

ν_{ij}^G, R_j^G, $\Delta H_{Rj}(T)$ are the stoichiometric coefficient of the i-th species in the j-th reaction, reaction rate of the j-th reaction and enthalpy variation of the j-th reaction ("G" denotes the gas phase); $\boldsymbol{g}$ represents gravitational acceleration, while $\boldsymbol{I}$ is the identity matrix.

Eq. (2.2) accounts for material and thermal driven diffusion, expressed with Fick and Soret laws: since in this work most of the carrier gas consists of H_2, material diffusion coefficients are computed as binary coefficients between each i-th species and hydrogen.

The heat of reaction, $-\sum_{j=1}^{NRG} R_j^G \Delta H_{Rj}(T)$, can be considered null as CVD systems are characterized by low conversions[4] and the carrier gas provide a thermal diluent effect.

The term accounting for field forces in Eq. (2.4) degenerates to $\rho\boldsymbol{g}$ as the main forces involved in the process are gravity and buoyancy[41] due to density variations. Moreover, density, temperature and composition interactions are described by the ideal gases EoS as the operating pressure of many CVD systems is lower than the atmospheric one.

Once the equations have been defined it is still necessary to implement proper boundary conditions to make the solution unique: this can be achieved by specifying inlet flow rate and composition together with temperature at the inlet and at the walls of the reactor; no slip condition, i.e. velocity at the surface is null, is valid not only at the reactor walls, but also on the deposition surface, i.e. average macroscale velocity of adsorbed/desorbed atoms at the growing film is negligible[4]. At the reactor outlet the flow is fully developed.

The last boundary condition is represented by flux continuity at the gas-surface interface:

$$-\rho\Gamma_i\hat{\boldsymbol{n}}\cdot\left(\nabla\omega_i - \alpha_{T,i}\omega_i\nabla\ln T\right) = W_i\sum_{j=1}^{NRS}\nu_{ij}^S\,R_j^S \qquad \textit{Interface flux continuity} \ (2.6)$$

$\hat{\boldsymbol{n}}$ is the outward pointing versor normal to the deposition surface, ν_{ij}^S is the i-th species stoichiometric coefficient in the j-th surface reaction, whose reaction rate is R_j^S.

Eq. (2.6) states that the total diffusive mass flux of a species (left-hand side of the equation) from the gaseous bulk to the deposition surface must be equal to the reactive surface flux, equal to the net production rate onto this surface (right-hand side of the equation).

Film growth rate can be defined as the sum of the net incorporation rates of each species onto the film[4]:

$$G.R. = \frac{W_{film}}{\rho_{film}} \sum_{i=1}^{NC_{film}} \sum_{j=1}^{NRS} \nu_{ij}^{S} R_{j}^{S} \qquad Growth\ rate\ (2.7)$$

W_{film}, ρ_{film} are the film molecular weight and mass density. If the carrier gas includes a doping precursor, then the dopant molar fraction inside the film is defined as the ratio between the dopant incorporation rate and the growth rate of the limiting growth precursor, both expressed as molar fluxes towards the deposition surface:

$$x_{dopant} = \frac{n_{dop.}}{n_{dop.} + n_{pre.}} \approx \frac{n_{dop.}}{n_{pre.}} = \frac{n_{dop.}}{\frac{G.R.}{V_{pre.}}} = V_{pre.} * \frac{n_{dop.}}{G.R.} \qquad Dop.mol.fraction\ (2.8)$$

x_{dopant} is the dopant molar fraction within the film, $n_{dop.}$ and $n_{pre.}$ respectively stands for the dopant and the limiting film precursor molar fluxes towards the deposition surface (usually the former is way lower than the latter as it is added only in minor quantities in the carrier gas); $V_{precursor}$ is the film precursor molar volume.

Eventually, it is worth noting that turbulent transport contributions intrinsically contained in the right-hand side of conservation equations are negligible as CVD systems operate in laminar regime due to the low viscosity of the gaseous flow at low pressures and high temperatures. A more detailed dissertation about conservation equations can be found in the work of Kee et al.[41].

2.1.1 One Dimensional Heterogeneous Reactor Modelling

A horizontal disk CVD reactor can be seen as a specific case of the heterogeneous Plug Flow Reactor, where mass is exchanged from the gas phase to the deposition surface in order to promote film growth; reactions will occur in both the gas and at the gas-solid interphase. Gas flow velocity can be taken as constant, whilst pressure drops inside the reactor are considered negligible and fully compensated by the presence of a vacuum circulation pump: this assumption allows to avoid the inclusion of momentum conservation and Ergun equations, which will otherwise make the system solution less smooth from a computational point of view. If this is valid, it is now possible to simplify the set of conservation equations from Eq. (2.1) to Eq. (2.4), leading to the formulation of a mono-dimensional heterogeneous model.

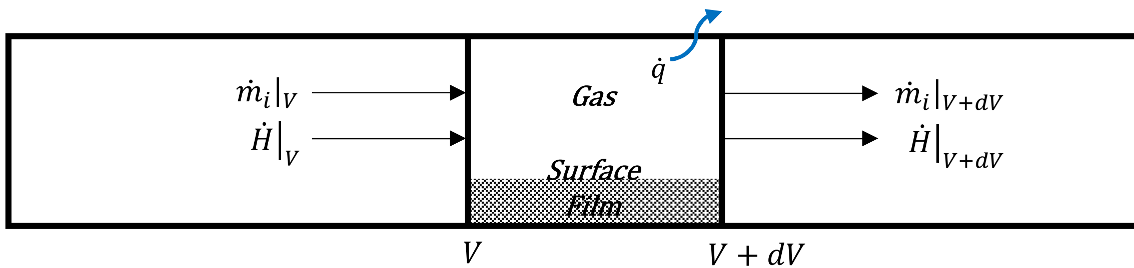

Figure 2.1: *heterogeneous model of a horizontal CVD reactor; radiative pre-heating is assumed to occur before the reactive section of the reactor, so both surface and gas temperature profiles over the deposition zone are almost isothermal.*

Consider an infinitesimal control volume dV, which contains both gas and solid phases, of the heterogeneous PFR shown in Figure 2.1: the i-th species material balance in steady-state conditions over this control volume will be written as

$$\frac{dm_i|_V}{dt} = 0 = \dot{m}_i|_V - \dot{m}_i|_{V+dV} + W_i\left(\sum_{j=1}^{NRG} \nu_{ij}^G R_j^G + S_V \sum_{j=1}^{NRS} \nu_{ij}^S R_j^S\right) dV \tag{2.9}$$

Eq. (2.9) states that the variation in time of the total mass of the i-th species, approximated equal to the mass of the i-th species contained inside the gas phase only ($m_i|_V$), due to the net convective flow of species i ($\dot{m}_i|_V - \dot{m}_i|_{V+dV}$) and its transformation rate, is null. S_V accounts for the active surface, i.e. ratio deposition surface to reactor volume.

Expanding the outlet flowrate term, $\dot{m}_i|_{V+dV}$, with a Taylor series leads to:

$$\dot{m}_i|_{V+d} \quad = \dot{m}_i|_V + \left.\frac{d\dot{m}_i}{dV}\right|_{V+d} \; dV \tag{2.10}$$

Thus Eq. (2.9) becomes:

$$0 = -d\dot{m}_i + W_i \left(\sum_{j=1}^{NRG} \nu_{ij}^G R_j^G + S_V \sum_{j=1}^{NRS} \nu_{ij}^S R_j^S \right) dV \tag{2.11}$$

Rearranging Eq. (2.11) leads to:

$$\frac{d\dot{m}_i}{dV} = W_i \left(\sum_{j=1}^{NRG} \nu_{ij}^G R_j^G + S_V \sum_{j=1}^{NRS} \nu_{ij}^S R_j^S \right) \tag{2.12}$$

In other words, the i-th mass flowrate variation in space inside the control volume referred to gas and solid phases is equal to the i-th species transformation rate, accounting for both gas and surface reactivity. Considering the same control volume, this time referred to the gaseous phase only, the steady-state material balance for the i-th species will be:

$$\frac{dm_i|_V}{dt} = 0 = \dot{m}_i|_V - \dot{m}_i|_{V+dV} + W_i \sum_{j=1}^{NRG} \nu_{ij}^G R_j^G \, dV - S_V N_i dV \tag{2.13}$$

Variation in time of the i-th species mass inside the gas due to the net convective flux of i along with its gas phase transformation rate and its gas-surface diffusive flux N_i is null.

With the same procedure done for Eq. (2.9), Eq. (2.13) becomes:

$$\frac{d\dot{m}_i}{dV} = W_i \sum_{j=1}^{NR_G} \nu_{ij}^G R_j^G \, dV - S_V N_i \tag{2.14}$$

The i-th mass flowrate variation in space inside the control volume referred to the gas phase is equal to the sum of the i-th species transformation rate, accounting for gas reactivity only, and its diffusive flux. Total mass flowrate ($\dot{m}$) variation in the gas phase, is obtained summing Eq. (2.14) for all the gas phase species contained in the system:

$$\frac{d\dot{m}}{dV} = \sum_{i=1}^{NCG} \dot{m}_i = -\sum_{i=1}^{NCG} S_V N_i \tag{2.15}$$

The sum of all the gas phase transformation rates is null (mass conservation law), but the mass flowrate contained inside the gas phase still varies due to a diffusive contribute.

The interface flux continuity equation, stating that the gas-surface diffusive flux is equal to the surface reactive flux, is obtained by subtracting Eq. (2.14) from Eq. (2.12):

$$0 = W_i \left(\sum_{i=1}^{NRG} \nu_{ij}^G R_j^G + S_V \sum_{i=1}^{NRS} \nu_{ij}^S R_j^S \right) - \left(W_i \sum_{i=1}^{NRG} \nu_{ij}^G R_j^G \, dV - S_V N_i \right) \tag{2.16}$$

Resulting in:

$$-N_i = W_i \sum_{j=1}^{NRS} \nu_{ij}^S R_j^S \tag{2.17}$$

About the energy balance, it can be derived with the same approach. Considering a control volume dV including both phases, its energy balance in steady-state conditions will be written as the difference between the net enthalpic flow ($\dot{H}\big|_V - \dot{H}\big|_{V+dV}$) and the heat exchanged with the cooling fluid ($\dot{q}$):

$$\frac{dH}{dt} = 0 = \dot{H}\big|_V - \dot{H}\big|_{V+dV} - \dot{q}dV \tag{2.18}$$

Expanding the outlet energy stream with a Taylor series and rearranging the equation:

$$\frac{d\dot{H}}{dV} \approx \frac{d(\dot{m}\widetilde{cp}T_G)}{dV} = -\dot{q} \tag{2.19}$$

T_G is the gas-phase temperature. Spatial variation of the enthalpic flux equals the opposite of the heat leaving the system. Proceeding once again with the same strategy, the energy balance for the gas-phase will be:

$$0 = -d\dot{H} - \dot{q}dV - hS_V(T_G - T_S)dV \tag{2.20}$$

Where T_S is film surface temperature and h is the liminar heat transfer coefficient. Differently from Eq. (2.18), Eq. (2.20) contains an additional contribute given by the thermal flux between gas and deposition surface. Exploiting the term $d\dot{H}$ leads to:

$$d\dot{H} \approx d(\dot{m}\widetilde{cp}T_G) + \sum_{i=1}^{NCG} \widetilde{H}_i(T_G)d\dot{m}_i \tag{2.21}$$

being $\widetilde{H}_i$ the i-th species mass enthalpy.

Once $d\dot{m}_i$ has been substituted from Eq. (2.11), Eq. (2.21) becomes:

$$d\dot{H} \approx d(\dot{m}\widetilde{cp}T_G) + \sum_{i=1}^{NCG} \widetilde{H}_i(T_G)\left(\sum_{j=1}^{NRG} \nu_{ij}^G R_j^G + S_V \sum_{j=1}^{NRS} \nu_{ij}^S R_j^S\right) * W_i \, dV \tag{2.22}$$

The second term on the right-hand side correspond to the heat released by gas and surface reactions. If the contribute of surface reactivity is negligible, then:

$$d\dot{H} \approx d(\dot{m}\widetilde{cp}T_G) + \sum_{i=1}^{NCG} W_i \widetilde{H}_i(T_G)\left(\sum_{j=1}^{NRG} \nu_{ij}^G R_j^G\right) dV \tag{2.23}$$

Dividing by dV and switching the order of the summations at the right hand side gives:

$$\frac{d\dot{H}}{dV} \approx \frac{d(\dot{m}\widetilde{cp}T_G)}{dV} + \sum_{j=1}^{NRG} R_j^G \sum_{i=1}^{NCG} W_i \nu_{ij}^G \widetilde{H}_i(T_G) = \frac{d(\dot{m}\widetilde{cp}T_G)}{dV} + \sum_{j=1}^{NRG} R_j^G \, \Delta H_{R,j}(T_G) \tag{2.24}$$

Therefore, Eq. (2.20) is rearranged in its final form:

$$\frac{d(\dot{m}\widetilde{cp}T_G)}{dV} = -\dot{q} - hS_V(T_G - T_S) - \sum_{j=1}^{NRG} R_j^G \, \Delta H_{R,j}(T_G) \tag{2.25}$$

This relation asserts that the spatial variation of the enthalpic flux, approximated as the product of its thermal capacity $\dot{m}\widetilde{cp}$ and T_G, is equal to the net contribute of the heat exchanged with the cooling fluid, the heat transferred between gas and surface and the heat released/absorbed, depending on the sign of $\Delta H_{R,j}$, by all the j-th gas-phase reactions.

Interface flux continuity equation is obtained by subtraction of Eq. (2.25) from Eq. (2.19):

$$0 = -\dot{q} - \left(-\dot{q} - hS_V(T_G - T_S) - \sum_{j=1}^{NRG} R_j^G \, \Delta H_{R,j}(T_G) \right) \qquad (2.26)$$

Defining $\dot{q}$ as:

$$\dot{q} = US_e(T_G - T_C) \qquad (2.27)$$

U is the global heat transfer coefficient referred to the external exchange area, S_e is the ratio external exchange area to reactor volume and T_C stands for the coolant fluid temperature; Eq. (2.26) further simplifies into:

$$-hS_V(T_G - T_S) = \sum_{j=1}^{NRG} R_j^G \, \Delta H_{R,j}(T_G) \qquad (2.28)$$

If the enthalpic contribute of each gas-phase reaction is negligible then Eq. (2.28) has null thermal interface flux between gas and surface: excluding the trivial solutions of null heat transfer coefficient and null or very low active area, this is possible only if the equation reduces to $T_G = T_S$, meaning that there is no thermal gradient between the two phases.

The last step to complete the model is the implementation of the Pseudo Steady State Approximation for all species adsorbed on the surface: adsorbed species are consumed as quickly as they are generated, so net surface transformation rate for each species is null.

$$\sum_{j=1}^{NRS} \nu_{ij}^S R_j^S = 0 \qquad i = 1,2,\dots,NCA - N_{sites} \qquad (2.29)$$

Eq. (2.29) is applied to all species with the exception of the surface free sites (in this work N_{sites} is equal to 2 as it accounts either for a carbon or a silicon site of the silicon carbide lattice); indeed, the surface concentrations of these sites can be evaluated from the surface stoichiometric equation, which states that the total number of m-type surface sites, occupied and free, is constant:

$$\sum_{i=1}^{NCA_m} \theta_{m,i} = 1 \qquad m = 1, 2, \dots, N_{sites} \tag{2.30}$$

$\theta_{m,i}$ represents the coverage fraction of the i-th species on the m-th kind of surface site (m is an index denoting the type of site), i.e. ratio between concentration of the i-th species adsorbed onto m type sites and total number of m-type surface sites, while NCA_m is the number of components adsorbed onto the m-type sites. Eq. (2.30) is valid only if every surface species has the same surface occupation, if this is not true then it has to be rewritten to account its dependence on the i-th species valence ξ_i, i.e. number of surface dangling bonds occupied by species i:

$$\sum_{i=1}^{NCA_m} \xi_i \theta_{m,i} = 1 \qquad m = 1, 2, \dots, N_{sites} \tag{2.31}$$

In case of unitary valence, equation 2.31 reduces to Eq. (2.30).

It is now possible to write the full heterogeneous model for a CVD system featuring NCG gaseous species, NCA adsorbed species (including N_{sites} types of site), NRG gaseous reactions and NRS surface reactions:

$$\frac{d\left(\dot{m}\omega_i^G\right)}{dV} = W_i \sum_{j=1}^{NRG} \nu_{ij}^G R_j^G \, dV - S_V N_i \qquad \textit{Gas phase material balances}$$

$$\frac{d\dot{m}}{dV} = -\sum_{i=1}^{NCG} S_V N_i \qquad \textit{Global gas-phase material balance}$$

$$\frac{d(\dot{m}\widetilde{cp}T_G)}{dV} = -US_e(T_G - T_C) - hS_V(T_G - T_S) - \sum_{j=1}^{NRG} R_j^G \, \Delta H_{R,j}(T_G) \qquad \textit{Energy balance}$$

$$-N_i = W_i \sum_{j=1}^{NRS} \nu_{ij}^S R_j^S \qquad \textit{Material interface flux continuity}$$

$$-hS_V(T_G - T_S) = \sum_{j=1}^{NRG} R_j^G \, \Delta H_{R,j}(T_G) \qquad \textit{Thermal interface flux continuity}$$

$$\sum_{j=1}^{NRS} \nu_{ij}^S R_j^S = 0 \qquad \textit{Pseudo Steady State Approximation for adsorbed compounds}$$

$$\sum_{i=1}^{NCA_m} \xi_i \theta_{m,i} = 1 \qquad \textit{Surface stoichiometric equation for the m type site}$$

Boundary conditions are saturated specifying inlet flow, composition and temperature:

$$\dot{m}|_{V=0} = \dot{m}_0 \tag{2.32}$$

$$\omega_i^G\big|_{V=0} = \omega_{i,0}^G \tag{2.33}$$

$$T_G|_{V=0} = T_{G,0} \tag{2.34}$$

N_i is defined as:

$$N_i = K_{m,i}\rho\left[\left(\omega_i^G - \omega_i^S\right) - \alpha_{T,i}\omega_i^G\left(1 - \omega_i^G\right)\ln\left(\frac{T_S}{T_G}\right)\right] \qquad i - th\ diffusive\ flux\ (2.35)$$

It accounts for a material flux, driven by a concentration gradient, and a thermal induced flux, driven by a temperature gradient: direction of this flux depends on the value of the i-th species composition and temperature inside the gaseous bulk and at the deposition surface. The thermal flux component of Eq. (2.35) was derived assuming a linear variation of the temperature inside the boundary layer[42,43,44]. Mass transfer coefficient, $K_{m,i}$, is estimated with the Cess and Shaffer correlation[45] for rectangular ducts:

$$K_{m,i} = \frac{\Gamma_i}{H} * Sh_H \qquad Mass\ transfer\ coefficient\ (2.36)$$

Being Sherwood number Sh_H defined as:

$$Sh_H = \left[\frac{1}{Sh^{\infty}} + 0.25\sum_{n=1}^{\infty}\gamma_n \exp\left(-\frac{8{\beta_n}^2 z}{3H\ Re_H\ Sc}\right)\right]^{-1} \qquad Sherwood\ number\ (2.37)$$

Sh^{∞} is the Sherwood number for a fully developed flow[46], Sc is the Schmidt number and Re_H is Reynolds number referred to the characteristic length H, which is the spacing between the susceptor and the reactor wall; γ_n and β_n are numerical constants while z is the axial coordinate of the reactor.

If the disk of the reactor is rotating, Sherwood and Reynolds number are defined using its diameter as characteristic length:

$$Re_D = \frac{\rho_G w D}{2\mu_G} \qquad \textit{Reynolds number, rotating disk configuration} \quad (2.38)$$

$$Sh_D = 0.39\sqrt{Re_D} \qquad \textit{Sherwood number, rotating disk configuration} \quad (2.39)$$

Nusselt number is defined as a function of Sherwood, Prandtl and Schmidt number:

$$Nu_H = Sh_H \left(\frac{Pr}{Sc}\right)^{1/3} \qquad \textit{Nusselt number} \quad (2.40)$$

All of the correlations employed for the dimensionless numbers assume full mass transport regime.

Eventually, the total number of unknowns to be found is equal to 2NCG+NCA+1 (1 global mass flowrate, 1 gas phase temperature, 1 surface temperature, NCG-1 gas phase mass fractions, NCG-1 surface mass fractions and NCA concentrations of adsorbed species and of surface free sites), saturated by the same number of equations (1 global material balance, 1 energy balance, 1 thermal interface flux continuity equation, NCG-1 gas phase material balances, NCG-1 material interface flux continuity equations, NCA-N_{sites} pseudo steady-state approximations, N_{sites} surface stoichiometric equations). The remaining mass fractions of the carrier gas, inside the gas phase and at the surface, are not unknown as they can be found either with two stoichiometric relations, i.e. the sum of all mass fractions is equal to one, or simply by subtraction of all other mass flowrates from the global mass flowrate.

2.1.2 Physical Parameters

Conductivity and viscosity of the gaseous mixture, assumed to be equal to those of H_2 due to the high dilution of the precursors inside the carrier gas[4], are expressed with the following relations:

$$\lambda_G(T_G) = \lambda_0 + \lambda_1 \frac{T_G}{T_{rif}} + \lambda_2 \left(\frac{T_G}{T_{rif}}\right)^2 \qquad \textit{Gaseous mixture conductivity} \quad (2.41)$$

$$\lambda_0 = 4.6004 * 10^{-2} \left[\frac{J}{m*s*K}\right], \lambda_1 = 2.2763 * 10^{-2} \left[\frac{J}{m*s*K}\right], \lambda_2 = -1.4454 * 10^{-3} \left[\frac{J}{m*s*K}\right].$$

Reference temperature is set equal to $T_{rif} = 298.15\ K$.

$$\mu_G = \mu_{0,G} \left(\frac{T_G}{T_{rif}}\right)^{0.6505} \qquad \textit{Gaseous mixture dynamic viscosity} \quad (2.42)$$

being $\mu_{0,G} = 8.965 * 10^{-6}\ [Pa * s]$.

Binary material diffusivity coefficients of the i-th species inside the hydrogen carrier gas are evaluated exploiting their dependence from temperature and pressure:

$$\Gamma_i(T,P) = \Gamma_{i,0} \frac{1}{P} \left(\frac{T}{T_{rif}}\right)^{\beta_i} \qquad \textit{Diffusivity of the } i-th \textit{ species in the carrier} \quad (2.43)$$

$\Gamma_{i,0}$ and β_i are numerical constants, respectively expressed in $\left[\frac{m^2}{s}\right]$ and dimensionless.

Thermal diffusivity coefficients are obtained with the following polynomial relation:

$$\alpha_{T,i} = \alpha_{0,i} + \alpha_{1,i}\frac{T}{T_{rif}} + \alpha_{2,i}\left(\frac{T}{T_{rif}}\right)^2 \qquad i-th\ species\ thermal\ diff.coeff. \quad (2.44)$$

All α parameters are dimensionless; similarly, the relation employed for specific heats evaluation is a polynomial law:

$$cp_{G,i}(T_G) = A_{cp,i}T_G + B_{cp,i}{T_G}^2 + C_{cp,i}{T_G}^3 + D_{cp,i}{T_G}^4 \qquad i-th\ specific\ heat \quad (2.45)$$

$A_{cp,i}$, $B_{cp,i}$, $C_{cp,i}$, $D_{cp,i}$ are constants expressed in $\left[\frac{J}{mol*K^2}\right]$, $\left[\frac{J}{mol*K^3}\right]$, $\left[\frac{J}{mol*K^4}\right]$, $\left[\frac{J}{mol*K^5}\right]$.

2.1.3 Kinetic Rates Evaluation

Gas phase reaction rates of the heterogeneous model are computed exploiting the thermodynamic consistency relation:

$$R_j^G = \overrightarrow{k_j}\left[\prod_{i=1}^{NCG_{r,j}} P_i^{O_{ij}^G} - exp\left(\frac{\Delta G^{\circ}_{R,j}(T_G, P_{rif})}{R_{gas}T_G}\right)\prod_{i=1}^{NCG_{p,j}} P_i^{\nu_{ij}^G}\right] \quad (2.46)$$

P_i, O_{ij}^G, and ν_{ij}^G are the i-th species partial pressure, j-th gaseous reaction order, and j-th stoichiometric coefficient, while $\overrightarrow{k_j}$ and $\Delta G^{\circ}_{R,j}(T, P_{rif})$ are the j-th reaction forward kinetic constant and the free Gibbs energy variation associated to the j-th reaction in its reference state (ideal mixture of ideal gases at one atmosphere and gas phase temperature T_G); R_{gas} is the universal gas constant.

In the end, $NCG_{r,j}$ and $NCG_{p,j}$ are the number of reactants and the number of products involved into the j-th gaseous reaction among all NCG species.

Eq. (2.46) can be derived considering a system of NC species and NR reactions: the reaction rate of a generic j-th elementary reversible reaction, involving reactants (A, B) and products (C, D) in the form $aA + bB \rightleftarrows cC + dD$, will be a function of temperature, pressure and species concentrations:

$$R_j(T, \boldsymbol{C}) = k_j(T, P) * f_j(\boldsymbol{C}) \qquad j = 1, 2, \dots, NR \qquad (2.47)$$

where $f_j(\boldsymbol{C})$ is a function related to species concentrations, usually defined with a power law. It is possible to express the kinetic constant $k_j(T, P)$ with an Arrhenius formulation:

$$k_j(T, P) = A_j T^{\alpha} P^{\beta} e^{-\frac{E_{act,j}}{R_{gas} T}} \qquad \textit{Kinetic constant} \ (2.48)$$

A is the j-th reaction pre-exponential factor, $E_{act,j}$ is the j-th reaction activation energy, while α and β are two parameters that must be found empirically. If the system consist of a single gaseous phase, the function $f(\boldsymbol{C})$ can be written using species partial pressures instead of concentrations:

$$f_j(\boldsymbol{C}) = \prod_{i=1}^{NC} P_i^{O_{ij}} \qquad i = 1, 2, \dots, NC \qquad \textit{Power law} \ (2.49)$$

Being the reaction reversible, $R_j(T, \boldsymbol{C})$ represents the net contribute between forward reaction rate ($\overrightarrow{R_j}$, pathway from reactants to products) and backward reaction rate ($\overleftarrow{R_j}$, pathway from products to reactants).

Moreover, as the reaction is elementary, for the forward reaction rate reactants partial reaction orders are equal to their stoichiometric coefficients ν_{ij}, while products partial reaction orders are null; the exact opposite is valid for the backward reaction rate.

Therefore, neglecting the dependence of both forward and backward ($\overleftarrow{k_J}$) kinetic constants from pressure, Eq. (2.49) states that:

$$\overrightarrow{R_J} = \overrightarrow{k_J} P_A^a P_B^b \tag{2.50}$$

$$\overleftarrow{R_J} = \overleftarrow{k_J} C_C^c C_D^d \tag{2.51}$$

Then, the net reaction rate will be equal to:

$$R_j(T, \boldsymbol{C}) = \overrightarrow{R_J} - \overleftarrow{R_J} = \overrightarrow{k_J} P_A^a P_B^b - \overleftarrow{k_J} C_C^c C_D^d \tag{2.52}$$

At thermodynamic equilibrium conditions, Eq. (2.52) must be null:

$$R_j^{EQ} = \overrightarrow{R_J^{EQ}} - \overleftarrow{R_J^{EQ}} = \overrightarrow{k_J} P_{A,EQ}^a P_{B,EQ}^b - \overleftarrow{k_J} P_{C,EQ}^c P_{D,EQ}^d = 0 \tag{2.53}$$

$$\overrightarrow{k_J} P_{A,EQ}^a P_{B,EQ}^b = \overleftarrow{k_J} P_{C,EQ}^c P_{D,EQ}^d \tag{2.54}$$

Eq. (2.54) states that forward and backward reaction rate are equal if the system has reached its thermodynamic equilibrium, i.e. if the reactants partial pressures equal the products partial pressures.

Assuming the reference state of ideal mixture of ideal gases at the system temperature and at a reference pressure P_{rif}, rearranging Eq. (2.54) yields to:

$$\frac{\overrightarrow{k_j}}{\overleftarrow{k_j}} = \frac{P_{C,EQ}^{c} P_{D,EQ}^{d}}{P_{A,EQ}^{a} P_{B,EQ}^{b}} = \prod_{i=1}^{NC} a_i^{\nu_{ij}} = K_j^{EQ}(T) \tag{2.55}$$

being $a_i = \frac{P_i}{P_{rif}}$ the i-th species activity and P_{rif} the reference pressure. The ratio between forward and backward reaction rate is equal to the thermodynamic equilibrium constant. The thermodynamic definition of this latter element is:

$$K_j^{EQ}(T) = \exp\left(-\frac{\Delta G_{R,j}^{\circ}(T, P_{rif})}{R_{gas}T}\right) \tag{2.56}$$

Where $\Delta G_{R,j}^{\circ}$ is expressed as:

$$\Delta G_{R,j}^{\circ}(T, P_{rif}) = \sum_{i=1}^{NC} \nu_{ij} \Delta g_{f,i}^{\circ}(T, P_{rif}) \tag{2.57}$$

$\Delta g_{f,i}^{\circ}(T, P_{rif})$ represents the free Gibbs energy variation associated to the i-th species formation: once the reference pressure has been fixed, $\Delta G_{R,j}^{\circ}$ is a function of temperature only and so will be K_j^{EQ}.

A new relation can be found by combining the left hand side of Eq. (2.55) with the right hand side of Eq. (2.56):

$$\frac{\overrightarrow{k_j}}{\overleftarrow{k_j}} = \exp\left(-\frac{\Delta G_{R,j}^{\circ}(T, P_{rif})}{R_{gas}T}\right) \qquad \textit{Thermodynamic consistency} \tag{2.58}$$

Equation (2.58) can be exploited to compute the backward reaction constant from the knowledge of the forward reaction constant and the j-th free Gibbs energy variation.

Consequentially, merging Eq. (2.58) with Eq. (2.52) leads to:

$$R_j(T, \boldsymbol{C}) = \overrightarrow{k_j} P_A^a P_B^b - \overleftarrow{k_j} exp\left(\frac{\Delta G^{\circ}_{R,j}(T, P_{rif})}{R_{gas}T}\right) C_C^c C_D^d \qquad j - th\ reaction\ rate \quad (2.59)$$

This relation can be extended to any elementary (and gaseous) reversible reaction involving an arbitrary number of species, obtaining Eq. (2.46):

$$R_j^G = \overrightarrow{k_j}\left[\prod_{i=1}^{NCG_{r,j}} P_i^{O_{ij}^G} - exp\left(\frac{\Delta G^{\circ}_{R,j}(T_G, P_{rif})}{R_{gas}T_G}\right)\prod_{i=1}^{NCG_{p,j}} P_i^{O_{ij}^G}\right] \qquad j = 1,2, \dots, NRG \quad (2.46)$$

Eventually, surface reactivity includes adsorption, surface recombination and desorption reactions, thus reaction rates can be evaluated with the following formulation[4]:

$$R_j^S = A_j^S \prod_{i=1}^{NCA} \left(C_i^S\right)^{O_{ij}^S} \prod_{m=1}^{N_{SITES}} \prod_{n=1}^{NCA_m} \left(C_{im}^S\right)^{O_{ij}^{S,m}} \qquad j = 1,2, \dots, NRS \qquad (2.60)$$

A_j^S is the pre-exponential factor of the j-th surface reaction, C_i^S is the i-th species surface concentration, O_{ij}^S is the i-th species partial reaction order referred to the j-th surface reaction, C_{im}^S is the surface concentration of the i-th species adsorbed onto the m-type site and $O_{ij}^{S,m}$ is its correspondent partial reaction order in the j-th surface reaction; C_{im}^S is defined as $C_{im}^S = \psi_m \theta_{m,i}$ being ψ_m the surface concentration of m-type sites.

2.2 Kinetic Scheme

The kinetic mechanism adopted in this work, located in Appendix I, consists of 206 reactions subdivided into 139 gas phase reactions and 67 surface reactions with a total of 113 species. Silicon carbide film growth is described by the adsorption and recombination of hydrocarbons, silanes and chlorosilanes intermediates generated inside the gas phase from ethylene and trichlorosilane ($SiHCl_3$), with N_2 as doping precursor.

This scheme does not account for C_{4+} hydrocarbons and coke deposition: HCs containing more than three carbon atoms are unlikely to form because of the high cracking severity (TCVD temperatures are close to 2000 K) while coke formation is thermodynamically inhibited due to the large H_2 molar fraction in the carrier gas, up to 99 mol. %.

Lastly, homogeneous gas phase nucleation and consequent de-hydrocyclization of Si polymeric chains to give droplets or particles is also not featured: due to the inhibiting effect of HCl[37], the inclusion of this phenomenon will probably play a marginal role and the large set of reactions needed for the nucleation mechanism could compromise software performance in terms of computational speed.

2.2.1 Gas Phase Reactivity

The proposed gas phase kinetics involves hydrocarbons, silanes and chlorosilanes pyrolysis. The former is described by the group of reactions G-1÷G-46, where initiation takes place thanks to the homolytic cleavage of ethylene C-H bond in presence of a third body, either a wall or another particle. Subsequentially, a series of propagation and termination reactions, including hydrogen abstractions, α-scissions and eventually radical recombinations, leads to the formation of C_xH_y derivates like methane and acetylene:

$$C_2H_4 + M \leftrightarrows C_2H_3 + H + M \quad \text{(G-33)}$$

$$C_2H_3 + M \leftrightarrows C_2H_2 + H + M \quad \text{(G-28)}$$

$$C_2H_4 + H \leftrightarrows CH_3 + CH_2 \quad \text{(G-15)}$$

$$CH_3 + H \leftrightarrows CH_4 \quad \text{(G-1)}$$

Reactions from G-47 to G-50 represent hydrogen catalytic cycle, in which radical hydrogen is continuously consumed and produced interacting with other species.

Being similar to hydrocarbons pyrolysis, silanes cracking is treated in the set of reactions G-51÷G-71. Gaseous Si presence is enabled by SiCl formation, which is in turn triggered by $SiHCl_3$ decomposition, reaction contained in the chlorosilanes cluster G-72÷ G-125:

$$\mathrm{SiHCl_3} \leftrightarrows \mathrm{SiCl_2} + \mathrm{HCl} \qquad \text{(G-98)}$$

$$\mathrm{SiCl_2} + \mathrm{H} \leftrightarrows \mathrm{SiCl} + \mathrm{HCl} \qquad \text{(G-81)}$$

$$\mathrm{SiCl} + \mathrm{H} \leftrightarrows \mathrm{Si} + \mathrm{HCl} \qquad \text{(G-74)}$$

Reaction G-126 combined with G-52 introduces SiN formation from atomic Si and N_2:

$$\mathrm{Si_2} \leftrightarrows 2\mathrm{Si} \qquad \text{(G-52)}$$

$$\mathrm{N_2} + 2\mathrm{Si} \rightleftarrows 2\mathrm{SiN} \qquad \text{(G-126)}$$

This mechanism has been not yet understood and it is believed to be very fast; moreover, being G-126 trimolecular it is unlikely to occur[39]. Instead, Cavallotti et. al[39] suggested SiN formation from Si_2 and N_2, shown to be a more physically consistent assumption:

$$\mathrm{N_2} + \mathrm{Si_2} \rightleftarrows 2\mathrm{SiN} \qquad \text{(G-126-II)}$$

In any case, both reactions allow to study SiN reactivity in a simplified manner.

Reactions G-127÷G-139 deal with the formation of N doping precursors: although the main precursor is believed to be molecular nitrogen[38], it is worth considering also other species formed in combination with hydrogen (N, NH, NH_2, NH_3). As it will be shown later in this work, NH_3 can lead to excessive nitrogen incorporation over unwanted zones of the reactor, wasting precursors and compromising the overall efficiency of the process.

2.2.2 Surface Reactivity

Surface mechanism hinges on gaseous intermediates adsorption and their consecutive dissociative desorption into stable gaseous species and adsorbed species, namely C^*, Si^*, H^*, N^*, Cl^*, ${CH_x}^*$, ${SiH_x}^*$, ${SiCl_y}^*$ and ${NH_x}^*$; these adsorbed compounds further react forming solid species SiC^{film}, Si_2C^{film}, ${SiC_2}^{film}$, SiN^{film}, which represent the SiC film: Si_2C^{film}, ${SiC_2}^{film}$, SiN^{film} are fictitious species respectively representing a silicon, carbon and nitrogen rich zone of the deposited crystalline lattice. Moreover, the adopted kinetic model features two types of sites: σ_C stands for a carbon site, whilst σ_{Si} is a silicon site.

Methane, ethylene, acetylene and C_xH_y reactivity is included in the cluster A-1÷A-8:

$$CH_4 + \sigma_{Si} \rightarrow C^* + 2H_2 \qquad \text{(A-1)}$$

$$C_2H_4 + 2\sigma_{Si} \rightarrow 2C^* + 2H_2 \qquad \text{(A-6)}$$

$$C_2H_3 + 2\sigma_{Si} \rightarrow C^* + CH^* + H_2 \qquad \text{(A-7)}$$

$$C_2H_2 + 2\sigma_{Si} \rightarrow 2C^* + H_2 \qquad \text{(A-8)}$$

Similarly, set A-9÷A-16 deals with silanes adsorption and recombination to give Si^*:

$$SiH_2 + \sigma_C \rightarrow {SiH_2}^* \qquad \text{(A-9)}$$

$${SiH_2}^* \rightarrow Si^* + H_2 \qquad \text{(A-10)}$$

Among group A-15÷A-56, $SiCl^*$ plays an important role in the formation of surface Si and Cl; the former reacts together with adsorbed carbon growing the silicon carbide film:

$$Si^* + C^* \rightarrow SiC^{film} + \sigma_C + \sigma_{Si} \qquad \text{(A-44)}$$

$$2Si^* + C^* \rightarrow Si_2C^{film} + 2\sigma_C + \sigma_{Si} \qquad \text{(A-45)}$$

$$Si^* + 2C^* \rightarrow {SiC_2}^{film} + \sigma_C + 2\sigma_{Si} \qquad \text{(A-46)}$$

Nitrogen incorporation is described by reactions A-57÷A-67: molecular nitrogen and its derivates get adsorbed on a silicon site where they recombine with Si^* to form SiN^{film}.

$$N_2 + 2\sigma_{Si} \rightarrow 2N^* \quad \text{(A-57)}$$

$$N + \sigma_{Si} \rightarrow N^* \quad \text{(A-58)}$$

$$N^* + Si^* \rightarrow SiN^{film} + 2\sigma_{Si} \quad \text{(A-62)}$$

$$N^* + SiH_2{}^* \rightarrow SiN^{film} + H_2 + 2\sigma_{Si} \quad \text{(A-64)}$$

In the end, it is worth noting that this mechanism theorizes molecular nitrogen adsorption to occur exclusively onto silicon sites, thus N_2 is in direct competition with hydrocarbons.

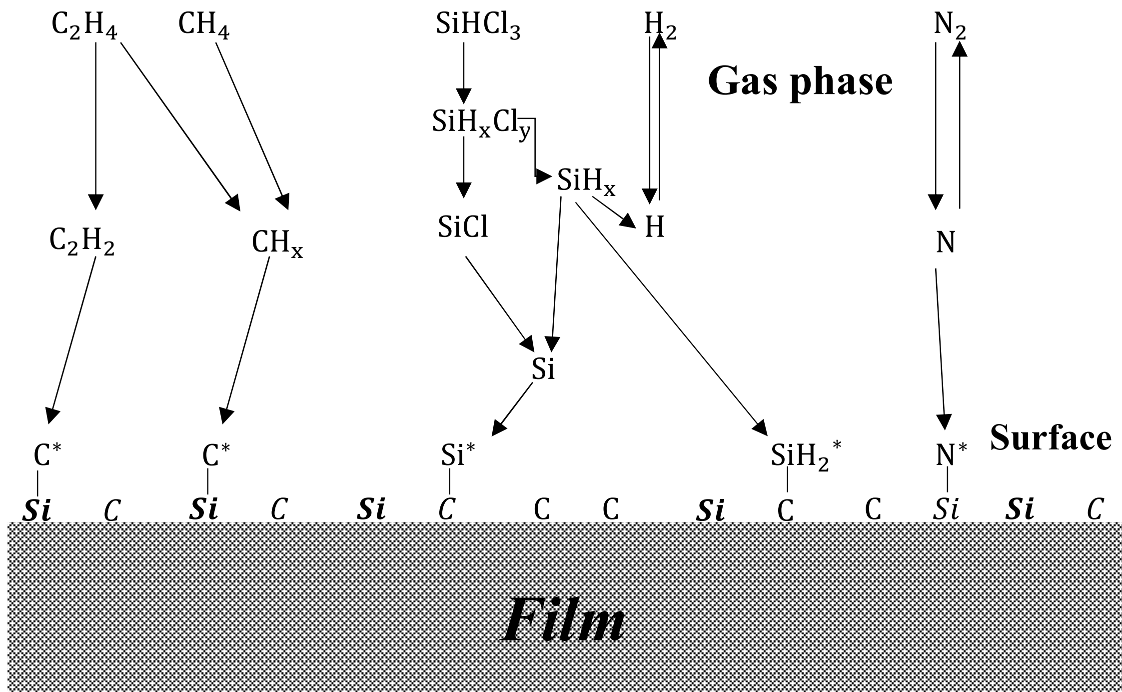

Figure 2.2: *schematic representation of the $C_2H_4/SiHCl_3/N_2$ kinetic scheme; this oversimplified figure resumes most of the key species and main pathways for the adsorption of SiC intermediates and dopants.*

2.2.3 Thermodynamic Analysis

Once the kinetic scheme has been introduced, it is useful to identify the most active species contributing to deposition and doping of the silicon carbide film. Due to the high temperatures involved in thermal chemical vapour deposition processes, it is possible to assume that all of the reactions describing gas phase reactivity approach their thermodynamic equilibrium[37,39]: therefore, a thermodynamic analysis built on acknowledged sources gathered from literature represents a useful tool to identify the key gaseous species in the system and obtain more knowledge about chlorosilanes chemistry.

An interesting study about chlorosilanes thermodynamics is the one conducted by Veneroni and Masi[37] on an older version of the kinetic scheme previously presented, applied to simulate a reactor working with SiH_4, C_3H_8, HCl precursors (0.8 C/Si ratio, 1 Cl/Si ratio) diluted in a H_2 carrier, which discovered that at lower temperatures the most abundant species among chlorosilanes are found to be silane and dichlorosilane followed by SiH_xCl_{4-x} species in the order SiH_3Cl, SiH_2Cl_2, $SiHCl_3$ and eventually Si; this trend reverses when moving towards the thermal range of chemical vapour deposition processes (from 1873 K upwards), where HCl and atomic Si have the highest molar fractions and the stability order of chlorosilanes shifts to $SiHCl_3 > SiH_2Cl_2 > SiH_3Cl$.

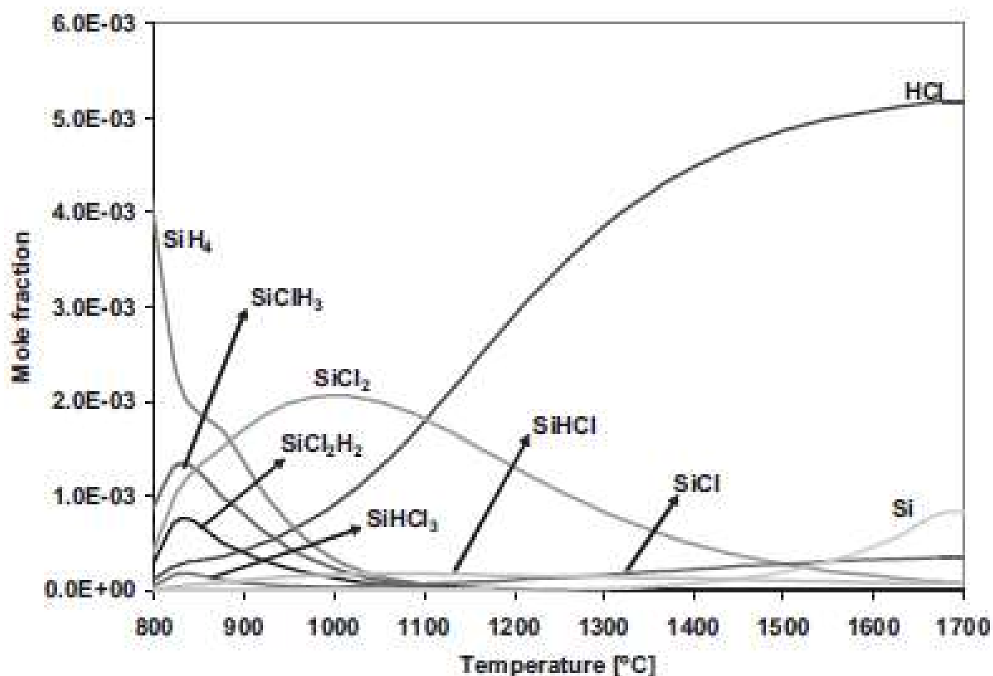

Figure 2.3: *distribution of main silicon chlorinated species diluted in a H_2 carrier gas as a function of temperature[37]; values at thermodynamic equilibrium.*

Veneroni and Masi also observed that gas phase composition at thermodynamic equilibrium was insensitive to variations of C/Si and Cl/Si ratios, as the same distribution of Figure 2.3 was obtained even when altering feed molar fractions of the precursors.

Regarding thermodynamic stability of hydrocarbons, a similar study performed by Fiorucci[48] on a $SiHCl_3/C_2H_4/H_2$ system (1.75 C/Si, 0.04 Si/H_2) identified C_2H_2, CH_4 and CH_3 as the most abundant species among all HCs formed inside the gas phase.

N_2 gas phase reactivity is still yet to be understood in detail, thus a thermodynamic analysis on molecular nitrogen and its derivates is more difficult to perform as the current kinetic scheme is only able to theorize the presence of certain intermediates without experimental evidences: what emerges from the work of Cavallotti et. al.[39] is that nitrogen incorporation mechanism might be triggered by formation of the SiN radical in the gas. Indeed, this research group performed numerical simulations of a horizontal CVD reactor relying on a kinetic mechanism derived from the one implemented by Veneroni and Masi and pointed out that SiN gas phase molar fraction along the reactor axis is significantly larger than those of all other species originated from the interaction between N_2 and H_2.

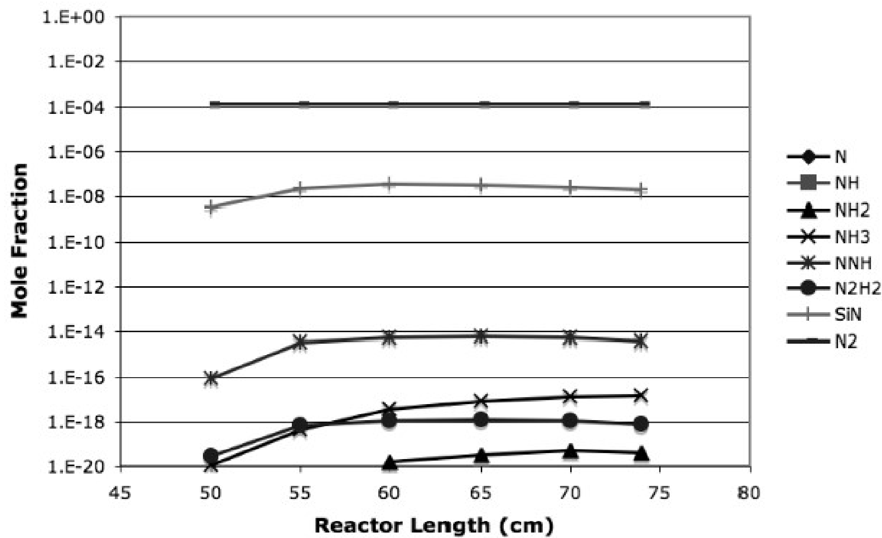

Figure 2.4: *gas phase composition along the axis of a 150 mm wafer of a horizontal CVD reactor*[39] *working at 1823 K with a feed of 100 slm H_2, 30 sccm $SiHCl_3$, 22.5 sccm C_2H_4 and 13 sccm N_2.*

In the end, from this analysis it is reasonable to assume that C_2H_2, CH_4, CH_3, Si, $SiHCl_3$, and HCl provide an important contribute to gas phase reactivity and consequently to SiC deposition while N_2 and SiN are believed to be the main dopant molecules.

2.3 Reactor Layout

PE-106 epitaxy reactor developed by LPE S.p.A. is a horizontal hot wall CVD reactor suitable for the production of 150 mm 4H-SiC (0001) nitrogen doped wafers; the digital twin of the reactor employed in this work is depicted in Figure 2.5: gaseous carrier and precursors are injected in a quartz liner using hundreds of nozzles to ensure optimal flow distribution and then, after being pre-heated in a short rectangular channel called "transition piece", they reach the deposition chamber, consisting of a rotating disk graphite susceptor installed between two graphite foils, a front plate and an outlet element. These latter foils must preserve flow direction respectively towards and away from the susceptor in order to avoid formation of vortices and recirculation zones which could trap the precursors leading to SiC deposition in unwanted zones of the chamber.

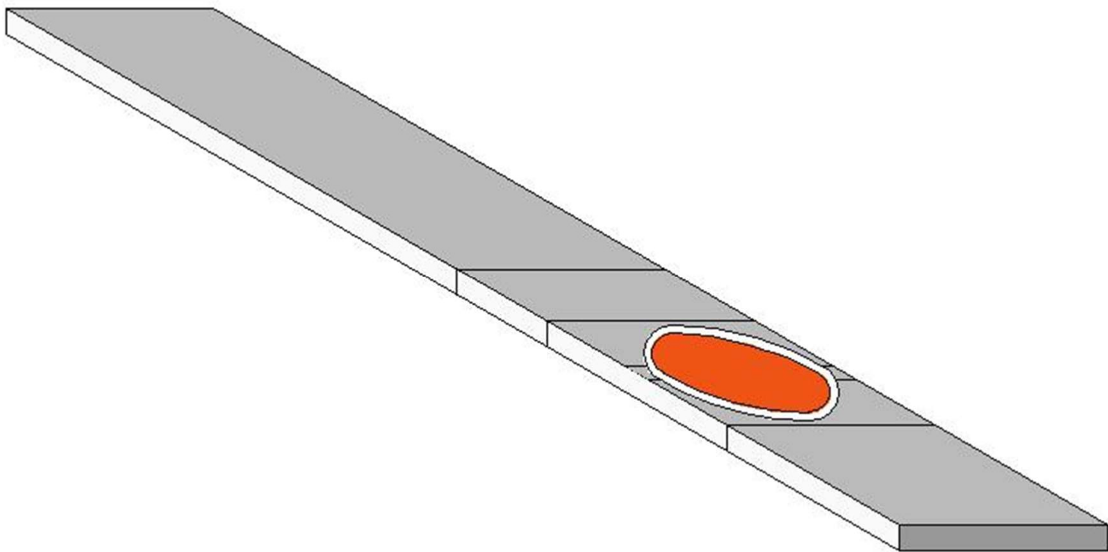

Figure 2.5: *digital twin of PE-106 reactor; from left to right: liner, transition piece, front plate, rotating disk susceptor (highlighted in orange: wafers, also known as growth plates, are placed onto this element), outlet.*

The whole reactor is covered by a metallic lid surrounded by a quartz bell externally heated by a radio-frequency coil. Heat is provided by radiation from the bell to the external walls of the reactor, by conduction from the walls to the susceptor and then onto the growth plate. During a typical run, the carrier gas is heated by convection from the walls, while cooling water controls the temperature of the process: gas enters in the liner zone at room temperature and gets gradually preheated up to 1300 K inside the transition piece, it reaches 1800 K close to the susceptor (orange region of Figure 2.6) and finally leaves the system at 1980 K.

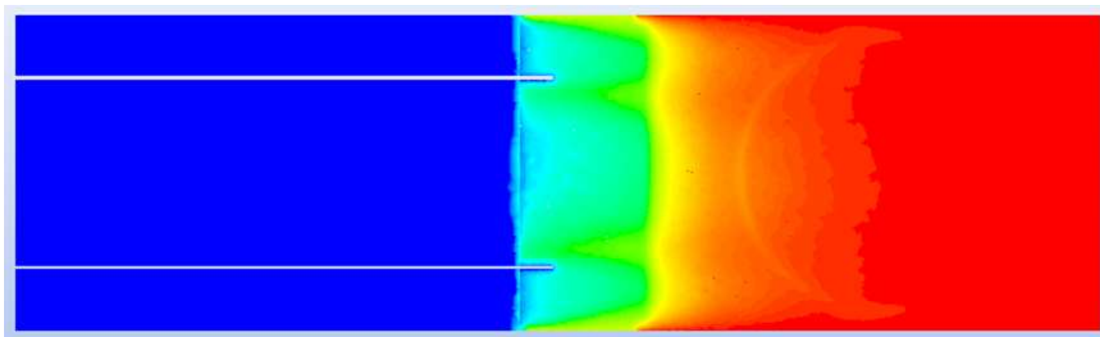

Figure 2.6: *simulated gas temperature profile for each zone of the reactor; pre-heating is assumed to occur only in the transition piece zone to save on computational costs.*

Loading and unloading of the growth plates between each batch-run, which takes approximately 10-12 minutes, is achieved with a robotic arm inserted in an apposite load-lock chamber placed prior to the deposition chamber: it is mandatory to reduce the dust content of the air surrounding these chambers with filters and ventilation systems as dust deposition onto the wafer compromises the SiC film purity and thus its properties.

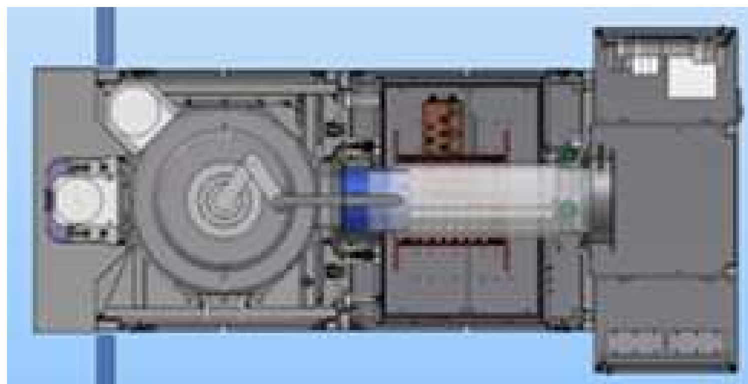

Figure 2.7: *transverse section of the PE-106 reactor with load-lock (left) and deposition chamber (right).*

2.4 Software Structure

The software employed in this work, a Fortran code written for GNU interfaces, is able to solve a dimensionless version of the mono-dimensional heterogeneous model introduced in Subsection 2.1.1; PE-106 reactor is approximated as a single line divided in 800 segments in order to implement the first order finite difference method.

The user is asked to provide eight input data files, respectively containing:

1. geometrical parameters and operating conditions of the reactor with wall thermal conductivity, susceptor emissivity and external liminar heat transport coefficient;
2. kinetic scheme together with all the parameters required for the estimation of kinetic constants in their Arrhenius form $k(T) = AT^{\alpha} exp\left(E_{act}/R_{gas}T\right)$;
3. stoichiometric matrices for both gas and surface reactions;
4. reaction order coefficients for all reactions except elementary ones;
5. thermodynamic and chemical-physical properties for each compound (molecular weight, standard enthalpy, standard entropy, heat capacity);
6. thermal and material transport properties for each compound evaluated at standard temperature and pressure (298 K, 10^5 Pa);
7. initialization parameters, such as relative and absolute tolerance, maximum iterations number, relaxation parameters and Jacobian matrix, either analytic or numeric;
8. initial guess values, it is not mandatory to specify all first attempt values as if their number is lower than the number of equations then the software is able to generate the lacking parameters in order to saturate the degrees of freedom of the system.

Once the user has provided a correct set of input data, the software proceeds with results calculation through a series of subroutines. If convergence is reached, four post-processing text files are generated, containing the trend of flowrates, dimensionless numbers, material fluxes, gas and surface temperature, molar composition, SiC growth rate and doping along the reactor axis. In case of failure, the software immediately stops.

2.4.1. Software Modifications

The reactivity of a TCVD system is very sensitive to temperature: due to the exponential term of Arrhenius equation, even a variation of 10-20 kelvins has a significant impact on the kinetics of the process. Hence, a satisfying agreement between empiric model and experimental data can be achieved only by estimating a reasonable temperature profile for the wafer placed onto the susceptor; one way to do this is to impose the energy input provided to the system, i.e. fix the heat flux flowing from the radio-frequency coil to the susceptor and other reactor walls, accounting for all the thermal resistances between these elements, and then compute the temperature along the axis of the wafer. Another solution is to directly infer the wafer temperature profile using values derived from previous experimental measurements without modelling the heat transfer: the software employed in this work adopts the latter method.

Wafer thermal profile in the source code was originally calculated through linear interpolation by imposing the temperature in five different points at $z/L = 0,\ 1/3,\ 1/2\,,\ 2/3\,,\ 1$, where z/L is the dimensionless length of the wafer, z is the wafer axial coordinate and L is the wafer diameter, equal to 150 mm. For instance, given the temperature of two points at the start of the wafer ($\mathrm{z}_0 = 0$ mm) and at one third of its length ($\mathrm{z}_{1/3} = 50$ mm), namely $P_0(z_0,\ T_0)$ and $P_{1/3}(z_{1/3}\,,\ T_{1/3})$, the temperature T_z of any generic point $P_z(z,\ T_z)$ in the interval $0 \div 150$ mm is found with Eq. (2.61):

$$\frac{T_z - T_0}{z - z_0} = \frac{T_{1/3} - T_0}{z_{1/3} - z_0} \tag{2.61}$$

This equation states that if P_0, P_z and $P_{1/3}$ lie on the same straight line on the (z, T) plane, then the slope computed from P_z to P_0 must be equal to the slope computed from $P_{1/3}$ to P_0. Thus, this relation can be rearranged obtaining the unknown temperature as:

$$T_z = T_0 + \left(T_{1/3} - T_0\right) * \frac{z - z_0}{z_{1/3} - z_0} \tag{2.62}$$

Wafer temperature profile is obtained once this procedure has been repeated for each point in the interval and for each interval in which the wafer is subdivided.

One of the main fixes done on the software was the implementation of a thicker grid in an attempt to reduce the interpolation error: the axis of the wafer was partitioned into ten segments and the temperature was fixed in eleven points at $z/L = 0,\ 1/10,\ 2/10, \dots,\ 1$. Working with an augmented discretization also eased the reproducibility of smooth temperature profiles, like the gaussian shape reported in Figure 2.8, in order to achieve a gradual transition of the temperature over the axis.

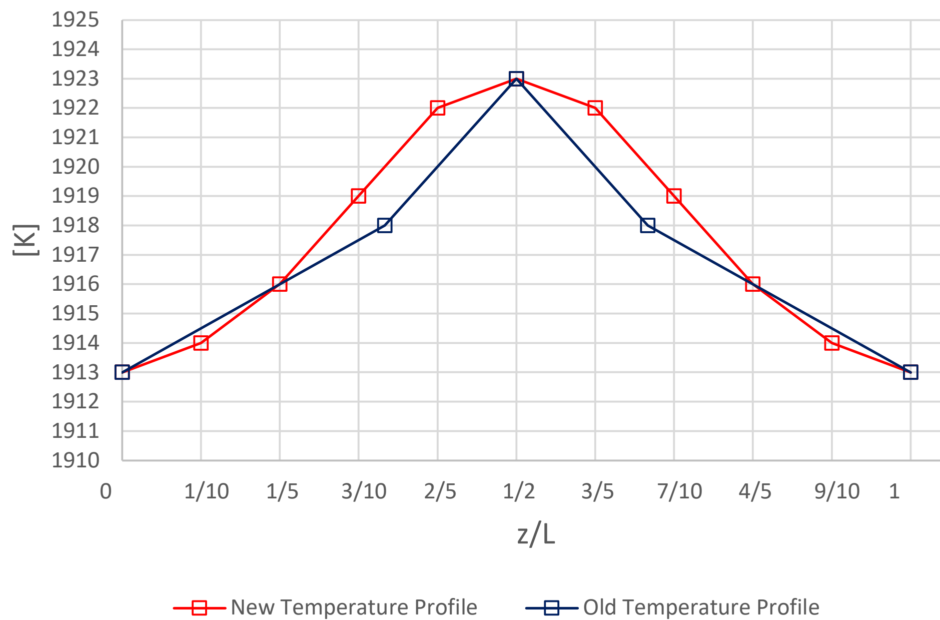

Figure 2.8: *comparison between the pre-existing (blue) and the modified wafer temperature profile (red); the modified profile is characterized by a smoother zone close to the centre of the wafer axis.*

Although most of the simulations were carried with a completely flat temperature profile with a constant temperature of 1923 K for the whole length of the wafer, the profile depicted in Figure 2.8 was particularly useful to test the behaviour of growth rate and doping incorporation in presence of different heating zones on the susceptor, which of course leads to a non-flat wafer temperature profile; in some instances, an asymmetric distribution was also tested.

Other modifications applied to the software were related to the geometry of the system: the length of the transition piece was changed from to 50 mm to 100 mm as the previous value was too short compared to the actual length of that section in the real reactor; moreover, the temperature of this element was also changed accordingly to the effective operative conditions, ranging from a value of 1377 K at the inlet up to 1923 K at the outlet. This fixes allowed to account for a more gradual pre-heating of the gaseous phase with the possibility to simulate silicon carbide deposition not only onto the wafer but also, even if more mildly, in the last centimetres of the transition piece and over the front plate, a phenomenon which is believed to occur also in the real reactor: this task was achieved by the introduction of a damping factor applied to the growth rate calculated in those specific zones, varying from zero to one and set equal to 0.3.

Lastly, concerning kinetic aspects of the software, the logarithmic value of the exponential factor of acetylene dissociative adsorption was changed from its previous reference value of 18.5 and set equal to a new value of 19.

2.5 Experimental Data Review of Film Thickness and Doping Profiles

Figure 2.9 displays the film thickness profile of a 150 mm nitrogen doped SiC wafer produced in a 10 minutes test run by PE-106 reactor working with 100 slm feed (1.3 C/Si ratio, molar composition: 0.997922 H_2, 0.001138 $SiHCl_3$, 0.00074 C_2H_4, 0.00020 N_2) with a wafer flat temperature profile of 1923 K and a rotating susceptor:

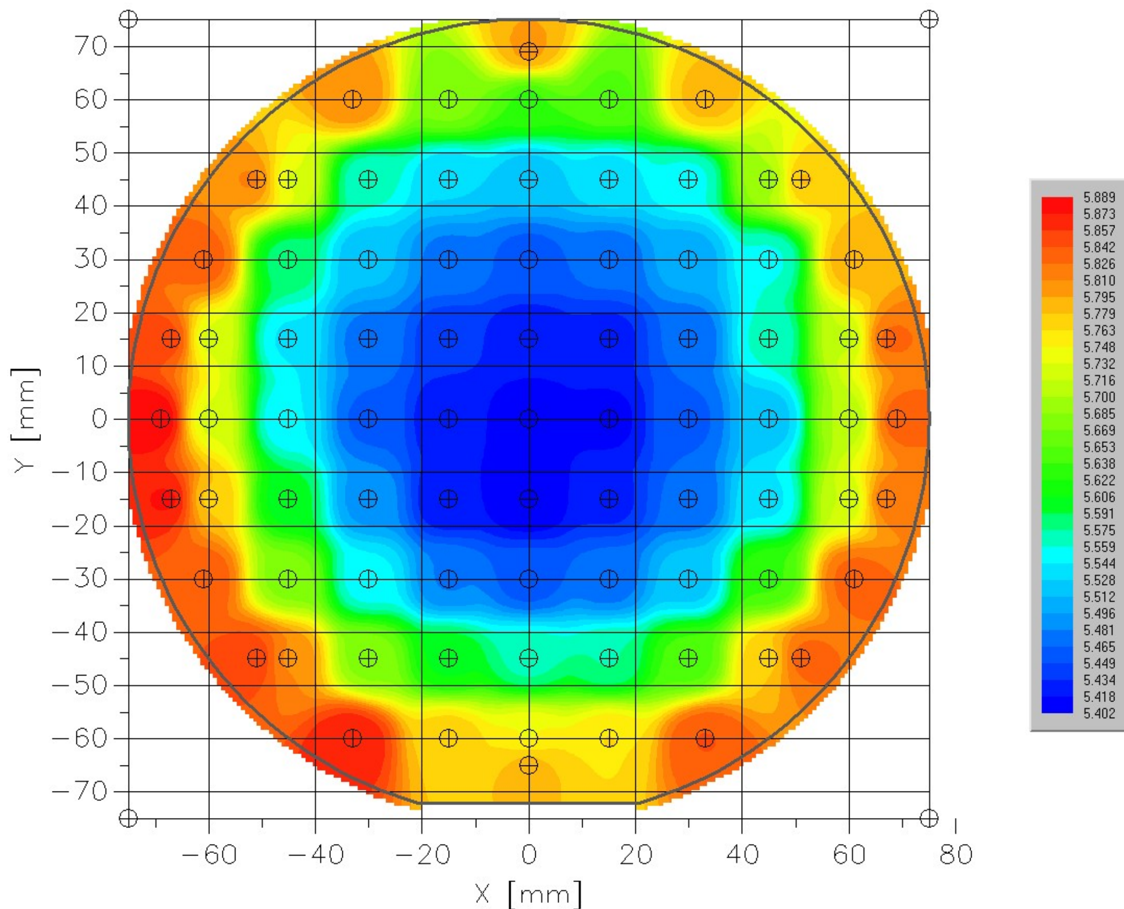

Figure 2.9: *film thickness colormap for the rotating susceptor configuration, data in µm.*

The deposited SiC film is characterized by low radial uniformity as its thickness ranges from 5.73 µm to 5.89 µm at the wafer outer edges and it is equal to 5.43 µm at the centre. As a result, this lack of isotropy compromises film quality and it needs to be compensated with a polishing treatment to obtain a completely flat wafer, which can be a challenging task when considering the extreme hardness and chemical inertia of SiC.

Nitrogen incorporation profile evaluated in the same run (Figure 2.10) is also rather non-homogeneous, displaying a low doping annulus close to the wafer edges (blue-cyan region) and a rich doping zone at the centre (red region). Indeed, doping radial profile resembles a sort of W-shape with a central maximum and two peripheral minima: taking the vertical axis $X = 0$ mm as a reference, N concentration inside the film moves from an initial value of 1.86E+16 at/cm^3 to 1.78E+16 at/cm^3 at the start of the wafer, then it gradually increases up to 1.98E+16 at/cm^3 at the centre before dropping back to 1.77E+16 at/cm^3 at $Y = 60$ mm and eventually rising up to 1.85E+16 at/cm^3.

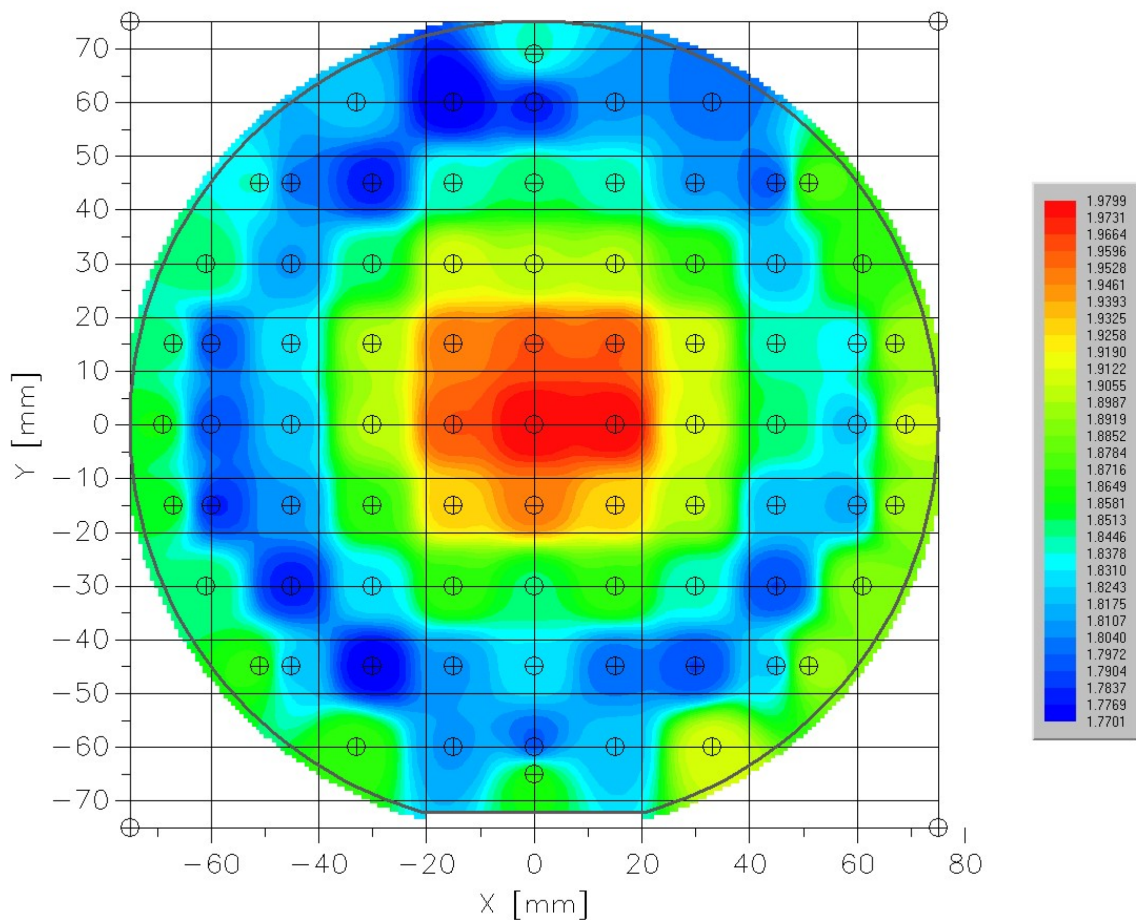

Figure 2.10: *N incorporation colormap for the rotating susceptor configuration, data in* 10^{16} *at/cm*^{3}.

A possible way to justify this behaviour from a physical point of view could be the inverse proportionality between growth rate and nitrogen incorporation: nitrogen atoms are more "diluted" inside high thickness regions of the silicon carbide bulk, characterized by higher growth rates, and on the contrary they are more concentrated in low thickness zones.

Other anomalies emerges when repeating the same test run with a still susceptor instead of a rotating one. In this scenario, reported in Figure 2.11, film thickness decreases on the central vertical axis from 8.53 μm to 3.27 μm due to the inverse proportionality between boundary layer width and precursors diffusive flux mentioned in Subsection 1.1.4. While film disuniformity on the vertical axes is not an issue as it is solved in the rotating susceptor configuration, where the motion of the disk periodically alters the highest deposition zone, there are still some unwanted thickness fluctuations along the horizontal axes except from the strip between $Y = -5$ mm and $Y = 5$ mm, characterized by an almost homogeneous thickness of 5.64 μm.

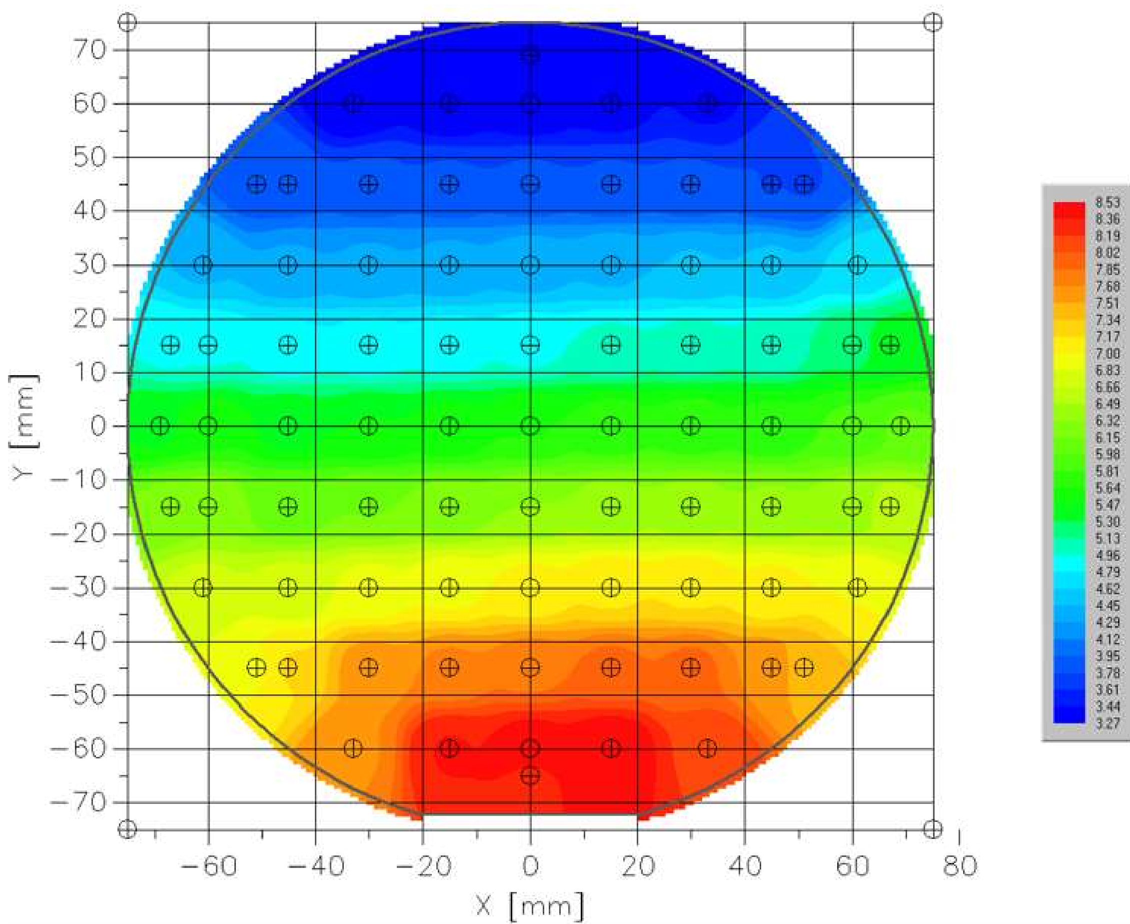

Figure 2.11: *film thickness colormap for the still susceptor configuration, data in μm.*

Same considerations are valid for nitrogen incorporation profile in the still susceptor configuration (Figure 2.12), where N concentration rises over the vertical axes with a bull trend (once again due to the inverse proportionality between film thickness and doping):

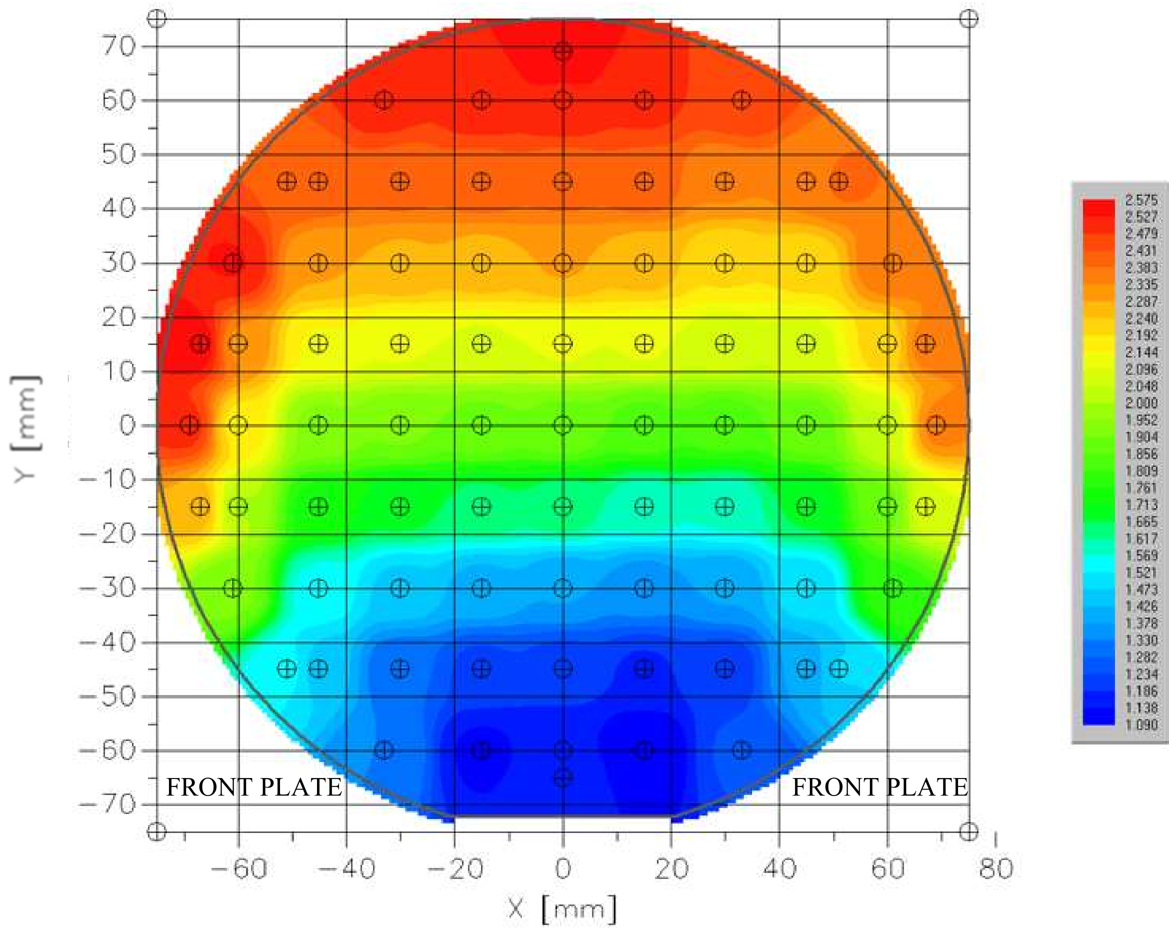

Figure 2.12: *N incorporation colormap for the still susceptor configuration, data in 10^{16} at/cm^3.*

In this instance, there is a large non-uniformity in the first section of the wafer, with doping values close to 1.09E+16 at/cm^3 at $X = \pm 40$ mm and equal to 1.4E+16 at/cm^3 at the extremities ($X = \pm 40$ mm, $Y = -45$ mm); this variation could be explained by the geometry of the system combined with the activation of certain reactions affecting nitrogen incorporation or altering C/Si ratio: local residence time is slightly higher at the edges of the front plate since the distance between the latter and the wafer grows when moving away from the central axis, so at the extremities the feed may start reacting before reaching the wafer. If this phenomenon occurs, then reduction of wafer diameter should play a beneficial role as it effectively shortens the front plate-wafer edges distance.

CHAPTER 3

Numerical Simulations of SiC Deposition and Nitrogen Incorporation

This chapter reports the results of several simulations performed to match the experimental data, gathered from the two test-runs conducted with PE-106 epitaxy reactor presented in Chapter 2, and further investigates the phenomenon of enhanced nitrogen incorporation at the edges of the SiC wafer in the still susceptor configuration. Results are presented following the chronological order in which the simulations were computed:

Section 3.1 introduces the Key Performance Indicators useful to analyse the results of the simulations and the operative conditions employed for the numerical simulations.

Then, Section 3.2 examines the outcome of a sensitivity analysis performed on the $C_2H_4/SiHCl_3$ kinetic scheme, presented in the previous chapter, without software fixes.

Consequently, Section 3.3 compares the results achieved by the 1D numerical simulations with the experimental trends of averaged growth-rate and doping.

Eventually, Section 3.4 includes the outcome of 1D and 3D simulations computed to study enhanced nitrogen doping at wafer edges.

3.1 Introductory Aspects and Key Performance Indicators

Before discussing the results, it is useful to identify the main parameters of interest to assess the quality of the numerical simulations, as the post-processing section of ASM.for provides a large number of outputs (gas and surface temperature, composition, diffusive and reactive fluxes, film thickness, nitrogen incorporation, growth rate, etc…). Among this information, one of the most important is surely the silicon carbide film growth rate:

$$G.R. = \frac{W_{SiC}}{\rho_{SiC}} \sum_{i=1}^{NC_{film}} \sum_{j=1}^{NRS} \nu_{ij}^{S} R_{j}^{S} \qquad NC_{film} = 1, 2, 3, 4 \qquad \textit{Growth Rate}\ (2.7)$$

In this work, NC_{film} ranges from one to the total number of film species (four: SiC^{film}, Si_2C^{film}, SiC_2^{film}, SiN^{film}) formed by surface recombination of adsorbed species; as most of the film consists of silicon carbide, it is reasonable to assume film molecular weight and density equal to the ones of SiC. Since the typical run time of PE-106 reactor is in the order of minutes, it is convenient to express $G.R.$ in micron over minutes as it allows to quickly evaluate film thickness at the end of the batch-run by simply multiplying the growth rate per the correspondent run-time, t_{run}:

$$Film\ Thickness = G.R. \ * \ t_{run} \qquad (3.1)$$

In the still susceptor configuration the growth rate, and consequently film thickness, decays along the wafer axial coordinate z (similarly to Figure 1.5): in this work, the maximum growth rate value over this profile is named "peak growth rate".

$$G.R._{peak} = \max[G.R.(z)] \qquad \textit{Peak Growth Rate}\ (3.2)$$

Another Key Performance Indicator is nitrogen incorporation, which can be defined as SiN^{film} molar fraction within the SiC film. Thus, modifying Eq. (2.8) to account for SiC as limiting growth precursor and gaseous SiN as dopant species leads to:

$$x_{SiN^{film}} = V_{SiC} * \frac{n_{SiN}}{G.R.} \qquad \text{Dopant molar fraction within the SiC film} \quad (3.3)$$

$x_{SiN^{film}}$ is equivalent to nitrogen molar fraction inside the film, V_{SiC} is SiC molar volume and n_{SiN} is SiN molar flux. Another way to estimate N incorporation is:

$$[N]_{film} = \frac{\text{number of N atoms within the SiC film}}{V_{SiC}} \quad (3.4)$$

Where film molar volume is assumed to be equal to the one of V_{SiC}; from now on, this latter relation will be employed to define N incorporation.

The last KPIs refer to the rotating susceptor configuration, where the rotation evens out growth rate and nitrogen doping along the axis of the wafer:

$$G.R._{avg}(z) = \frac{\int_0^z G.R.(\mathcal{Z})d\mathcal{Z}}{L_{wafer}} \qquad \text{Averaged Growth Rate} \quad (3.5)$$

$$[N]_{film,avg}(z) = \frac{\int_0^z [N]_{film}(\mathcal{Z})d\mathcal{Z}}{L_{wafer}} \qquad \text{Averaged Nitrogen Incorporation} \quad (3.6)$$

Being L_{wafer} the diameter of the wafer. Disuniformity in film thickness and nitrogen incorporation are computed from the maximum and minimum values of Eq. (3.5) and Eq. (3.6) as:

$$s_{film} = \frac{G.R._{avg,max} - G.R._{avg,min}}{G.R._{avg,max} + G.R._{avg,min}} * 100 \qquad \text{Film disuniformity} \quad (3.7)$$

$$s_{doping} = \frac{[N]_{film_{avg,max}} - [N]_{film_{avg,min}}}{[N]_{film_{avg,max}} + [N]_{film_{avg,min}}} * 100 \qquad \text{Doping disuniformity} \quad (3.8)$$

3.1.1 Wafer Horizontal Subdivision

As already stated, ASM.for solves the conservation equations of the monodimensional model referred to the centerline of the reactor, which is also the wafer centerline. On the other hand, the experimental data are spread across the whole surface of the wafer like in Figure 3.1 (each crossed circle represents a measurement point): as shown in Section 2.5, the parameters of study display significant variations not only along the central axis of the wafer but also when moving from the centerline to other horizontal sectors, thus it is interesting to investigate also this latter zones.

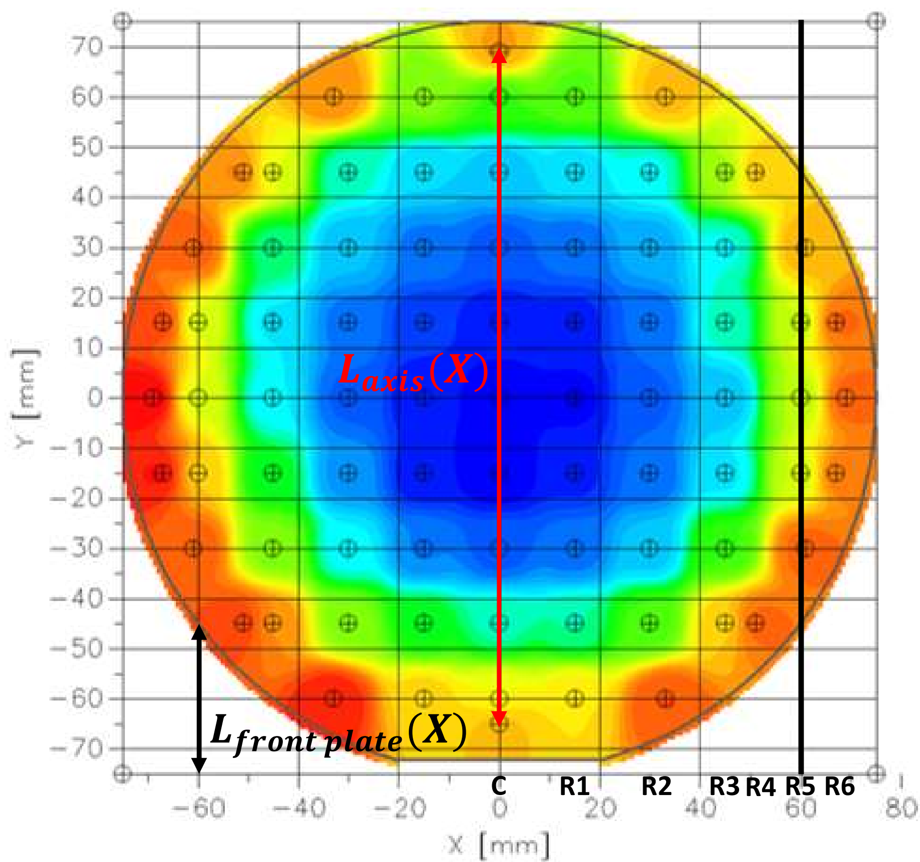

Figure 3.1: *schematic representation of the wafer subdivision in horizontal sectors.* $L_{front\ plate}$ *is the distance between the wafer and the leading edge of the front plate, varying along the abscissa.*

Simulations carried with the monodimensional model are obviously not able to account for more than one abscissa at the same time, i.e. it is not possible to calculate growth rate and nitrogen incorporation profiles in a bidimensional manner by simultaneously simulating both the centerline and all other horizontally displaced sectors of the wafer.

However, it is still possible to run a single simulation for each abscissa of the wafer while tuning the length of the front plate zone to match the target horizontal coordinate: for instance if the target abscissa is the centerline (X $= 0$ mm), then a simulation referred to this abscissa will have a front plate length $L_{front\,plate}$ of 5 mm, while if the target horizontal coordinate is R5 (X $= 60$ mm, black line of Figure 3.1), then the front plate length will be set equal to roughly 30 mm. This strategy can be repeated for all other horizontal coordinates of the wafer, eventually obtaining a 2D trend of growth rate and N doping over the whole wafer by merging a set of 1D horizontally displaced simulations. Furthermore, each horizontally displaced simulation has its own set of measurement points and its own axial length associated to its horizontal coordinate, $L_{axis}(X)$, which is the distance between its first and its last measurement point; for the sake of clarity, the centerline has eleven measurement points, the first one located at $Y_1 = -65$ mm and the last one at $Y_2 = 69$ mm: the sampled axial length is equal to the distance between these points, $L_{axis}(X = 0 \text{ mm}) = Y_2 - Y_1 = 134$ mm. Each simulation performed over a certain abscissa will compute the profile of a generic variable along the whole length of the wafer, but the values of interest are only the ones evaluated at the same Y coordinates of the measurement points (comparison between numerical results and experimental data is done exclusively over these points). Even if most of the simulations included in this work are evaluated with respect to the central axis of the wafer, this approach was particularly useful to study the anomalies of nitrogen incorporation in the still susceptor configuration: in this particular case, the right portion of the wafer was subdivided into five lines with abscissas C, R2, R3, R5, R6, reported in Figure 3.1 and also in Table 3.1.

Abscissa	L_{axis} $[mm]$	$L_{front\,plate}$ $[mm]$	X $[mm]$	**Measurement points**
Centerline (C)	134	negligible	0	11
R2	120	7	30	9
R3	90	15	45	7
R5	60	30	60	5
R6	31	41	65	3

Table 3.1: *geometrical features of each horizontal set of experimental data; abscissas R1 and R4 of Figure 3.1 were not studied because the former is too close to the centerline and there is a negligible variation of the experimental data between these lines, while the latter features only two measurement points and it is also too close to R3 (no significant variation of the experimental data).*

3.1.2 Operative Conditions: Monodimensional Model

ASM.for simulates an industrial reactor, therefore several data are confidential information and cannot be widespread: this subsection will provide only some key features of the reactor geometry and operative conditions adopted to carry the numerical simulations in order to make possible reproducing the results achieved in this work.

The simulated portions of the reactor consist of a liner, a transition piece, a front plate, the wafer, and an outlet element. The heated susceptor, not tilted with respect to the horizontal, can be either still or rotating.

The reactor works under moderate vacuum at 10^4 Pa; wall temperature ranges from 573 K to 1377 K in the liner zone, then from 1377 K to 1923 K inside the transition piece, while it is set equal to 1923 K over the wafer and it eventually decays to 1377 K at the outlet. As already mentioned in Subsection 2.4.1, the most employed temperatures profiles for the growth plate were three, namely a flat one, with a constant temperature of 1923 K for the whole length of the wafer, and two gaussian-like profiles, shifted by a few kelvins, both slightly asymmetric and characterized by a gradual increase up to a central maximum equal to 1923 K followed by a monotonic decay to 1905-1910 K.

The reactor feed flowrate consists in 100 slm (standard litres per minute) of a mixture of hydrogen, trichlorosilane, ethylene, and nitrogen at room temperature: mixture molar composition is reported in Table 6, C/Si ratio is equal to 1.3 while the $\mathrm{Si/H_2}$ ratio is 0.00114.

Species	Molar Fraction [-]
H_2	0.997922
$SiHCl_3$	0.001138
C_2H_4	0.00074
N_2	0.00020

Table 3.2: *feed mixture molar composition.*

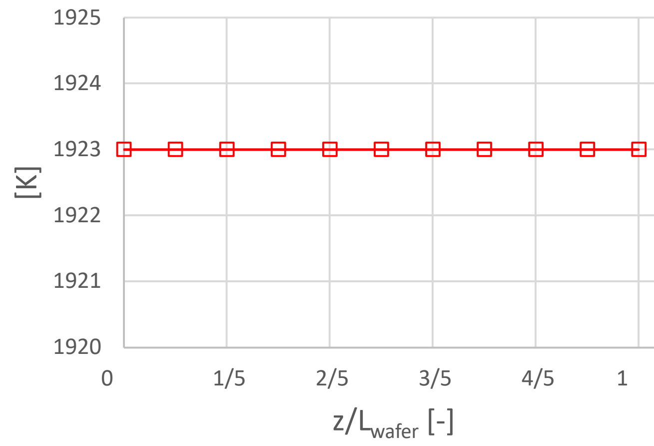

Figure 3.2: *wafer flat temperature profile.*

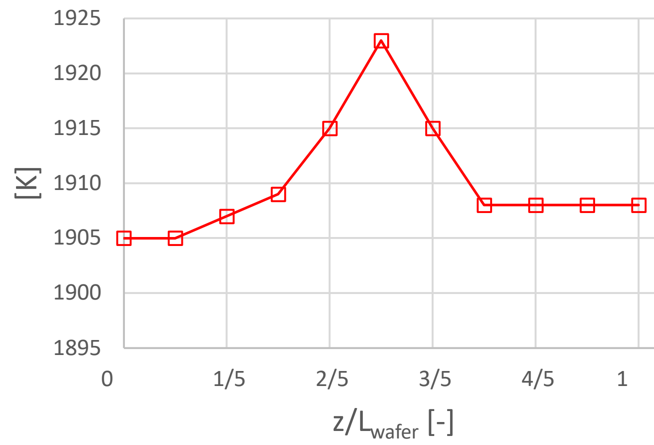

Figure 3.3: *wafer "gaussian" temperature profile, G1.*

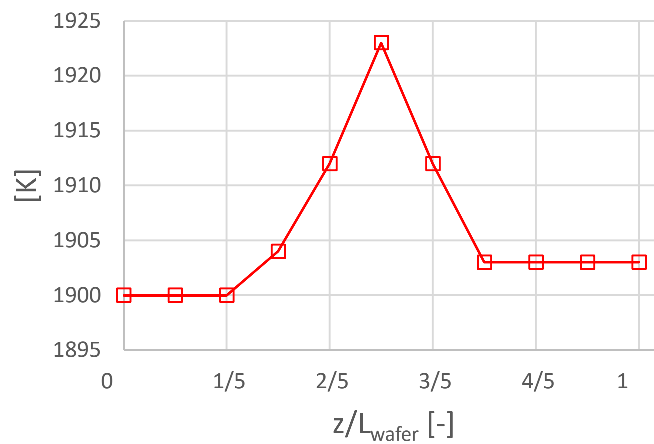

Figure 3.4: *wafer "gaussian" temperature profile, G2.*

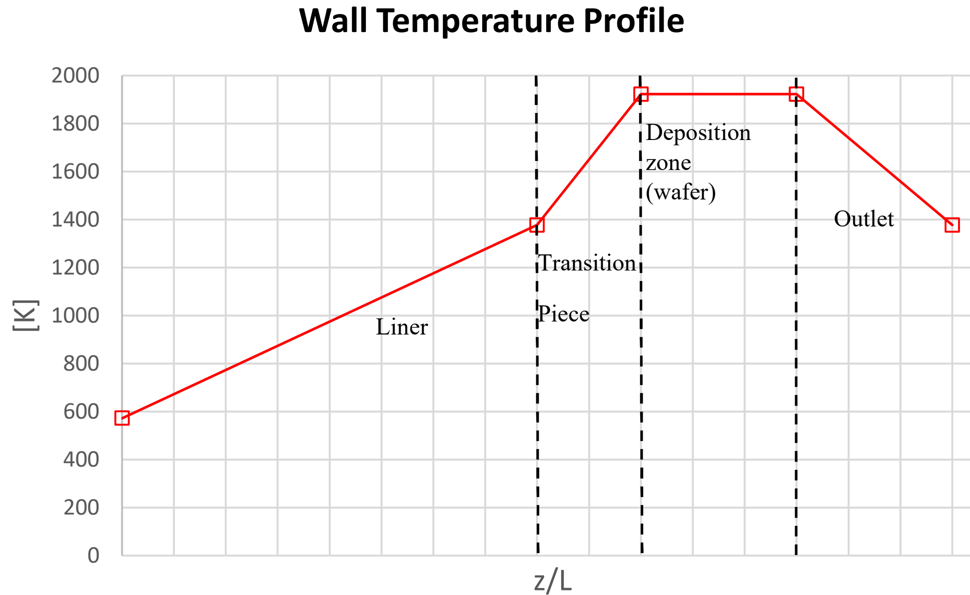

Figure 3.5: *wall temperature profile over the axial coordinate of the reactor centerline, calculated by ASM.for through linear interpolation of the imposed boundary conditions at the walls (when referring to the centerline, the front plate length can be neglected).*

From now on, if reactor geometry, mixture composition, and temperature profile adopted in the numerical monodimensional simulations analysed in this chapter are not specified, the reader must always refer to the correspondent values introduced in this subsection assuming a 1923 K flat wafer temperature profile and a 10 minutes run-time.

Regarding computational aspects of the software, the numerical integration was performed employing the Daspk 2.0 solver[49], while the uncertainty on the experimental data was assumed equal to a 10% error in an attempt to account for the approximations introduced by the monodimensional model when studying a 3D system (in some figures this error is reduced to 5% for graphic purposes). The average computational time for each simulation conducted with ASM.for was about 30 seconds.

3.1.3 Operative Conditions: Three-Dimensional Model

The reactor digital twin, schematically depicted in Figure 2.5, consist of a Fluent® mesh of 3205940 tetrahedral cells. Such mesh is coarser in the liner and outlet zones while it becomes more refined when reproducing the transition piece together with the rest of the deposition chamber; as previously mentioned, the gas is supposed to transit in the liner zone at 300 K without pre-heating in order to reduce the already high computational costs.

Similarly to the monodimensional discretization, the reactor, which works in steady-state conditions, employs an operating pressure equal to 10^4 Pa while wall temperature is set equal to 300 K in the liner zone, 1300 K in the transition piece, 1913 K on the deposition zone (front plate and susceptor) and 1913 K at the outlet section.

Since the three-dimensional model was employed to get a better insight about nitrogen incorporation, silicon carbide deposition was not accounted and N incorporation was modelled as a Neumann boundary condition on the diffusive flux. Indeed, the adopted reactor feed consists only of molecular nitrogen dispersed in a H_2 carrier gas (mass composition: 0.00013 N_2, 0.99987 H_2) and it is tripartite in three distinct ducts of the liner, a central and two lateral ones: the central duct accounts for an inlet mass flowrate of 8.3E-05 kg/s while this latter variable is equal to 3.3E-05 kg/s for both the lateral ducts.

Species diffusivities and thermal conductivities along with mixture specific heat were evaluated with Fluent correspondent standard correlations (respectively kinetic theory, polynomial law, and mixing law) assuming to work in a fully laminar regime with an ideal mixture of ideal gases. Reactor walls and susceptor surfaces were assigned constant temperature values.

Each simulation was solved employing the pseudo-transient method with 10^4 iterations and an average computational time roughly equal to two hours.

3.2 Sensitivity Analysis of the Kinetic Scheme

The starting point of this experimental study consisted in the assessment of the impact of both gas and surface reactivity on growth rate and nitrogen incorporation; this task was achieved with a sensitivity analysis based on a brute-force method: the kinetic constant of each reaction included in the kinetic scheme was systematically increased by a factor of 10 while keeping all other kinetic constants fixed to their original values and then a numerical simulation was performed (1.3 C/Si); percent variance of growth rate profile (evaluated by measuring the variation of the peak growth rate), film and doping disuniformity with respect to their reference values were evaluated and reported in three bar charts. Since all of these parameters strictly depend on the growth rate, each chart accounts only for reactions giving peak growth rate variations higher than 1%.

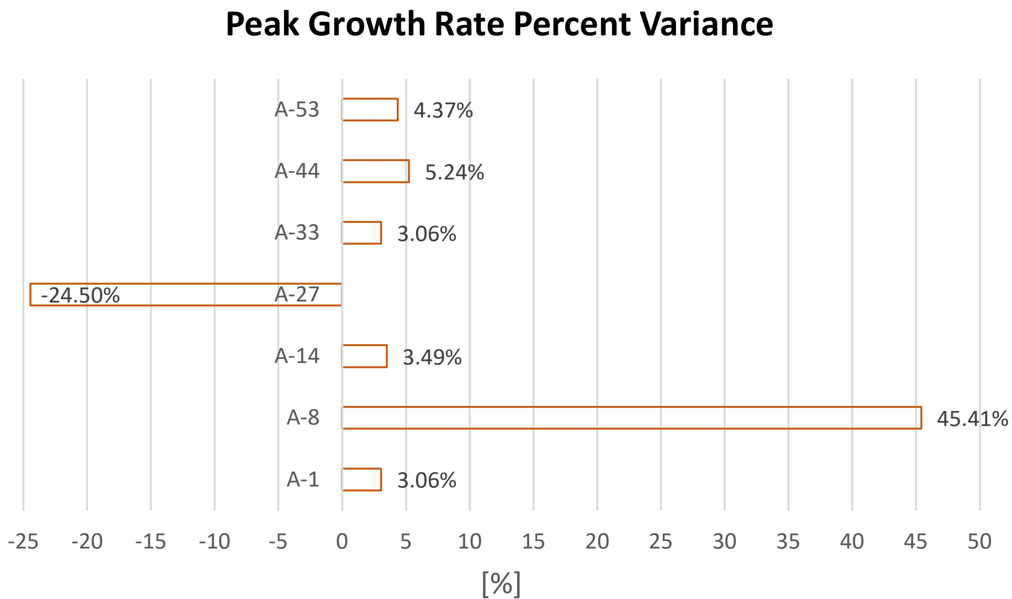

Figure 3.6: *peak growth rate percent variance from a reference value of 0.38 µm/min.*

As depicted in Figure 3.6, gas phase reactivity it is not featured since it has a negligible impact on the growth rate, probably because the system rapidly evolves to a composition similar to that of chemical equilibrium due to the high temperatures.

Moreover, a similar sensitivity analysis featuring a more detailed pyrolysis scheme performed by Cavallotti et al.[39] showed that gas phase synthesis reactions of main silicon carbide carbon precursors (CH_4, C_2H_2) have a minor effect on the growth rate profile.

Among all surface reactions, methane dissociative adsorption (A-1), silicon adsorption (A-14) and SiC^{film} formation from Si* or SiCl* (A-33, A-44, A-53) slightly alters the growth rate profile, while major variations are achieved by acetylene dissociative adsorption (A-8) and silicon desorption (A-27):

$$CH_4 + \sigma_{Si} \rightarrow C^* + 2H_2 \quad \text{(A-1)}$$

$$C_2H_2 + 2\sigma_{Si} \rightarrow 2C^* + H_2 \quad \text{(A-8)}$$

$$Si + \sigma_C \rightarrow Si^* \quad \text{(A-14)}$$

$$Si^* \rightarrow Si + \sigma_C \quad \text{(A-27)}$$

$$SiCl^* + CH^* \rightarrow SiC + HCl + \sigma_C + \sigma_{Si} \quad \text{(A-33)}$$

$$Si^* + C^* \rightarrow SiC^{film} + \sigma_C + \sigma_{Si} \quad \text{(A-44)}$$

$$Si^* + CH^* \rightarrow SiC + H + \sigma_C + \sigma_{Si} \quad \text{(A-53)}$$

This result suggests that among all the possible reactive intermediates involved in SiC deposition, C_2H_2 and Si play a key role. Film disuniformity is reported in Figure 3.7:

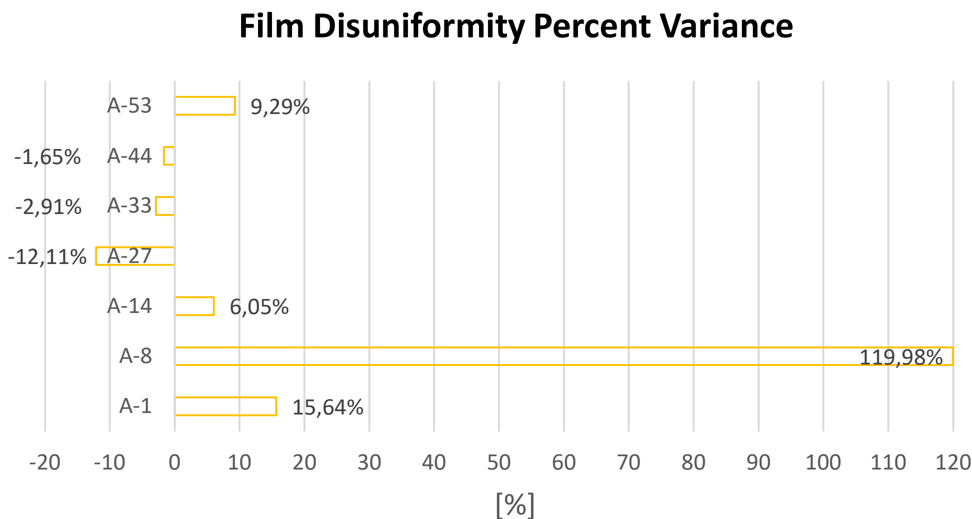

Figure 3.7: *film disuniformity percent variance from a reference value of 1.3E-02 (or 1.3%).*

Similarly to peak growth rate sensitivity, reactions A-1, A-14, A-33, A-44 and A-53 have a minor impact on film disuniformity, whilst the most significant discrepancies from the reference value are given by A-27 and A-8, with a particularly high variation for the latter reaction which increases film disuniformity up to 120% of its original value.

While variations of film disuniformity are related to variations in the growth rate profile as the former parameter is a function of the maximum and minimum values of the latter, changes in doping disuniformity are explained by the inverse proportionality between growth rate and doping (Figure 3.8): reactions A-8 and A-27 alter the growth rate which in turn perturbs nitrogen incorporation; in this sense, doping disuniformity is highly sensitive to Si desorption, with an observed increment equal to 113% of its original value.

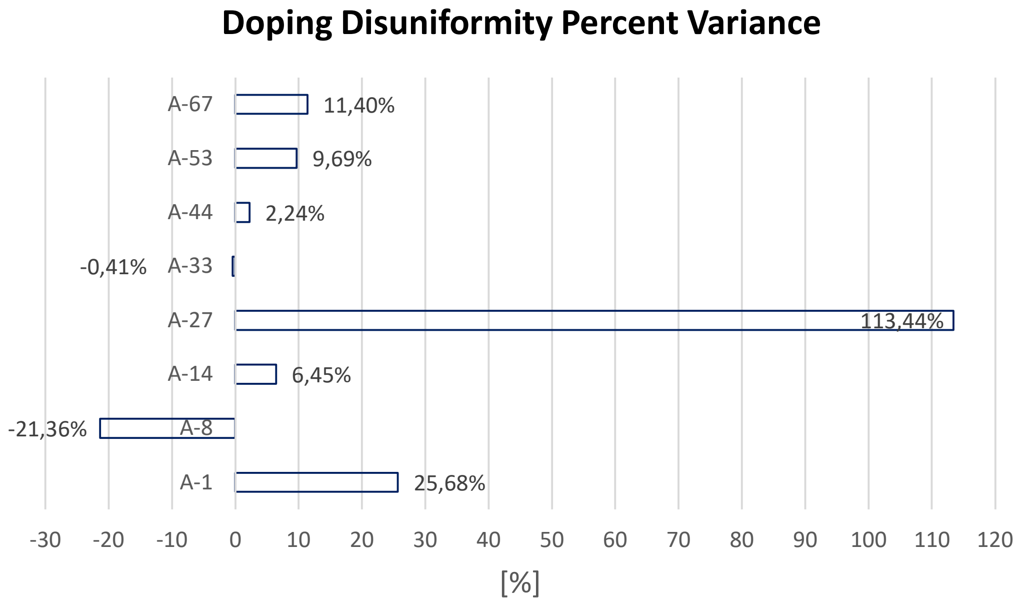

Figure 3.8: *doping disuniformity variance from a reference value of 9.8E-03 (or 0.98%).*

The marked sensitivity of nitrogen incorporation towards reactions A-27 and A-8 can be also explained from a physical point of view: the enhancement of the kinetic constant of acetylene dissociative adsorption causes an increase in the carbon containing species adsorbed onto the surface, resulting in less free Si sites available for N to bond with (accordingly to the site competition epitaxy criteria[26,27]), while the enhancement of Si desorption kinetic constant reduces the amount of adsorbed silicon decreasing nitrogen incorporation as it hinders the formation of SiN^{film} from N^* and Si^* (A-62).

Regarding the doping section of the kinetic scheme, the only reaction altering doping disuniformity is A-67, which represents the direct film incorporation of gaseous SiN:

$$SiN + \sigma_C \rightarrow SiN^{film} + \sigma_C \quad \text{(A-67)}$$

It is also worth noting that the inverse relation between growth rate and doping is not mutual: growth rate is not affected by variations of reactions included in the doping section of the kinetic scheme (after all, none of them is featured in the growth rate peak nor in the film disuniformity bar charts). As a result of this evidence, it is possible to study nitrogen doping independently from the growth rate; this assumption is justified from a physical point of view only if the simulated reactor works at high temperatures with small amounts of dopant precursor, like in most CVD reactors. Alternatively, it is known that the doping agent may alter the growth rate by modifying the Fermi level of the growing film[50].

In summary, this sensitivity test assesses that C_2H_2, CH_4, Si, $SiHCl_3$ and, to a lesser extent, SiN are the key species influencing SiC deposition and doping in terms of surface reactivity: this is somehow complementary to what stated in the thermodynamic analysis of Subsection 2.2.3 regarding gas phase reactivity.

3.3 Baseline and Optimized Simulations of Silicon Carbide Deposition

3.3.1 Comparison between Baseline Simulation and Experimental Data

Figure 3.9 displays a comparison of the still-susceptor growth rate trend evaluated over the centerline between a baseline simulation performed at the beginning of this work (no software modifications, 1.3 C/Si ratio, flat temperature profile) and the experimental data reported in Section 2.5 (the experimental growth rate profile is obtained by dividing the correspondent thickness profile by the run-time):

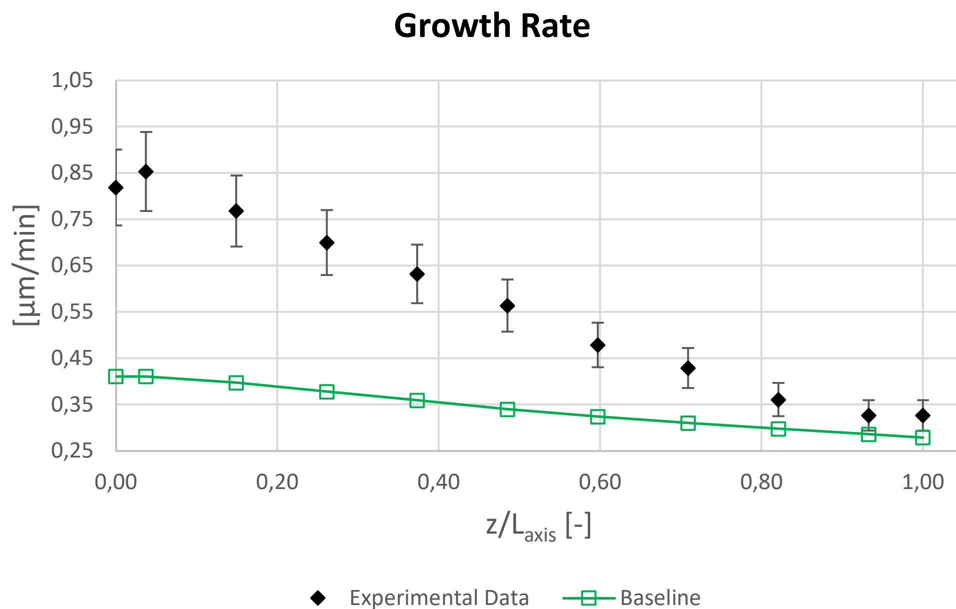

Figure 3.9: *growth rate profile over the centerline axial length, comparison between baseline simulation and experimental data;* L_{axis} *= 134 mm, 10% error bars.*

The growth rate predicted by the baseline simulation is qualitatively and quantitively inconsistent: indeed, not only the computed G.R. trend is considerably flatter than the actual experimental data distribution, but there is also a noticeable discrepancy between the two profiles with a difference of approximately 0.4 µm/min between their peak values.

Similar considerations are valid for the averaged growth rate: film disuniformity computed with the baseline simulation is equal to 0.81% while the same parameter calculated with the experimental data gives a value of 3.57%; this means that the averaged G. R. profile predicted by the baseline simulation is, once again, flatter (Figure 3.10).

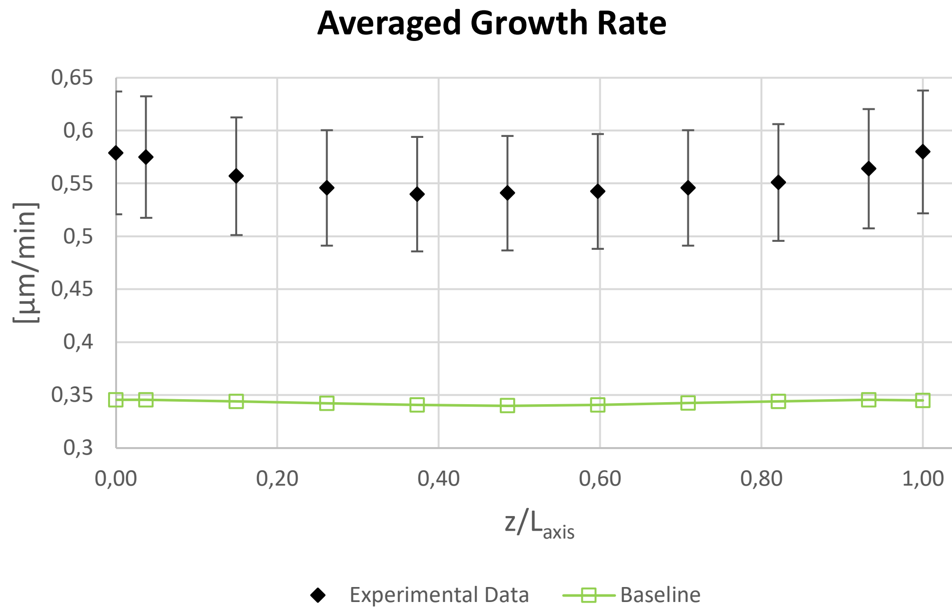

Figure 3.10: *averaged growth rate profile over the centerline axial length, comparison between baseline simulation and experimental data;* L_{axis} *= 134 mm, 10% error bars.*

The higher discrepancy between numerical and experimental growth rate might be attributed to the silicon rich and carbon rich regimes respectively employed for the real reactor and for the simulation: indeed, in the former regime growth rate is limited and therefore controlled by the amount of C_2H_4 injected in the reactor, as lower partial pressures of ethane slow the pyrolysis of hydrocarbons and alter the adsorption of carbon atoms onto the film affecting SiC deposition; the opposite is true for the latter regime, where growth rate is regulated by the $SiHCl_3$ content in the feed, which influences Si and SiH_xCl_y partial pressures (and thus silane and chlorosilanes reactivity).

Moreover, numerical nitrogen incorporation also shows important deviations and more disuniformity with respect to the experimental data trend, being the former almost one order of magnitude greater than the latter close to the end of the wafer (Figure 3.11): this could be explained by the high sensitivity and inverse proportionality of nitrogen doping towards growth rate, since deviations of the numerical growth rate might influence the numerical $[N]_{film}$.

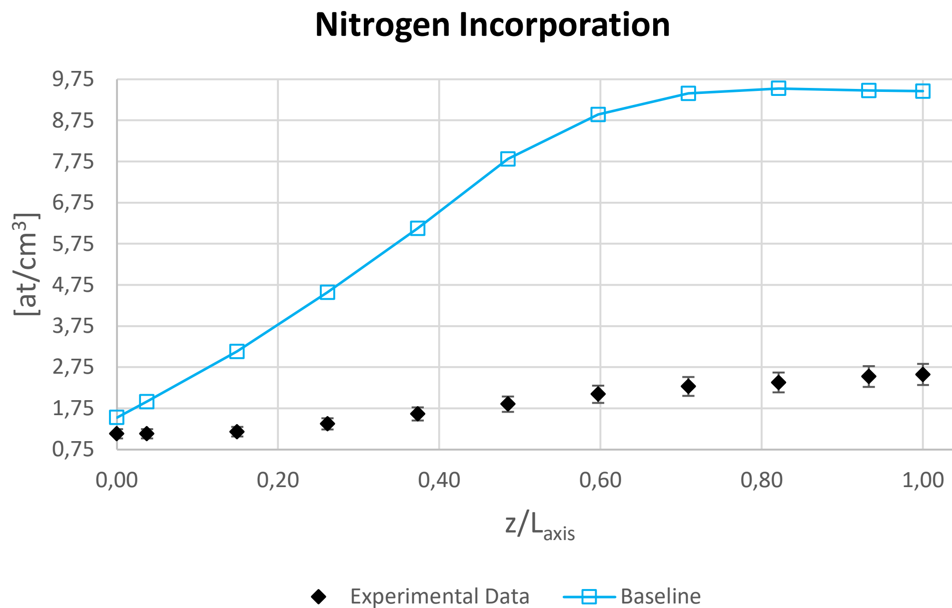

Figure 3.11: *nitrogen incorporation profile over the centerline axial length, comparison between baseline simulation and experimental data; L_{axis} = 134 mm, 10% error bars.*

3.3.2 Comparison between Optimized Simulations and Experimental Data

Results of simulations performed after the implementation of the software modifications previously exposed in Subsection 2.4.1, with a C/Si ratio of 1.3 and a flat temperature profile of 1650 K, are illustrated in Figures 3.12 and 3.13, which respectively depict the trends of the calculated averaged growth rate and averaged nitrogen incorporation:

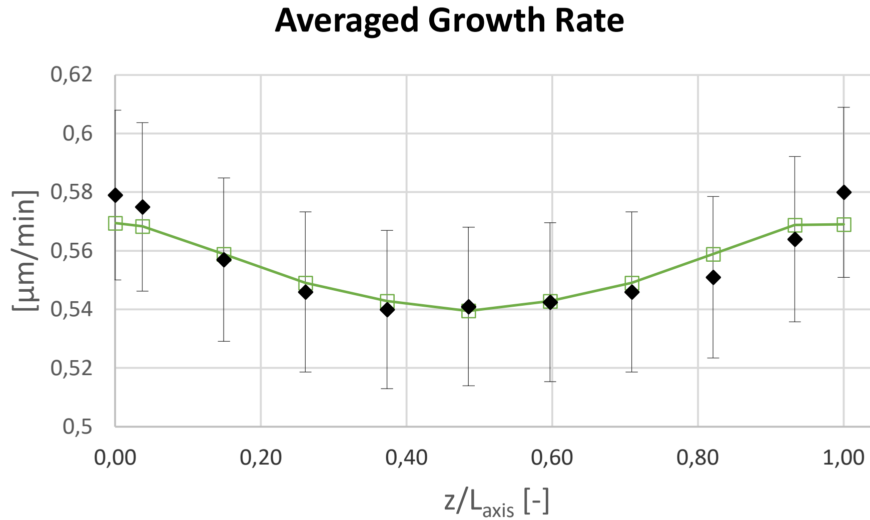

Figure 3.12: *averaged growth rate profile over the centerline axial length, comparison between optimized simulation and experimental data;* $L_{axis} = 134\ mm$*, 5% error bars.*

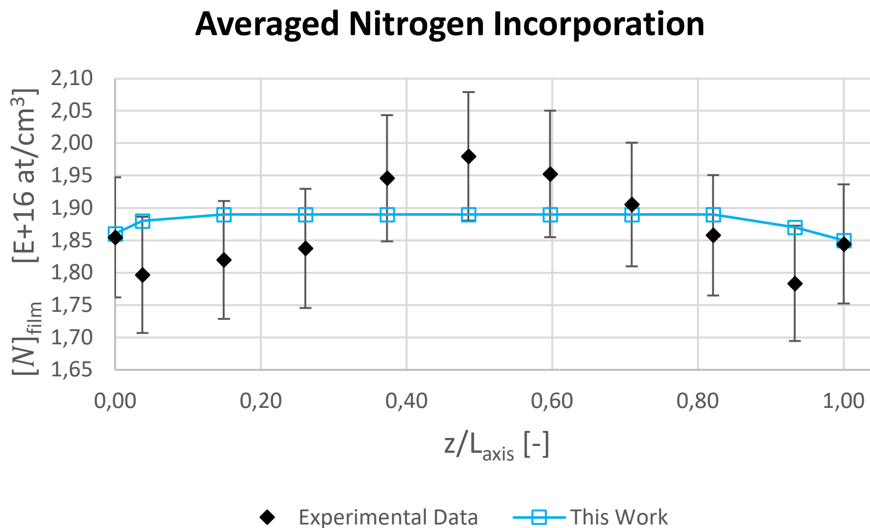

Figure 3.13: *averaged nitrogen incorporation profile over the centerline axial length, comparison between optimized simulation and experimental data;* $L_{axis} = 134\ mm$*, 5% error bars.*

The averaged G. R. profile evaluated by the simulation is in good agreement with the correspondent experimental data distribution, with a calculated film disuniformity equal to 2.61% compared to a measured one of 3.57%. On the other hand, the calculated values of averaged nitrogen incorporation differ from the measured ones: although the N doping profile quantitatively matches the experimental data, it does not replicate the W shape observed in Figure 2.10 and it is considerably flatter, with a doping disuniformity equal to 1.07% compared to the experimental one of 5.21%; this aspect was further investigated with a parametric analysis by examining the outcome of two additional simulations respectively conducted employing the two "gaussian" temperature profiles G1 and G2 of Figures 3.3 and 3.4. The averaged nitrogen incorporation trend with respect to the wafer centerline for these temperature profiles is depicted in Figure 3.14.

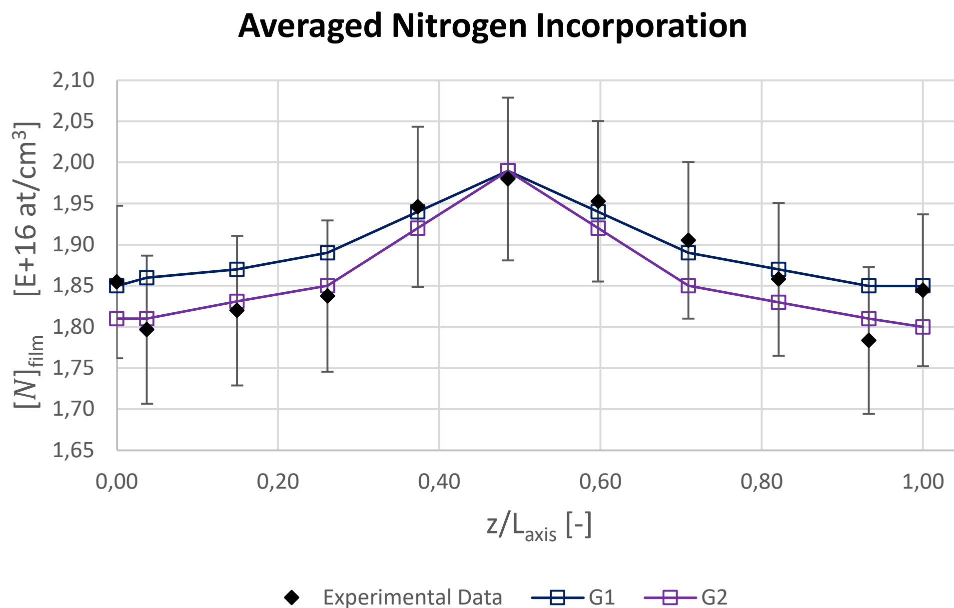

Figure 3.14: *averaged nitrogen incorporation profile over the centerline axial length, comparison between simulations conducted "gaussian" temperature profiles;* $L_{axis} = 134\ mm$.

Both simulations estimate reasonably well the experimental W distribution of nitrogen film concentration behaving in a similar manner (they predict the maximum value of $[N]_{film}$ at the centre of the wafer, but not the two peripherical minima), the main difference being a discrepancy at the inlet and outlet section of the wafer where the simulation conducted with the temperature profile G2 predict lower values of $[N]_{film}$ compared to the simulation launched with profile G1. This result suggests that even variations of few kelvins over the wafer, triggered by random thermal fluctuations or by the use of different heating zones, may have a high influence over N doping and thus it is mandatory to achieve optimal temperature control and precise temperature measurements in order to obtain a completely flat nitrogen incorporation profile.

However, N incorporation dependence on temperature is not so straight forward: indeed, temperature variation over the wafer either enhances or hinders both gas and surface reactions altering the C/Si ratio along the reactor axis, which in turn acts on growth rate and nitrogen doping. Hence, a more detailed analysis is required, studying the complex interplay among several parameters triggered by thermal variations (kinetic constants, diffusivity coefficients, molar fluxes and so on) with more detailed kinetic schemes if they will be available for the upcoming years or perhaps by describing SiC deposition and doping with a 3D model, even if this will inevitably raise the computational time required to run a simulation.

3.4 Study of the Enhanced Nitrogen Incorporation at Wafer Edges

To further investigate the experimental evidence of enhanced nitrogen incorporation at the wafer edges in the still susceptor configuration due to the effect of possible wall reactions occurring onto the front plate as hypothesized at the end of Section 2.5, the whole nitrogen doping section of the kinetic scheme (G-126÷G-139, A-57÷A-67) was lumped in a single irreversible surface reaction, which represents the direct incorporation of a generic gaseous dopant species inside the silicon carbide film:

$$\mathrm{Dopant} + \mathrm{M} \rightarrow \mathrm{SiN}^{\mathrm{film}} + \mathrm{M} \qquad \textit{Dopant Incorporation Reaction}\ \mathrm{(R3.1)}$$

Being M the deposition surface of the film; pre-exponential factor, temperature exponential coefficient, and activation energy for R3.1 were assumed equal to the correspondent parameters of SiN incorporation (A-67), while thermochemical properties of Dopant were set equal to the ones of SiN. Mixture composition was then altered by substituting N_2 with the dopant agent and the inlet molar fraction of this latter species was fitted to reproduce the N incorporation experimental trend (0.998032 H_2, 0.001138 $SiCl_3$, 0.00074 C_2H_4, 9E-05 Dopant), as shown in Figure 3.15.

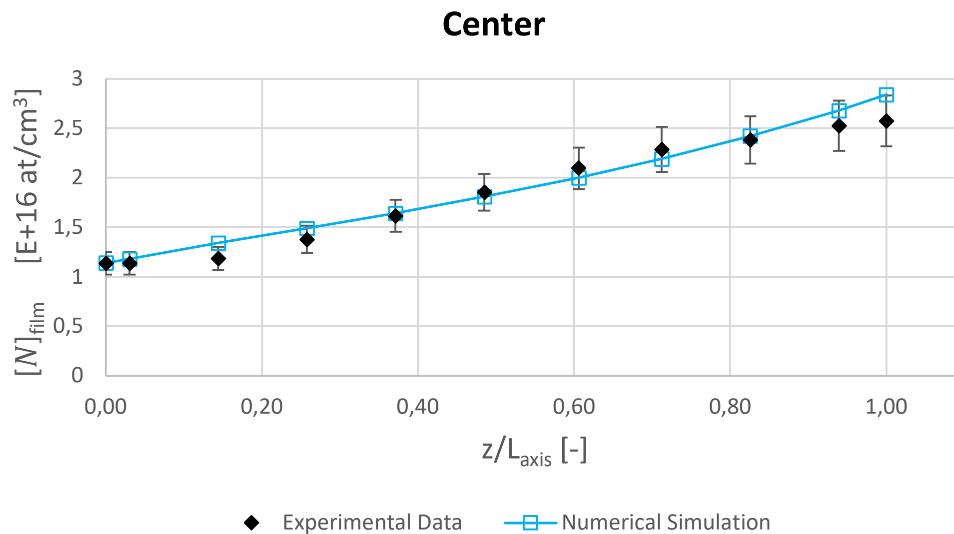

Figure 3.15: *fitted N incorporation profile along the axial length of the centerline;* $L_{axis} = 134\ mm$*, 10% error bars.*

In order to simulate nitrogen doping also over the lateral horizontal sectors of the wafer, the focus was consequently shifted to the other four horizontal coordinates of the right portion of the wafer introduced in Subsection 3.1.1 (R2, R3, R5, R6) assuming negligible variations in nitrogen incorporation between the wafer right and the left side; a horizontally displaced simulation was run along the axial length of each of these abscissas employing the lumping reaction R3.1 and accounting for a dopant inlet molar fraction varying with the proportional law:

$$y_{dopant}(X) = y_{dopant}^{centerline} * \frac{L_{inlet}(X)}{L_{inlet}(X = 0\ mm)} \tag{3.9}$$

$$L_{inlet}(X) = L_{liner} + L_{transition\ piece} + L_{front\ plate}(X) \tag{3.10}$$

Relation 3.9 evaluates the molar fraction of dopant for a generic horizontal coordinate X, $y_{dopant}(X)$, as the dopant molar fraction at the centerline, $y_{dopant}^{centerline} = 9E-05$, multiplied by the ratio between the inlet lengths of the generic abscissa and the centerline, $\frac{L_{inlet}(X)}{L_{inlet}(X=0\ mm)}$. The numerical nitrogen incorporation trends for each horizontal coordinate are reported in Figures 3.16, 3.17, 3.18 and 3.19: dopant molar fraction was fitted only when the value predicted by Eq. (3.9) failed to produce a satisfying agreement with the experimental data.

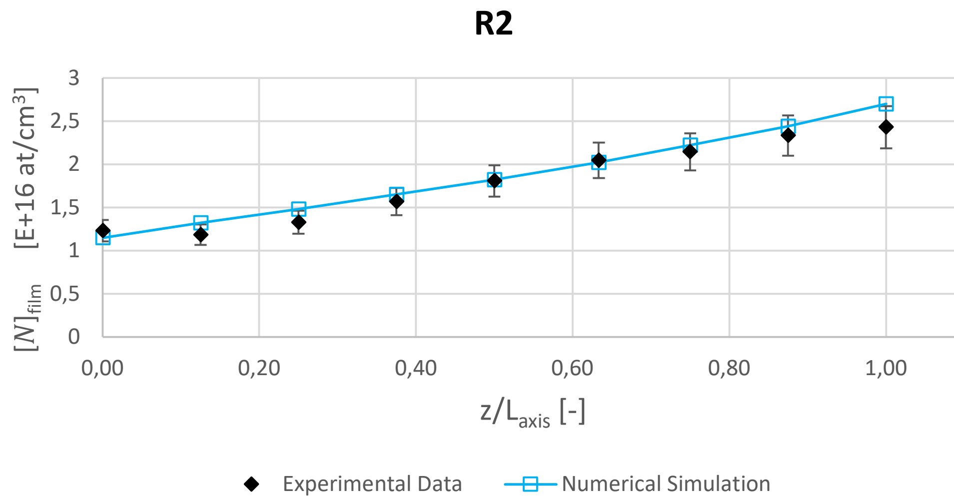

Figure 3.16: *nitrogen incorporation profile along the axial length of abscissa R2;*

X = 30 mm, L_{axis} = 120 mm, y_{dopant} = 9.13E-05, 10% error bars.

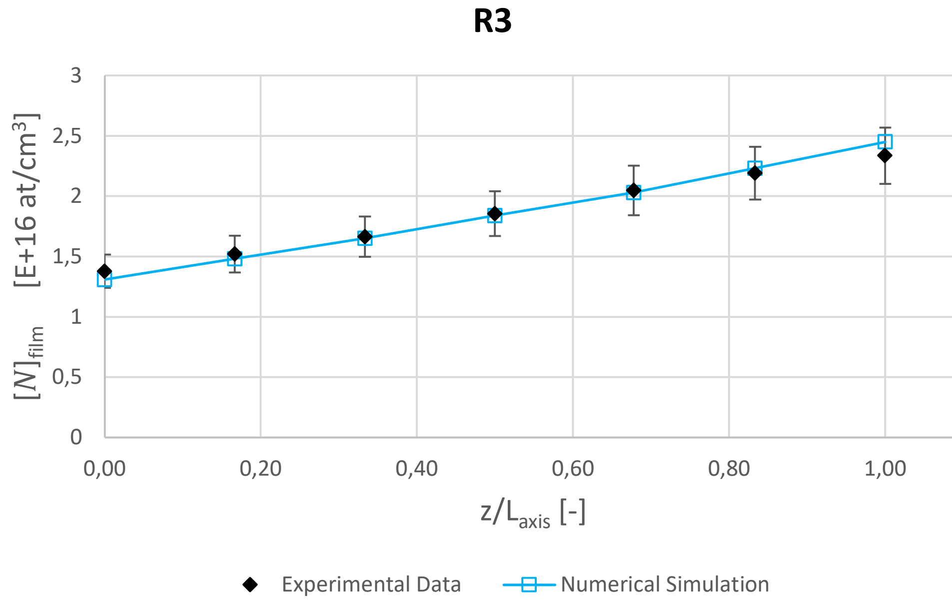

Figure 3.17: *nitrogen incorporation profile along the axial length of abscissa R3;*

X = 45 mm, L_{axis} = 90 mm, y_{dopant} = 9.27E-05, 10% error bars.

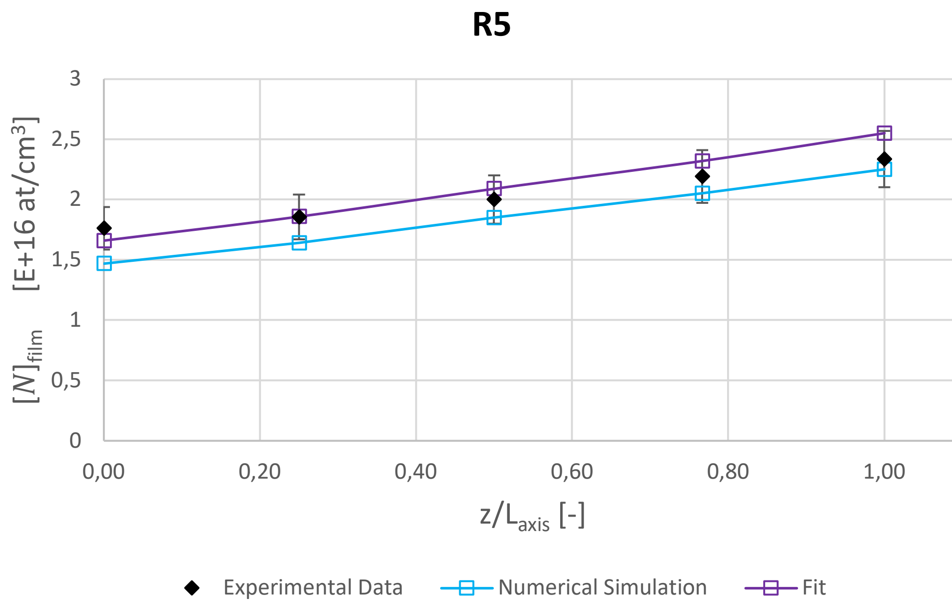

Figure 3.18: *nitrogen incorporation profile along axial length of abscissa R5;*

X = 60 mm, L_{axis} = 60 mm, y_{dopant} = 9.54E-05, $y_{dopant,fit}$ = 1.08E-04, 10% error bars.

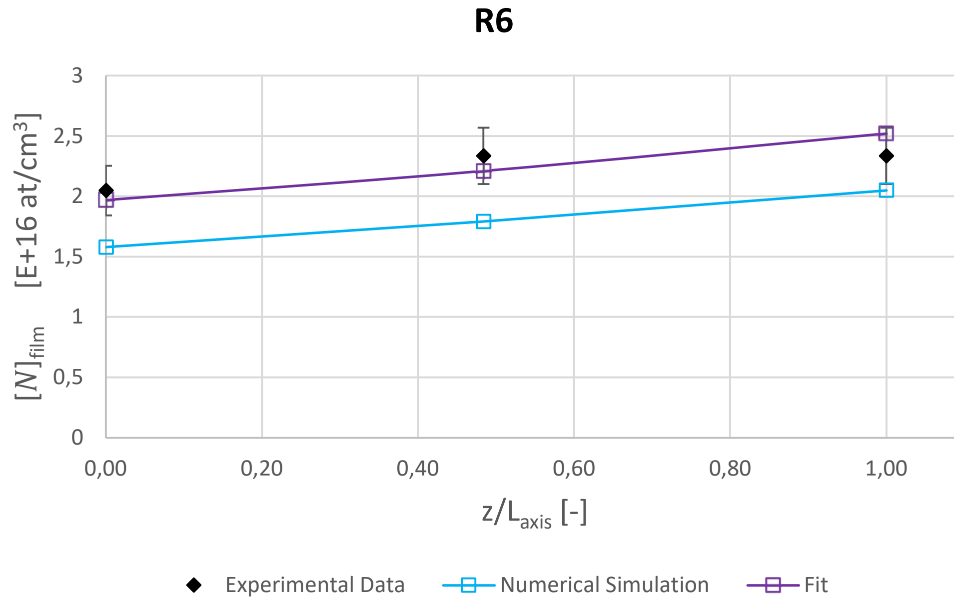

Figure 3.19: *nitrogen incorporation profile along the axial length of abscissa R6;*

X = 65 mm, L_{axis} = 31 mm, y_{dopant} = 9.74E-05, $y_{dopant,fit}$=1.21E-04, 10% error bars.

As it can be seen, curve fitting was required for abscissas 5 and 6, where the inlet dopant molar fraction had to be increased, while for the remaining coordinates the calculated doping profile is already in good accordance with the experimental data. This evidence indicates that the values of y_{dopant} predicted by the proportional relation are only able to justify data gathered from abscissas close to the centerline like R2 and R3 (Figure 3.20).

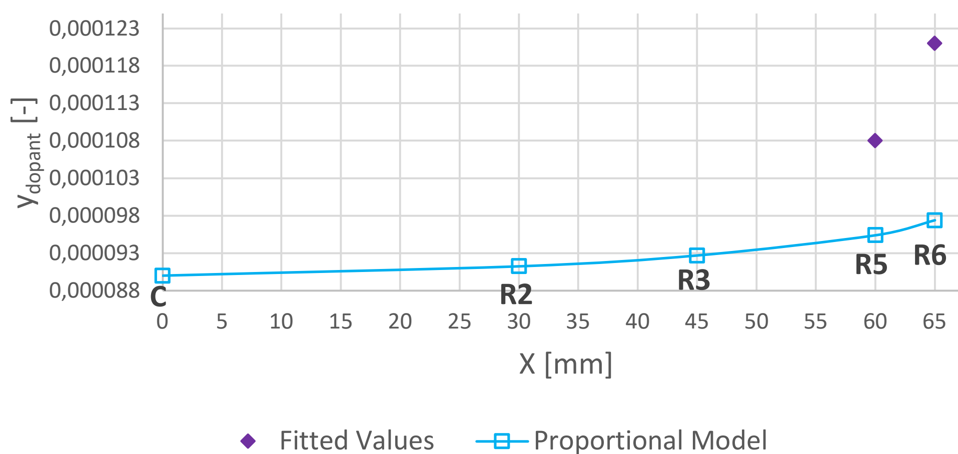

Figure 3.20: *inlet dopant molar fraction predicted by the proportional relation for each abscissa versus distance from the centerline.*

As it can be observed, when considering the horizontal coordinates R5 and R6, Figure 3.20 depicts a significant discrepancy between the inlet dopant molar fraction fitted values and the correspondent parameters predicted by the proportional relation Eq. (3.9).

Figure 3.20 also shows that y_{dopant} must monotonically increase from the centerline to the wafer edges in order to match the experimental data: this trend is coherent from a physical point of view as if the dopant content in the reactor feed is raised then there are more dopant molecules which can be incorporated inside the silicon carbide film and this obviously leads to higher values of $[N]_{film}$.

This evidence might also confirm what stated in Section 2.5: the enhanced nitrogen incorporation observed at wafer edges in the still susceptor configuration of PE-106 could effectively be explained by gas phase reactions occurring over the front plate which converts molecular nitrogen into a doping intermediate; since the front plate is longer at the edges, the residence time of the gas in these zones will be higher and more doping intermediate can be formed augmenting nitrogen incorporation. In these monodimensional simulations, this phenomenon was replicated in a simplified manner when increasing the inlet molar fraction of the generic dopant in all the horizontally displaced simulations.

3.4.1 Three-Dimensional Simulations

In order to properly test the N incorporation mechanism triggered by the formation of a dopant intermediate mentioned in this section, a 3D simulation was run in Fluent adopting the boundary conditions resumed in Subsection 3.1.3 with a still susceptor. The dopant intermediate was assumed to be NH_3, synthesized inside the gas phase by reaction of N_2 with the H_2 carrier gas:

$$1/2\ N_2 + 3/2\ H_2 \rightarrow NH_3 \qquad \text{(R3.2)}$$

Consequently, N deposition was modelled theorizing a single wall surface reaction occurring exclusively onto the susceptor surface and representing ammonia decomposition to produce bulk (solid) atomic nitrogen and gaseous hydrogen:

$$NH_3 + \text{wall} \rightarrow N_{(bulk)} + 3/2\ H_2 \qquad \text{(R3.3)}$$

The kinetic constant of reaction R3.3 was evaluated from the Transition State Theory applied to NH_3 adsorption ($NH_3 + \text{wall} \rightarrow NH_3{}^*$):

$$k_{ads} = \frac{k_B T}{h_P} \frac{Q_{transl.}^{(\neq)} Q_{rot.}^{(\neq)} Q_{vib.}^{(\neq)}}{Q_{transl.}^{(R)} Q_{rot.}^{(R)} Q_{vib.}^{(R)}} \qquad (3.11)$$

Being k_B the Boltzmann constant, equal to 1.3806E-23 $m^2kg/s^2/K$, h_P Planck's constant, equal to 6.62607E-34 m^2kg/s, and $Q_{transl.}^{()}$, $Q_{rot.}^{()}$ $Q_{vib.}^{()}$ respectively the translational, rotational and vibrational partition functions referred to the transition state, ($\neq$), or to the reactant, (R). Under the assumption of null or very low activation energy, at the transition state the molecule is free to move in two directions parallel to the surface while preserving the same rotation and vibrational partition functions of the correspondent gas molecule; moreover, inside the gaseous phase the molecule is free to translate in three directions.

Thus, Eq. (3.11) further simplifies into:

$$k_{ads} \approx \frac{k_B T}{h_P} \frac{Q_{transl.}^{(\neq)}}{Q_{transl.}^{(R)}} = \frac{k_B T}{h_P} \frac{\left(\frac{2\pi K_B T m_{NH_3}}{{h_P}^2}\right)^{\frac{2}{2}}}{\left(\frac{2\pi K_B T m_{NH_3}}{{h_P}^2}\right)^{\frac{3}{2}}} = \sqrt{\frac{k_B T}{2\pi m_{NH_3}}} \quad (3.12)$$

Where m_{NH_3} is the mass of an ammonia molecule, defined as NH_3 molecular weight divided by Avogadro's constant (6.022E+23 mol^{-1}) and equal to 2.83E-26 kg.

The value of k_{ads} predicted by the TST, equal to 385.53 m/s, was decreased to 6 m/s in order to account for the efficiency of the surface process. Then, the kinetic constant of reaction R3.2, expressed as $k_{R3.2} = A_{R3.2} T^{\alpha} e^{E_{act}/R_{gas}T}$ ($E_{act} = 0$ kcal/mol, $\alpha = 0.5$), was calculated by fitting the N surface deposition rate, representing the amount of atomic nitrogen deposited over time from NH_3 decomposition, until it matched the mass flux of precursor towards the surface evaluated with the monodimensional simulation performed over the central axis of the wafer presented in Figure 3.15.

This is why the fitted monodimensional simulation is the only one able to match the full set of experimental data regarding nitrogen incorporation, thus if the doping mechanism proposed in this section actually occurs in the real reactor then the calculated precursor mass flux should be close to its correspondent experimental value at least in terms of order of magnitude. Since the activation energy of R3.2 was assumed to be null, then the kinetic constant of this reaction reduces to the product of pre-exponential factor and temperature:

$$k_{R3.2} = A_{R3.2} T^{0.5} \quad (3.13)$$

The fitted value of the pre-exponential factor of R3.2 is $A_{R3.2} = 6.8\text{E} - 08 \frac{m^3}{kmol*K^{0.5}*s}$.

The outcome of this simulation is resumed in Figure 3.21, which illustrates the deposition rate of atomic nitrogen over the surface of the still susceptor:

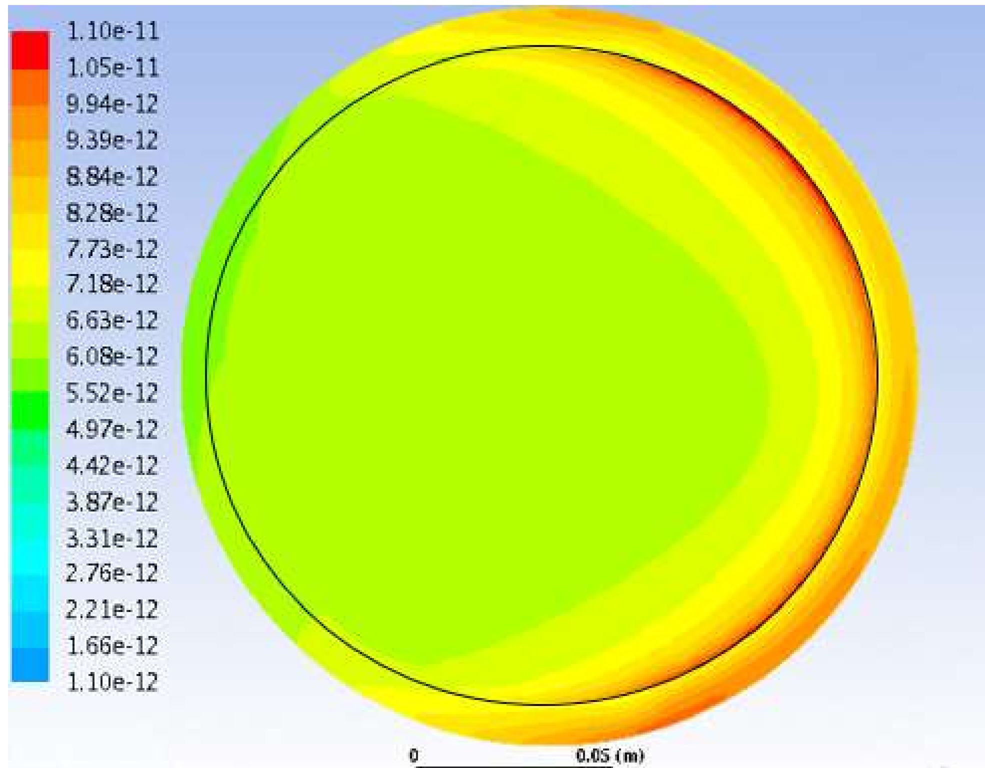

Figure 3.21: *colormap of N deposition rate in the still susceptor configuration, units in kg/m²/s; the black circle marks the perimeter of the wafer in order to distinguish it from other regions of the susceptor onto which it is supported (the wafer starts from the right black border and ends with the left one).*

As previously stated, the N deposition rate represent the amount of nitrogen deposited over time onto the surface, so it can be employed to study the trend of N bulk concentration (it is indeed a growth rate related to nitrogen deposition): obviously, zones with high deposition rate will consequently have high nitrogen concentration. Looking at Figure 3.21, these latter zones coincide with wafer edges, where the N deposition rate ranges in the interval 9.94E-12÷1.10E-11 $kg/m^2/s$ (red crest of Figure 3.21) and gradually decreases when moving towards the centerline reaching values close to 5.52E-12÷6.08E-12 $kg/m^2/s$ (greenish area of Figure 3.21).

What emerges from this three-dimensional simulation is that the calculated doping trend at the lateral sectors of the wafer resembles the experimental one (on the other hand, this is not true for zones of the wafer close to the centerline as the effect of the growth rate on nitrogen incorporation is not accounted in the 3D simulations so these latter zones do not display the monotonically decay observed in Figure 2.12); therefore, the excessive nitrogen incorporation observed in the still susceptor configuration (Figure 2.12) could be explained by enhanced formation of NH_3, or a similar dopant intermediate, on the lateral sides of the front plate due to the geometrical shape of this latter element. In theory, it should be possible to limit this phenomenon with a reduction of the wafer diameter in order to bypass the lateral stream of gas coming from the front plate; another solution could be either a better flow distribution or the employment of a more efficient dopant precursor which incorporates directly into the wafer without intermediate reactions.

Another explanation consists in the inverse proportionality between boundary layer thickness and dopant diffusive flux: indeed, the gaseous stream contacts first the portion of the wafer close to the centerline and then its lateral sides, thus the boundary layer develops earlier in the former zone; obviously, lower boundary layer thickness at the edges implies greater dopant diffusive flux which in turn causes enhanced nitrogen incorporation. However, due to the minor quantity of N_2 injected in the carrier gas, this latter phenomenon is not so relevant or at it least it has a minor impact on the system (it affects instead the growth rate due to the higher molar fraction of C_2H_4 in the feed).

CHAPTER 4

Conclusions and Future Prospects

This thesis work was devoted to the study of the kinetic and fluid dynamic behaviour of silicon carbide film growth and nitrogen doping conducted inside an industrial chemical vapour deposition reactor: several numerical simulations were performed with the softwares ASM.for, a Fortran program based on a monodimensional discretization of the epitaxy reactor PE-106, and Fluent, which was employed to model the same reactor in a three-dimensional environment.

A sensitivity analysis conducted at the beginning of this work allowed to identify the key species affecting silicon carbide deposition and nitrogen doping, which were found to be mainly C_2H_2, CH_4, Si, and $SiHCl_3$, with a minor role played by gaseous SiN.

Then, after a series of software fixes applied to ASM.for, optimized simulations were launched in an attempt to replicate the experimental trends of growth rate and nitrogen doping gathered from two test runs of PE-106, taking as reference a baseline simulation without software modifications: the fixes applied to ASM.for enhanced the quality of the simulations, which proved to be more adherent to the experimental data; satisfactory results have been achieved in terms of modelling of silicon carbide deposition, while nitrogen doping still requires the implementation of additional fixes, either on certain sections of the software or directly on the kinetic scheme in order to better describe the chemistry of the system: this is why the simulated wafer flat temperature profile was unable to replicate the W trend observed in the rotating susceptor configuration of the real reactor, while it is possible to obtain this latter trend by applying a temperature profile with a central maximum.

Subsequently, the focus was shifted to the study of the experimental nitrogen doping trend and its anomalies: the uneven N incorporation observed at the lateral zones of the silicon carbide film was investigated with a simplified monodimensional simulation featuring a fictitious dopant species; this phenomenon was supposed to be triggered by gas phase reactions converting molecular nitrogen into a dopant intermediate over the reactor's front plate, with an augmented intermediate formation at the edges of this latter element due to the higher residence time of the gaseous precursors in those zones. This hypothesis was tested with a more detailed kinetic mechanism in a three-dimensional simulation, employing ammonia as dopant intermediate formed by reaction of N_2 with hydrogen; the outcome of these computations suggests that the system could benefit either from a reduction of the wafer's diameter or by the use of a more efficient dopant precursor.

Future improvements could consist in the development of a mono or three-dimensional model including silicon carbide film growth and featuring a more detailed kinetic scheme able to describe both gaseous and surface reactivities of nitrogen incorporation. The same model could be also employed to study other chemical vapour deposition systems operating with different doping precursors.

APPENDIX I

Gas phase kinetic mechanism

$k = AT^{\alpha}e^{-E_{act}/RT}$, parameters expressed in units consistent with mol, cm^3, s, kcal.

→ denotes a forward reaction, ⇄ denotes a reversible reaction.

$Si_xD_yCl_z$ species are isomers of their correspondent $Si_xH_yCl_z$ species (D is a hydrogen atom).

Index	Reaction	Log_{10} A	α [-]	E_{act} [kcal/mol]
G-1	$CH_4 \rightleftarrows CH_3 + H$	16.38	0.00	10.38
G-2	$C_2H_2 \rightleftarrows C_2H + H$	15.25	0.00	12.47
G-3	$C_2H_5 \rightleftarrows C_2H_4 + H$	10.80	0.40	39.20
G-4	$2CH_3 \rightleftarrows C_2H_6$	15.01	-0.64	0.00
G-5	$C_3H_8 \rightleftarrows C_2H_5 + CH_3$	22.42	-1.80	88.69
G-6	$2CH \rightleftarrows C_2H_2$	14.08	0.00	0.00
G-7	$CH_2 + H \rightleftarrows CH + H_2$	13.48	0.00	0.00
G-8	$CH_2 + H_2 \rightleftarrows CH_3 + H$	13.30	0.50	0.00
G-9	$CH_2 + CH \rightleftarrows C_2H_2 + H$	13.60	0.00	0.00
G-10	$2CH_2 \rightleftarrows C_2H_4$	12.01	0.00	0.00
G-11	$2CH_2 \rightleftarrows C_2H_2 + 2H$	14.03	0.00	0.795
G-12	$2CH_2 \rightleftarrows C_2H_2 + H_2$	13.08	0.00	0.795
G-13	$CH_4 + H \rightleftarrows CH_3 + H_2$	3.600	3.16	0.009
G-14	$CH_3 + CH \rightleftarrows C_2H_3 + H$	13.47	0.00	0.00
G-15	$CH_3 + CH_2 \rightleftarrows C_2H_4 + H$	13.25	0.00	0.00
G-16	$2CH_3 \rightleftarrows C_2H_5 + H$	21.06	0.00	26.38

G-17	$CH_4 + CH \rightleftarrows C_2H_5$	14.21	0.00	0.00
G-18	$CH_4 + CH \rightleftarrows C_2H_4 + H$	13.48	0.00	-0.40
G-19	$CH_4 + CH_2 \rightleftarrows C_2H_6$	13.01	0.00	0.00
G-20	$CH_4 + CH_2 \rightleftarrows 2CH_3$	13.11	0.50	0.00
G-21	$CH_4 + CH_3 \rightleftarrows C_2H_5 + H_2$	13.01	0.00	22.85
G-22	$C_2H + H_2 \rightleftarrows C_2H_2 + H$	13.06	0.00	2.881
G-23	$C_2H + CH_2 \rightleftarrows C_2H_2 + CH$	13.25	0.00	0.00
G-24	$C_2H + CH_4 \rightleftarrows C_2H_2 + CH_3$	12.25	0.00	0.497
G-25	$C_2H_2 + H \rightleftarrows C_2H_3$	12.74	0.00	2.412
G-26	$C_2H_2 + H_2 \rightleftarrows C_2H_3 + H$	12.38	0.00	64.97
G-27	$2C_2H_2 \rightleftarrows C_2H_3 + C_2H$	12.98	0.00	84.45
G-28	$C_2H_3 + M \rightleftarrows C_2H_2 + H + M$	15.48	0.00	31.79
G-29	$C_2H_3 + H_2 \rightleftarrows C_2H_4 + H$	4.480	2.63	0.854
G-30	$C_2H_3 + CH_2 \rightleftarrows C_2H_2 + CH_3$	13.25	0.00	0.00
G-31	$C_2H_3 + CH_3 \rightleftarrows C_2H_2 + CH_4$	11.59	0.00	0.00
G-32	$C_2H_3 + CH_4 \rightleftarrows C_2H_4 + CH_3$	0.159	4.02	5.472
G-33	$C_2H_4 + M \rightleftarrows C_2H_2 + H_2 + M$	16.54	0.00	71.50
G-34	$C_2H_4 + M \rightleftarrows C_2H_3 + H + M$	17.41	0.00	96.60
G-35	$C_2H_4 + H_2 \rightleftarrows C_2H_5 + H$	13.01	0.00	68.15
G-36	$C_2H_4 + C_2H_2 \rightleftarrows 2C_2H_3$	13.38	0.00	68.35
G-37	$2C_2H_4 \rightleftarrows C_2H_3 + C_2H_5$	14.68	0.00	71.53
G-38	$C_2H_5 + H \rightleftarrows C_2H_6$	13.56	0.00	0.00
G-39	$C_2H_5 + H_2 \rightleftarrows C_2H_6 + H$	0.492	3.60	8.451
G-40	$C_2H_5 + CH_3 \rightleftarrows C_2H_4 + CH_4$	13.30	0.50	0.00
G-41	$C_2H_5 + CH_4 \rightleftarrows C_2H_6 + CH_3$	-1.060	4.14	12.56
G-42	$C_2H_5 + C_2H \rightleftarrows C_2H_2 + C_2H_4$	12.25	0.00	0.00
G-43	$C_2H_5 + C_2H_2 \rightleftarrows C_2H + C_2H_6$	11.43	0.00	23.45

G-44	$C_2H_5 + C_2H_3 \rightleftarrows C_2H_2 + C_2H_6$	11.68	0.00	0.00
G-45	$C_2H_5 + C_2H_4 \rightleftarrows C_2H_6 + C_2H_3$	2.820	3.13	18.01
G-46	$2C_2H_5 \rightleftarrows C_2H_6 + C_2H_4$	12.86	0.00	1.073
G-47	$H_2 + H \rightarrow 3H$	14.35	0.00	96.07
G-48	$2H_2 \rightarrow 2H + H_2$	14.95	0.00	96.07
G-49	$2H + H_2 \rightarrow 2H_2$	16.96	-0.60	0.00
G-50	$2H + M \rightarrow H_2 + M$	18.73	-1.30	0.00
G-51	$SiH_4 \rightleftarrows SiH_2 + H_2$	27.28	-4.91	57.32
G-52	$Si_2 \rightleftarrows 2Si$	15.00	0.00	74.43
G-53	$Si_2H_4 \rightleftarrows Si + SiH_4$	13.15	0.54	57.58
G-54	$Si_2H_4 \rightleftarrows Si_2H_2 + H_2$	14.49	0.00	53.03
G-55	$Si_2H_6 \rightleftarrows SiH_2 + SiH_4$	10.25	1.70	50.20
G-56	$Si_2H_6 \rightleftarrows Si_2H_4 + H_2$	9.950	0.00	54.22
G-57	$Si_3H_8 \rightleftarrows SiH_2 + Si_2H_6$	12.84	1.00	52.70
G-58	$SiH_2 + H \rightleftarrows SiH + H_2$	13.08	0.00	0.00
G-59	$SiH_2 + Si \rightleftarrows Si_2 + H_2$	14.17	0.00	0.00
G-60	$SiH_2 + Si \rightleftarrows Si_2H_2$	12.86	0.00	1.987
G-61	$2SiH_2 \rightleftarrows Si_2H_2 + H_2$	14.81	0.00	0.00
G-62	$SiH_4 + Si \rightleftarrows 2SiH_2$	12.97	0.00	1.987
G-63	$SiH_4 + Si \rightleftarrows Si_2H_2 + H_2$	14.17	0.00	7.292
G-64	$SiH_4 + SiH \rightleftarrows Si_2H_4 + H$	14.47	0.00	9.011
G-65	$SiH_4 + SiH \rightleftarrows Si_2H_5$	14.61	0.00	0.00
G-66	$Si_2 + H \rightleftarrows Si + SiH$	13.71	0.00	5.305
G-67	$Si_2 + H_2 \rightleftarrows 2SiH$	13.18	0.00	40.02
G-68	$Si_2 + H_2 \rightleftarrows Si_2H_2$	13.18	0.00	1.987
G-69	$Si_2H_4 + H_2 \rightleftarrows SiH_2 + SiH_4$	13.97	0.00	0.00
G-70	$Si_2H_4 + SiH_4 \rightleftarrows SiH_2 + Si_2H_6$	14.24	0.4	0.00

G-71	$Si_2H_6 + H \rightleftarrows Si_2H_5 + H_2$	14.16	0.00	2.484
G-72	$SiH_3Cl \rightleftarrows SiHCl + H_2$	14.39	0.00	68.40
G-73	$SiH_2Cl_2 \rightleftarrows SiHCl + HCl$	14.84	0.00	75.8
G-74	$Si + HCl \rightleftarrows SiCl + H$	14.98	0.00	13.60
G-75	$Si + H_2 \rightleftarrows SiH_2$	12.08	0.50	0.00
G-76	$SiH_2Cl_2 \rightleftarrows SiCl_2 + H_2$	13.92	0.00	77.40
G-77	$SiCl_4 \rightleftarrows SiCl_3 + Cl$	15.68	0.00	111.2
G-78	$SiHCl_3 + H \rightleftarrows SiCl_3 + H_2$	12.39	0.00	2.500
G-79	$HCl \rightleftarrows H + Cl$	13.64	0.00	81.73
G-80	$Cl + H_2 \rightleftarrows HCl + H$	13.68	0.00	5.258
G-81	$SiCl + HCl \rightleftarrows SiCl_2 + H$	13.80	0.00	19.490
G-82	$SiCl_3 + H \rightarrow SiHCl_3$	13.39	0.08	-0.170
G-83	Reverse	17.71	-0.75	93.82
G-84	$SiHCl_2 + H \rightarrow SiH_2Cl_2$	13.15	0.18	-0.410
G-85	Reverse	17.94	-0.70	93.13
G-86	$SiHCl_3 + H \rightarrow SiCl_3 + H_2$	8.870	1.60	2.690
G-87	Reverse	5.121	2.44	13.87
G-88	$SiCl_3 + HCl \rightarrow SiCl_4 + H$	2.080	3.08	11.79
G-89	Reverse	9.970	1.47	19.03
G-90	$SiCl_3 + SiHCl_3 \rightarrow SiCl_4 + SiHCl_2$	4.580	2.66	18.03
G-91	Reverse	5.170	2.57	17.17
G-92	$SiHCl_2 + HCl \rightarrow SiHCl_3 + H$	2.380	3.00	12.00
G-93	Reverse	9.680	1.48	20.09
G-94	$SiH_2Cl_2 + H \rightarrow SiHCl_2 + H_2$	9.090	1.62	2.810
G-95	Reverse	5.350	2.39	14.75
G-96	$SiHCl_2 + SiHCl_3 \rightarrow SiH_2Cl_2 + SiCl_3$	3.709	2.98	6.140
G-97	Reverse	3.757	3.04	5.410

G-98	$SiHCl_3 \rightarrow SiCl_2 + HCl$	17.30	-0.73	72.40
G-99	Reverse	4.301	2.33	15.00
G-100	$SiHCl_3 + HCl \rightarrow SiCl_4 + H_2$	3.505	2.63	43.10
G-101	Reverse	7.398	1.94	62.20
G-102	$2SiCl_3 \rightarrow Si_2Cl_6$	11.58	0.25	0.220
G-103	Reverse	20.98	-2.15	78.96
G-104	$SiCl_3 + SiHCl_2 \rightarrow Si_2HCl_5$	9.420	0.43	-0.001
G-105	Reverse	23.72	-2.36	78.91
G-106	$2SiHCl_2 \rightarrow Si_2H_2Cl_4$	12.13	0.17	0.250
G-107	Reverse	23.71	-2.37	77.68
G-108	$SiCl_2 + H \rightarrow SiHCl_2$	12.86	0.35	-0.690
G-109	Reverse	19.10	-1.25	50.33
G-110	$Si_2Cl_6 \rightarrow SiCl_4 + SiCl_6$	12.07	0.47	48.31
G-111	Reverse	1.270	3.03	12.99
G-112	$Si_2HCl_5 \rightarrow SiCl_2 + SiHCl_3$	11.50	0.45	45.48
G-113	Reverse	1.370	2.96	11.98
G-114	$Si_2H_2Cl_4 \rightarrow SiCl_2 + SiH_2Cl_2$	10.50	0.59	50.02
G-115	Reverse	-1.588	3.06	16.98
G-116	$Si_2HCl_5 \rightarrow SiCl_4 + SiHCl$	11.160	0.60	50.99
G-117	Reverse	2.200	2.93	0.488
G-118	$Si_2D_2Cl_4 \rightarrow SiCl_2 + SiD_2Cl_2$	11.060	0.66	43.41
G-119	Reverse	0.620	3.24	9.420
G-120	$Si_2D_2Cl_4 \rightarrow SiDCl + SiDCl_3$	10.84	0.62	46.640
G-121	Reverse	1.200	2.99	1.780
G-122	$SiHCl + SiHCl_3 \rightarrow Si_2Cl_4 + H_2$	10.86	0.84	52.88
G-123	Reverse	4.110	2.36	6.210
G-124	$Si_2Cl_4 \rightarrow 2SiCl_2$	21.14	-2.92	24.92

G-125	Reverse	10.57	-0.23	0.380
G-126	$N_2 + 2Si \rightleftarrows 2SiN$	13.00	0.00	0.00
G-127	$N_2 + H \rightleftarrows NNH$	14.30	-0.60	15.50
G-128	$NNH + NH \rightleftarrows N_2 + NH_2$	13.71	0.00	0.00
G-129	$N_2H_2 + NH \rightleftarrows NNH + NH_2$	13.00	0.00	0.00
G-130	$NNH + NH_2 \rightleftarrows N_2 + NH_3$	13.70	0.00	0.00
G-131	$N_2H_2 + NH_2 \rightleftarrows NNH + NH_3$	13.00	0.00	0.993
G-132	$NH_3 + H \rightleftarrows NH_2 + H_2$	5.800	2.39	10.10
G-133	$NH + H \rightleftarrows N + H_2$	14.00	0.00	0.00
G-134	$NH + N \rightleftarrows N_2 + H$	13.48	0.00	0.00
G-135	$2NH_2 \rightleftarrows N_2H_2 + H_2$	11.71	0.00	0.00
G-136	$NH_2 + H \rightleftarrows NH + H_2$	13.84	0.00	3.624
G-137	$NH_2 + NH \rightleftarrows N_2H_2 + H$	13.70	0.00	0.00
G-138	$N_2H_2 + H \rightleftarrows NNH + H_2$	13.70	0.00	0.993
G-139	$N_2H_2 + M \rightleftarrows NNH + H + M$	16.70	0.00	49.65

Surface kinetic mechanism

$k = AT^{\alpha}e^{-E_{act}/RT}$, parameters expressed in units consistent with mol, cm^2, s, kcal.

→ denotes a forward reaction, ⇄ denotes a reversible reaction.

Index	Reaction	Log_{10} A	α [-]	E_{act} [kcal/mol]
A-1	$CH_4 + \sigma_{Si} \rightarrow C^* + 2H_2$	9.38	0.50	0.00
A-2	$CH_3 + \sigma_{Si} \rightarrow CH^* + H_2$	11.93	0.50	0.00
A-3	$CH_2 + \sigma_{Si} \rightarrow C^* + H_2$	11.95	0.50	0.00
A-4	$CH + \sigma_{Si} \rightarrow CH^*$	11.97	0.50	0.00
A-5	$C_2H_5 + 2\sigma_{Si} \rightarrow C^* + CH^* + 2H_2$	20.76	0.50	0.00
A-6	$C_2H_4 + 2\sigma_{Si} \rightarrow 2C^* + 2H_2$	17.97	0.50	0.00
A-7	$C_2H_3 + 2\sigma_{Si} \rightarrow C^* + CH^* + H_2$	20.77	0.50	0.00
A-8	$C_2H_2 + 2\sigma_{Si} \rightarrow 2C^* + H_2$	19.00	0.50	0.00
A-9	$SiH_2 + \sigma_C \rightarrow SiH_2{}^*$	11.78	0.50	0.00
A-10	$SiH_2{}^* \rightarrow Si^* + H_2$	19.00	0.00	61.00
A-11	$SiH_4 + \sigma_C \rightarrow SiH_2{}^* + H_2$	10.50	0.50	18.678
A-12	$SiH + \sigma_C \rightarrow SiH^*$	11.79	0.50	0.00
A-13	$2SiH^* \rightarrow 2Si^* + H_2$	25.00	0.00	61.00
A-14	$Si + \sigma_C \rightarrow Si^*$	11.80	0.50	0.00
A-15	$Si_2H_5 + 2\sigma_C \rightarrow SiH^* + Si^* + 2H_2$	20.59	0.50	0.00
A-16	$Si_2 + 2\sigma_C \rightarrow 2Si^*$	20.61	0.50	0.00
A-17	$SiHCl_3 + 2\sigma_C + 2\sigma_{Si} \rightarrow SiCl^* + H^* + 2Cl^{*,Si}$	16.42	0.50	0.00
A-18	$SiCl_2 + 2\sigma_C \rightarrow SiCl^* + Cl^{*,C}$	19.49	0.50	0.00
A-19	$SiCl_2 + \sigma_C + \sigma_{Si} \rightarrow SiCl^* + Cl^{*,Si}$	19.49	0.50	0.00
A-20	$HCl + \sigma_C + \sigma_{Si} \rightarrow H^* + Cl^{*,Si}$	12.55	0.50	0.00

A-21	$H_2 + 2\sigma_C \rightarrow 2H^*$	11.36	0.50	0.00
A-22	$H + CH^* \rightarrow C^* + H_2$	12.53	0.50	0.00
A-23	$H + C^* \rightarrow CH^*$	12.53	0.50	0.00
A-24	$CH^* + CH^* \rightarrow H_2 + 2C^*$	23.00	0.00	57.100
A-25	$CH^* + CH^* \rightarrow C_2H_2 + 2\sigma_{Si}$	23.00	0.00	87.954
A-26	$H^* + CH^* \rightarrow H_2 + C^* + \sigma_C$	23.00	0.00	61.00
A-27	$Si^* \rightarrow Si + \sigma_C$	13.50	0.00	40.50
A-28	$2SiCl^* + H_2 \rightarrow 2Si^* + 2HCl$	15.37	0.50	60.00
A-29	$SiCl^* + HCl \rightarrow SiCl_2 + H + \sigma_C$	10.55	0.50	0.00
A-30	$SiCl^* + Cl^{*,C} \rightarrow SiCl_2 + 2\sigma_C$	19.00	0.00	20.095
A-31	$SiCl^* + Cl^{*,Si} \rightarrow SiCl_2 + \sigma_C + \sigma_{Si}$	19.00	0.00	89.806
A-32	$2SiCl^* \rightarrow SiCl_2 + Si^* + \sigma_C$	19.00	0.00	89.806
A-33	$SiCl^* + CH^* \rightarrow SiC + HCl + \sigma_C + \sigma_{Si}$	17.00	0.00	0.00
A-34	$SiCl^* + H^* \rightarrow HCl + Si^* + \sigma_C$	19.00	0.00	70.006
A-35	$Cl^{*,C} + H \rightarrow HCl + \sigma_C$	12.53	0.50	0.00
A-36	$Cl^{*,Si} + H \rightarrow HCl + \sigma_{Si}$	12.53	0.50	0.00
A-37	$Cl^{*,Si} + H^* \rightarrow HCl + \sigma_C + \sigma_{Si}$	19.00	0.00	89.806
A-38	$Cl^{*,Si} + CH^* \rightarrow HCl + C^* + \sigma_{Si}$	19.00	0.00	89.806
A-39	$Cl^{*,Si} + Si^* \rightarrow SiCl^* + \sigma_{Si}$	17.00	0.00	0.00
A-40	$CH^* + Cl^{*,C} \rightarrow HCl + C^* + \sigma_C$	19.00	0.00	84.190
A-41	$Si^* + Cl^{*,C} \rightarrow SiCl^* + \sigma_C$	17.00	0.00	0.00
A-42	$H^* + Cl^{*,C} \rightarrow HCl + 2\sigma_C$	19.00	0.00	84.190
A-43	$H^* + H^* \rightarrow H_2 + 2\sigma_C$	24.00	0.00	61.00
A-44	$Si^* + C^* \rightarrow SiC^{film} + \sigma_C + \sigma_{Si}$	17.00	0.00	0.00
A-45	$2Si^* + C^* \rightarrow Si_2C^{film} + 2\sigma_C + \sigma_{Si}$	23.00	0.00	0.00
A-46	$Si^* + 2C^* \rightarrow SiC_2^{film} + \sigma_C + 2\sigma_{Si}$	23.00	0.00	0.00
A-47	$SiCl + \sigma_C \rightarrow SiCl^*$	11.62	0.50	0.00

A-48	$SiHCl + 2\sigma_C \rightarrow SiCl^* + H^*$	20.52	0.50	0.00
A-49	$SiC_2 + \sigma_C + 2\sigma_{Si} \rightarrow Si^* + 2C^*$	29.64	0.50	0.00
A-50	Reverse	31.00	0.00	82.262
A-51	$Si_2C + 2\sigma_C + \sigma_{Si} \rightarrow 2Si^* + C^*$	29.54	0.50	0.00
A-52	Reverse	31.00	0.00	55.834
A-53	$Si^* + CH^* \rightarrow SiC + H + \sigma_C + \sigma_{Si}$	17.00	0.00	0.00
A-54	$SiH^* + CH^* \rightarrow SiC + 2H + \sigma_C + \sigma_{Si}$	17.00	0.00	0.00
A-55	$SiH^* + C^* \rightarrow SiC + H + \sigma_C + \sigma_{Si}$	17.00	0.00	0.00
A-56	$SiH^* + \sigma_C \rightarrow Si^* + H^*$	17.00	0.00	0.00
A-57	$N_2 + 2\sigma_{Si} \rightarrow 2N^*$	20.77	0.50	66.00
A-58	$N + \sigma_{Si} \rightarrow N^*$	11.95	0.50	0.00
A-59	$NH + \sigma_{Si} \rightarrow NH^*$	11.94	0.50	0.00
A-60	$NNH + 2\sigma_{Si} \rightarrow N^* + NH^*$	21.06	0.50	0.00
A-61	$2NH^* \rightarrow 2N^* + H_2$	22.00	0.00	60.00
A-62	$N^* + Si^* \rightarrow SiN^{film} + 2\sigma_{Si}$	19.00	0.00	60.00
A-63	$2N^* + 2SiH^* \rightarrow 2SiN^{film} + H_2 + 4\sigma_{Si}$	19.00	0.00	60.00
A-64	$N^* + SiH_2{}^* \rightarrow SiN^{film} + H_2 + 2\sigma_{Si}$	19.00	0.00	60.00
A-65	$SiCl^* + N^* \rightarrow SiN^{film} + Cl + \sigma_C + \sigma_{Si}$	19.00	0.00	60.00
A-66	$NH_2 + \sigma_C \rightarrow NH^* + H$	11.92	0.50	0.00
A-67	$SiN + \sigma_C \rightarrow SiN^{film} + \sigma_C$	11.70	0.50	37.00

Bibliography

[1] Burton, W. K., Cabrera, N., Frank, C. F., *Phil. Trans.*, Royal Society (London), A243, p. 299 (1951).

[2] Masi, M., Kommu, S., *Semiconductors and Semimetals*, Volume 72, p.185-224 (2001).

[3] Warner, J. H., Schäffel, F., Bachmatiuk, A., Rümmeli, M. H., *Grapehene: fundamentals and emergent applications*, Chapter 4, p. 129-228 (2013).

[4] Masi, M., Di Stanislao, M., Veneroni, A., *Fluid-dynamics during vapor epitaxy and modelling*, Progress in Crystal Growth and Characterization of Materials, 47, p. 239-270 (2003).

[5] Hess, D. W. , Graves, D. B., *Chemical Vapor Deposition*, Eds. M. L. Hitchman and K. F. Jensen, Academic Press, New York (1989).

[6] Van de Burgt, Y., *Laser-assisted growth of carbon nanotubes – A review*, Journal of Laser Applications 26 (2014).

[7] Väyrynen, K., *Photo-Assisted Atomic Layer Deposition and Chemical Vapor Deposition of Metal and Metal Oxide Thin Films*, University of Helsinki (2016).

[8] Wolf, S., Tauber, R. N., *Silicon Processing for the VLSI Era*, Lattice Press, Volume 1, p. 128 (1986).

[9] Jones, A. C., Hitchman, M. L., *Chemical Vapour Deposition: Precursors, Processes and Applications*, Royal Society of Chemistry (2009).

[11] UNESCO, public domain image.

[12] Ellison, A., Zhang, J., Henry, A., Janzén, E., *Epitaxial growth of SiC in a chimney CVD reactor*, Journal of Crystal Growth, 236, p. 225-238 (2002).

[13] Ullmann, F., *Silicon Carbide*, Encyclopedia of Industrial Chemistry (2007).

[14] Liu, T., Xu, Z., Rommel, M., *Raman Characterization of Carrier Concentrations of Al-implanted 4H-SiC with Low Carrier Concentration by Photo-Generated Carrier Effect*, Crystals, 9, 428 (2019).

[15] Deblecker, O., De Grève, Z., Versèle, C., *Comparative Study of Optimally Designed DC-DC Converters with SiC and Si Power Devices*, Advanced Silicon Carbide Devices and Processing (2015).

[16] Krenkel, W., Heidenreich, B., Renz, R., *C/C-SiC Composites for advanced Friction Systems*, Advanced engineering materials, 4 (2002).

[17] E. G. Acheson, *Manufacture of graphite*, patent US568323A (1896).

[18] N. N. Ault, *Structure and Properties of Silicon Carbide Ceramics*, Encyclopedia of Materials: Science and Technology, p. 8502-8508 (2001).

[19] W. R. Matizamhuka, *Gas transport mechanism and the behaviour of impurities in the Acheson furnace for the production of silicon carbide*, Heliyon, Volume 5, Issue 4 (2019).

[20] V. Kumar, Y. Gupta, *Study of formation of silicon carbide in the Acheson Process*, Steel Research International: a journal for steel and related materials, Volume 73, Issue 2 (2002).

[21] J. A. Lely, Sublimation process for manufacturing silicon carbide crystals, patent US2854364A (1958).

[22] G. J. Caras, *Silicon Carbide for Semiconductors*, Redstone Scientific Information Center (1965).

[23] R. W. Brander, R. P. Sutton, *Solution grown SiC p-n junctions*, Journal of Physics D: Applied Physics, Volume 2, Issue 3, p. 309-318 (1969).

[24] V. A. Dmitriev, *Silicon carbide and SiC-AlN solid-solution p-n structures grown by liquid-phase epitaxy*, Physica B 185, p. 440-452 (1993).

[25] P. Capper, I. Stuart, T. Joyce, *Epitaxial Crystal Growth: Methods and Materials*, Springer Handbook of Electronic and Photonic Materials, Chapter 1 (2017).

[26] Larkin, D. J. Neudeck, P. G., Powell, J. A. & Matus, L. G., *Site-competition epitaxy for superior silicon carbide electronics*, Applied Physics Letters 65, p. 1659-1661 (1994).

[27] Larkin, D. J., *SiC dopant incorporation control using site-competition CVD*, Physica Status Solid (B) Basic Research 202, p. 305-320 (1997).

[28] Yamamoto, T., Kimoto, T. & Matsunami, H., *Impurity incorporation mechanism in step-controlled epitaxy growth temperature and substrate off-angle dependence*, Materials Science Forum 264-168, p. 111-114 (1998).

[29] Kojima, K., Kuroda, S., Okumura, H. & Arai, K., *Nitrogen incorporation characteristics on a 4H-SiC epitaxial layer*, Applied Physics Letters 88, p. 1-3 (2006).

[30] Zhang., J. Ellison, A., Henry, A., Linnarsson, M. K. & Janzen, E., *Nitrogen incorporation during 4H-SiC epitaxy in a chimney CVD reactor*, Journal of Crystal Growth 236, p. 101-112 (2001).

[31] Zhang., J. Ellison, A., Henry, A., Linnarsson, M. K. & Janzen, E., *Nitrogen doping of epitaxial silicon carbide*, Journal of Crystal Growth 226, p. 267-276 (2002).

[32] Ferro, G. and Chaussende, D., *A new model for in situ nitrogen incorporation into 4H-SiC during epitaxy*, Scientific Report 7, 43968 (2017).

[33] Allendorf, M. D., Melius, C. F., *Theorical study of the thermochemistry of molecules in the silicon-carbon-hydrogen-system*, Journal of Physical Chemistry 96, p. 428-437 (1992).

[34] Allendorf, M. D., Kee, R. J., *A Model of Silicon Carbide Chemical Vapour Deposition*, Journal of the Electrochemical Society 138, p. 841-853 (1991).

[35] Coltrin, M. E., Kee, R. J., Evans,G. H., *A Mathematical Model of the Fluid Mechanics and Gas-Phase Chemistry in a Rotating Disk Chemical Vapour Deposition Reactor***,** Journal of the Electrochemical Society 136, p. 819-829 (1989)

[36] Danielsson, O., Henry, A., Janzen, E., *Growth rate predictions of chemical vapour deposited silicon carbide epitaxial layers*, Journal of Crystal Growth 243, p. 170-184 (2002)

[37] Veneroni, A., Masi, M., *Gas phase and surface kinetics of epitaxial silicon carbide growth involving chlorine-containing species*, Chemical Vapour Deposition 12, (8-9), p. 562-568 (2006).

[38] Fiorucci, A., Moscatelli, D., Masi, M., *Mechanism of n-doping of silicon carbide epitaxial films*, Journal of Crystal Growth 303, 1, p. 345-348 (2007).

[39] Cavallotti, C., Rossi, F., Ravasio, S. V., Masi, M., *A Kinetic Analysis of the Growth and Doping Kinetics of the SiC Chemical Vapour Deposition Process*, Industrial & Engineering Chemistry Research, Volume 3 (2014).

[40] Carrà, S., Masi, M., *Kinetic approach to materials synthesis by gas phase deposition*, Progress in Crystal Growth and Characterization of Materials, p. 1-46 (1998)

[41] Kee, R. J., Coltrin, M. E., Glarborg, P., *Chemically Reacting Flow: Theory and Practice*, John Wiley & Sons, Hoboken (2003).

[42] Carrà, S., Masi, M., Morbidelli, M., Scaravaggi, V., Preti, F., *Chemical Engineering Science 45*, 3551 (1990).

[43] Carrà, S., Masi, M., Morbidelli, M., *Italian Crystal Growth 1988*, 23 (1998).

[44] Masi, M., Cavallotti, C., Radaelli, G., Carrà, S., *Crystal Research Technologies 32*, 1125 (1997).

[45] Cess, R. D., Shaffer, E. C., *Applied Science Research A8*, 339 (1959).

[46] A. V. Luikuv, *Heat and Mass Transfer*, MIR Moscow (1980).

[47] Skelland, A. H. P., *Diffusional Mass Transfer*, J.Wiley, New York (1974).

[48] Fiorucci, A., *Dopants Incorporation Kinetics for Silicon Carbide Chemical Vapour Deposition Processes*, Chemical Engineering Ph. D. Thesis , Chapter 5 (2008).

[49] Brown, P. N., Hindmarsh, A. C., Petzold, L. R., *Using Krylov Methods in the Solution of Large-Scale Differential-Algebraic Systems*, Siam Journal on Scientific Computing, 19, p. 1495-1512 (1994).

[50] Masi, M., Carrà, S., Zonca, R., *Estimation of the Dopant Effect of the Surface Kinetics in CVD Systems through the Charge-Transfer Theory*, Proceedings of the Thirteenth International Conference on Chemical Vapour Deposition, Volume 96-5, p. 47 (1996).

Other consulted sources:

[51] Rota, R., *Termodinamica dell'Ingegneria Chimica*, Pitagora Editrice, Chapter 9.

Physical parameters

A_j	pre-exponential factor for the j-th reaction*
a_i	i-th species activity [-]
C_i	i-th species concentration [mol/m^3]
$\widetilde{c_P}$	mixture mass specific heat [J/kg/K]
D	disk diameter [m]
d	distance [m]
$E_{act,j}$	activation energy for the j-th reaction [J/mol]
g	gravitational acceleration [m/s^2]
$G.\ R.$	film growth rate [m/s]
$\dot{H}$	total enthalpic flux [W]
H	spacing between susceptor and reactor wall[m]
h	liminar heat transfer coefficient [W/m^2/K]
h_P	Planck's constant [m^{2}kg/s]
$K_{m,i}$	mass transfer coefficient [m/s]
k_B	Boltzmann constant [m^{2}kg/s^2/K]
k_j	kinetic constant for the j-th reaction*
L	characteristic length [m]
L_{wafer}	wafer diameter [m]
m	total mass [kg]
$\dot{m}$	total mass flowrate [kg/s]
m_i	i-th species mass [kg]
$\dot{m}_i$	i-th species mass flowrate [kg/s]
N_i	i-th species mass diffusive flux [kg/m^2/s]

n_i	i-th species molar diffusive flux [mol/m^2/s]
O_{ij}	partial j-th reaction order of the i-th species [-]
P	pressure [Pa]
P_i	i-th species partial pressure [Pa]
P_{rif}	reference pressure [Pa]
$Q^{()}$	generic partition function
$\dot{q}$	heat flux [W/m^3]
R_{gas}	universal gas constant [J/mol/K]
R_j	reaction rate of the j-th reaction [mol/m^3/s]
S_e	specific surface referred to ext. heat exchange [m^{-1}]
S_V	active surface [m^{-1}]
s	disuniformity parameter [-]
T	temperature [K]
t	time [s]
T_{rif}	reference temperature [K]
U	global heat transfer coefficient [W/m^2/K]
u	velocity [m/s]
V_i	i-th species molar volume [m^3/mol]
W_i	i-th species molecular weight [kg/kmol]
x_i	i-th species molar fraction in the film [-]
y_i	i-th species molar fraction inside the gas [-]
z	axial coordinate [m]

*expressed in unit consistent with kmol, m^3, s.

NC	number of components
NCG/NCS	number of components inside the gas/at the surface
NR	number of reactions
NRG/NRS	number of gas phase reactions/surface reactions
N_{sites}	number of sites

Greek letters

α_j	j-th reaction temperature exponential coefficient [-]
$\alpha_{T,i}$	i-th species thermal diffusion coefficient [-]
Γ_i	i-th species material diffusion coefficient [m^2/s]
$\Delta G_{R,j}$	free Gibbs energy variation of the j-th reaction [J/mol]
$\Delta g_{f,i}$	free Gibbs energy variation of i-th species formation [J/mol]
ΔH_{Rj}	enthalpic contribute of the j-th reaction [J/mol]
δ_x	boundary layer thickness [m]
$\theta_{m,i}$	i-th species coverage fraction on the m-th kind of surface site
λ_T	thermal conductivity coefficient [W/m/K]
ξ_i	i-th species valence [-]
μ	dynamic viscosity [Pa*s]
ν_{ij}	i-th species stoichiometric coefficient of the j-th reaction [-]
ρ	mass density [kg/m^3]
σ_C, σ_{Si}	carbon site, silicon site [-]
ψ_m	m-th type site surface concentration [mol/m^2]
ω_i	i-th species mass fraction [-]

Dimensionless numbers

$$Nu_L = \frac{hL}{\lambda_{T,G}} = \frac{convective\ heat\ transfer}{conductive\ hea\ \ transfer}$$ Nusselt number

$$Pr = \frac{\mu_G c_{pG}}{\lambda_{T,G}} = \frac{momentum\ diffusion}{therm\ \ \ diffusion}$$ Prandtl number

$$Re_L = \frac{\rho_G u L}{\mu_G} = \frac{inertia}{viscous\ forces}$$ Reynolds number

$$Sc = \frac{\mu_G}{\rho_G \Gamma_G} = \frac{momentum\ diffusion}{material\ diffusion}$$ Schmidt number

$$Sh_L = \frac{K_m L}{\Gamma_G} = \frac{convective\ mass\ transfer}{diffusive\ mass\ transfer}$$ Sherwood number

Suffixes and Acronyms

“^{G}” or “$_{G}$” and “^{S}” or “$_{S}$” respectively refer to the gas and surface phases;

“^{R}” and “$^{\neq}$” respectively stands for “reactant” and “transition state”.

“*” stands for “adsorbed”;

“$_{i}$” refers to the i-th species and “$_{j}$” refers to the j-th reaction;

“$_{film}$” refers to the deposition surface film;

“$_{peak}$” stands for “peak value”;

“^{EQ}” or “$_{EQ}$” refers to thermodynamic equilibrium conditions.

Mathematical notation

φ	scalar φ
$\boldsymbol{\varphi}$	vector φ
$\boldsymbol{\varphi}^{\boldsymbol{T}}$	transposed vector φ
$\hat{\boldsymbol{\varphi}}$	versor φ
$\cdot$	scalar product
$\left.\frac{d\varphi}{dx}\right\|_{x_0}$	derivative of φ with respect to x evaluated at x_0
$\left.\frac{\partial\varphi}{\partial x}\right\|_{x_0}$	partial derivative of φ with respect to x evaluated at x_0
∇	Nabla operator
$\nabla\varphi$	gradient of φ
$\nabla \cdot \boldsymbol{\varphi}$	divergence of $\boldsymbol{\varphi}$
$\boldsymbol{I}$	identity matrix

Gradient of scalar φ is defined as $\nabla\varphi = \frac{\partial\varphi}{\partial x} + \frac{\partial\varphi}{\partial y} + \frac{\partial\varphi}{\partial z}$;

Divergence of vector $\boldsymbol{\varphi}$ is defined as $\nabla \cdot \boldsymbol{\varphi} = \frac{\partial\varphi_x}{\partial x} + \frac{\partial\varphi_y}{\partial y} + \frac{\partial\varphi_z}{\partial z}$;

The identity matrix is defined as $\boldsymbol{I} = \begin{bmatrix} 1 & 0 & 0 \\ 0 & 1 & 0 \\ 0 & 0 & 1 \end{bmatrix}$.